Monte Carlo Investigation of Electron Beam Relative Output Factors

by

Geoffrey G. Zhang

A dissertation submitted in partial fulfillment of

the requirements for the degree of

Doctor of Philosophy

Carleton University

Ottawa, Canada

i

Canada

ABSTRACT

One of the tasks in commissioning an electron accelerator in cancer clinics is to measure relative output factors (ROFs) versus various parameters such as applicator size (called applicator factors), cutout size (cutout factors) and air-gap size (gap factors) for various electron beam energies and applicator sizes. This kind of measurement takes a lot of time and labour. This thesis shows that Monte Carlo simulation offers an alternative to this task. With *BEAM* (Med. Phys. 22(1995)503-524), an *EGS4* user-code, clinical accelerator electron beams are simulated and ROFs for a Siemens MD2 linear accelerator and a Varian Clinac 2100C accelerator are calculated. The study shows that the Monte Carlo method is not only practical in clinics but also powerful in analyzing the related physics. The calculated ROFs agree within 1% with the measurements for most cases and 2% for all cases that have been studied, which is more than acceptable in clinical practice. The details of each component of the dose, such as dose from particles scattered off the photon-jaws and the applicator, the dose from contaminant photon, the dose from direct electrons, *etc.*, are also analyzed. The study also explains quantitatively why the effective SSD (Source to Phantom Surface Distance) is often not the nominal reference SSD. For ROF measurements for small fields using an ion chamber, this study discusses the stopping-power ratio corrections due to changes in the depth of dose maximum as a function of field size and versus various accelerators.

Since it handles ROF calculations for arbitrary fields, including square, rectangular, circular and irregular fields, in the same way, Monte Carlo is the simplest method to get ROFs compared to other algorithms. As the first step towards implementing Monte Carlo methods in clinical treatment planning, Monte Carlo calculations for electron beam ROFs can replace measurements in clinical practice. It takes about 6 hours of CPU time on a single Pentium Pro 200MHz computer to simulate an accelerator and additional 2 hours for each ROF.

sions with me, reading the chapters of my thesis and papers, and making very helpful suggestions. Besides his intelligence, wide range of knowledge and strong expertise in medical physics, his enthusiasm, conscientiousness and scrupulousness in research set a good example for me and will definitely continue to influence me in the future. I will treasure this valuable experience.

Contents

List of Tables

List of Figures

List of Symbols

$1 - D$: One-dimensional method used in calculating relative output factors for rectangular fields;

A: field size defined by a cutout, in cm^2;

A': field size defined by an open applicator, in cm^2;

A_0: reference field size defined by the reference applicator, in cm^2;

AE: threshold energy for secondary electron production, in MeV;

$BEAM$: $EGS4$ user-code for Monte Carlo simulations of clinical radiation units;

$CLINAC$ 2100C: a model of Varian accelerator;

CM: Component Module used in $BEAM$ to define a specific class of geometric shape;

Δ: cutoff energy in Spencer–Attix formulation of the Bragg-Gray equation;

$DOSRZ$: $EGS4$ user-code for Monte Carlo calculations of cylindrical 2-dimensional dose distributions;

$DOSXYZ$: $EGS4$ user-code for Monte Carlo calculations of 3-dimensional dose distributions;

D_{max}: maximum absorbed dose (usually on a depth-dose curve);

$\%DD$: percentage depth-dose;

$\frac{D}{U}$: dose per monitor unit, in cGy;

d_{max}: depth at which D_{max} occurs, in cm, also called R_{100};

$\overline{E}_o$: mean energy of electron beam at phantom surface, in MeV;

$ECUT$: cutoff energy for electrons in Monte Carlo simulations using $EGS4$ code (total energy, MeV);

$EGS4$: Electron Gamma Shower Version 4, a Monte Carlo code system;

$ESAVE$: the maximum charged particle energy (in MeV) at which range rejection is considered in $EGS4$ simulations;

$ESTEPE$: the maximum fractional energy loss per electron step in $EGS4$ simulations;

GF: gap factor. Relative output factor for open applicators with respect to different SSDs;

g: air-gap thickness, in cm;

$KD2$: a model of Siemens accelerator;

$(\bar{L}/\rho)_{\text{air}}^{\text{water}}$: ratio of averaged restricted stopping powers for water to air. The average is by the Spencer-Attix theory over the total electron energy spectrum at the point of measurement (AAPM notation);

M: reading of an ionization chamber system corrected for temperature and air pressure, in nC;

$\frac{M}{U}$: reading of an ionization chamber per monitor unit, in nC;

$MD2$: a model of Siemens accelerator;

MeV: Mega electron-Volts, unit of energy;

N_{gas}: cavity-gas calibration factor (Unit: Gy/C or Gy/scale division);

$OMEGA$: a project to develop electron dose planning using Monte Carlo simulation (Ottawa Madison Electron Gamma Algorithm);

PCUT: cutoff energy for photons in Monte Carlo simulations using *EGS*4 code (MeV);

*PEGS*4: preprocessor which creates cross-section data sets for *EGS*4;

P_{ion}: Ion-recombination correction factor applicable to the calibration of the user's beam;

P_{repl}: a factor that corrects for replacement of phantom material by an ionization chamber's cavity;

PRESTA: an algorithm for electron transport;

P_{wall}: a factor that accounts for the walls being different from the medium and thereby changing the electron spectrum in the cavity;

ROF: relative output factor;

ROF_{app}: applicator factor. Relative output factor with respect of field sizes defined by open applicators;

ROF_{cut}: cutout factor. Relative output factor of the field defined by a cutout with reference to the field defined the open applicator in which the cutout is inserted;

R_{50}: depth at which dose in an electron beam falls to 50% of D_{max}, in cm.

R_p: practical range of an electron beam; depth of intersection of a line drawn tangent to the depth-dose curve at the unflection point and a line extrapolated from the bremsstrahlung tail, in cm;

SPR: Stopping-Power Ratio;

SQRT: square-root method used in calculating ROFs for square fields;

SPRRZ: *EGS*4 user-code for Monte Carlo calculations of stopping-power ratios;

SSD: Source-Surface Distance, in cm;

SSD_{eff}: effective SSD, in cm;

Chapter 1

Introduction

1.1 Radiotherapy

In this modern world, cancer remains one of the major threats to human lives. According to The National Cancer Institute of Canada[1], an estimated 129,200 new cases of cancer and 62,700 deaths from cancer will occur in Canada in 1998. For women, 1 in 9 is expected to develop breast cancer during their lifetime, 1 in 18 will develop colorectal cancer, and 1 in 21 will develop lung cancer. Among men, 1 in 8 will develop prostate cancer during their lifetime, mostly after age 70, and 1 in 11 will develop lung cancer. An average of 912 Canadian children were diagnosed with cancer each year between 1989 and 1993 and an average of 173 died each year between 1991 and 1995.

The major treatments of cancer include surgery, chemotherapy, radiotherapy, and combinations of these therapies. Among them, radiotherapy, in which radiation is used, is commonly applied due to its high cure rate in many cases. Radiation treatment is based on the fact that radiation can kill human cells, tumor or healthy ones. A complete understanding of why radiation damages mammalian cells and some of the damaged cells repair themselves while some of them die is not yet achieved, although scientists have had some theories which can partially explain why. One of the most widely used theories is called "multiple-target single-hit model"[2]. The basic idea of this theory is that in a cell, there are several critical structures which are called *targets*. These targets are believed to be DNA molecules in genes. If one or a few of these targets are hit by radiation particles, this cell mostly repairs itself and survives. If all of the targets are hit in a short time, the cell dies. So to kill a tumor cell, enough radiation must be delivered to it. The amount of radiation absorbed in a medium is measured by *absorbed dose*, D, which is defined as the expectation value of the energy imparted to matter per unit mass at a point[3]. The SI unit for absorbed dose is *gray* (Gy). It replaced the old unit *rad*:

$$1 \text{ Gy} = 1 \text{ J/kg} = 10^2 \text{ rad} = 10^4 \text{ erg/g} . \tag{1.1}$$

are the most commonly used sources.
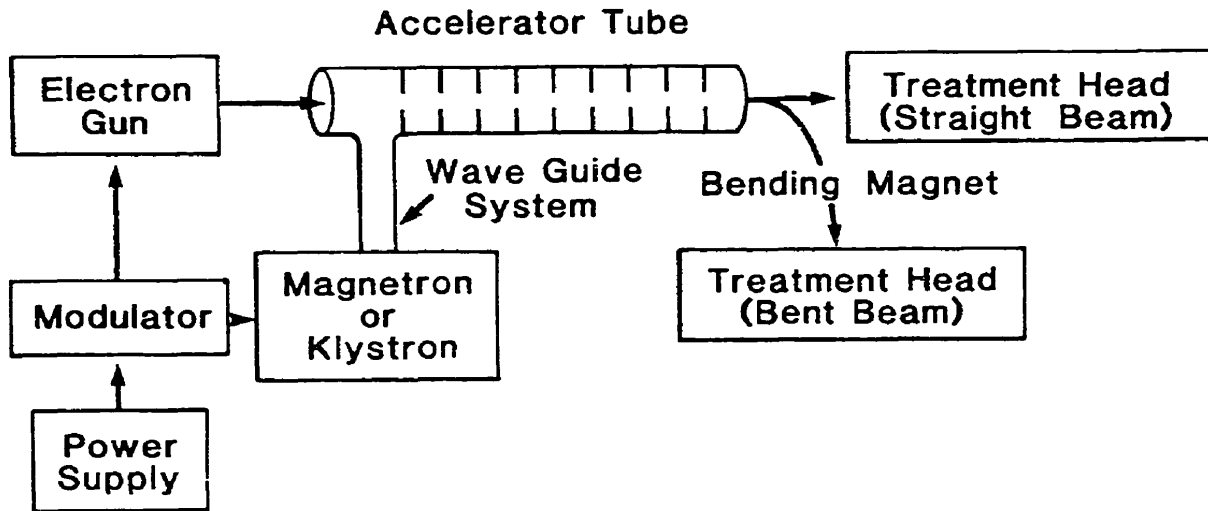
Accelerator Tube

Figure 1.2: A block diagram of typical medical linear accelerator (from Khan[4]).

Fig. 1.1 shows a Siemens MD2 accelerator which has options of 6, 9, 11 and 13 MeV electron beams. It contains an electron gun which emits electrons, microwave tubes which accelerate electrons to the desired energy, bending magnets which turn the electrons towards the patient (Fig. 1.2), and the accelerator head which uniformly spreads and collimates the radiation beam to the part of a patient's body in which the tumor is located. The accelerator head is of primary interest in this thesis. In the accelerator head for electron beams the scattering foil is to spread the beam to be uniform within the field; the monitor chamber is to register how many electrons go through it and the output from the chamber (number of monitor units, #MU) is used to calculate the dose delivered to the patient; the photon-jaws and applicator are to collimate the beam to a desired field size. A cutout is usually inserted on the last scraper of the applicator to define a field which is smaller than the open applicator.

1.2   The purpose and definition of ROF

Radiation can kill both tumor and healthy human cells. The treatments aim to kill the tumor while sparing the healthy tissue. For this reason, the radiation field size should match the size of the tumor to maximize the dose to the tumor and minimize the dose to the healthy tissue, and hence the radiation field size varies with patients. Since tumors always have different shapes, cutouts with different shapes of openings are often used. To insure the exact dose prescribed is delivered to the tumor, the relative output factors (ROFs) for different field sizes are used in electron beam treatment planning to calculate the number of monitor units for a treatment fraction (Eq. 1.2). ROFs include (1) applicator factor, ROF_{app}, which is the relative output (dose per monitor unit at the depth of maximum dose in a phantom) of a field defined by applicator A' with reference to the field defined by the reference applicator, A_0; (2) gap factor, GF, which is the relative output of a beam at one nominal source to phantom surface distance, SSD, with reference to the beam at the reference SSD, SSD_0, for an open applicator A'; and (3) cutout factor, ROF_{cut}, which is the relative output of a beam defined by an inserted cutout or block with reference to that of the beam defined by the open applicator at the same SSD. In the measurement or calculation of ROFs, a phantom, usually a tank of water, is used instead of a real patient. The number of monitor units for a given setup is given by:

$$\#MU = \frac{D}{RDR \cdot ROF_{\mathrm{app}} \cdot GF \cdot ROF_{\mathrm{cut}}} \, , \qquad (1.2)$$

where D is the prescribed dose per fraction in cGy and RDR is the reference dose rate in cGy/MU, which is dose per monitor unit for the reference field at the standard SSD, usually 10×10 cm^2 open applicator and SSD = 100 cm.

According to TG-25[5], the clinical electron beam dosimetry protocol of the American Association of Physicists in Medicine (AAPM), the applicator factor is defined as the ratio of dose per monitor unit, $\frac{D}{U}$, at its depth of maximum dose in a phantom,
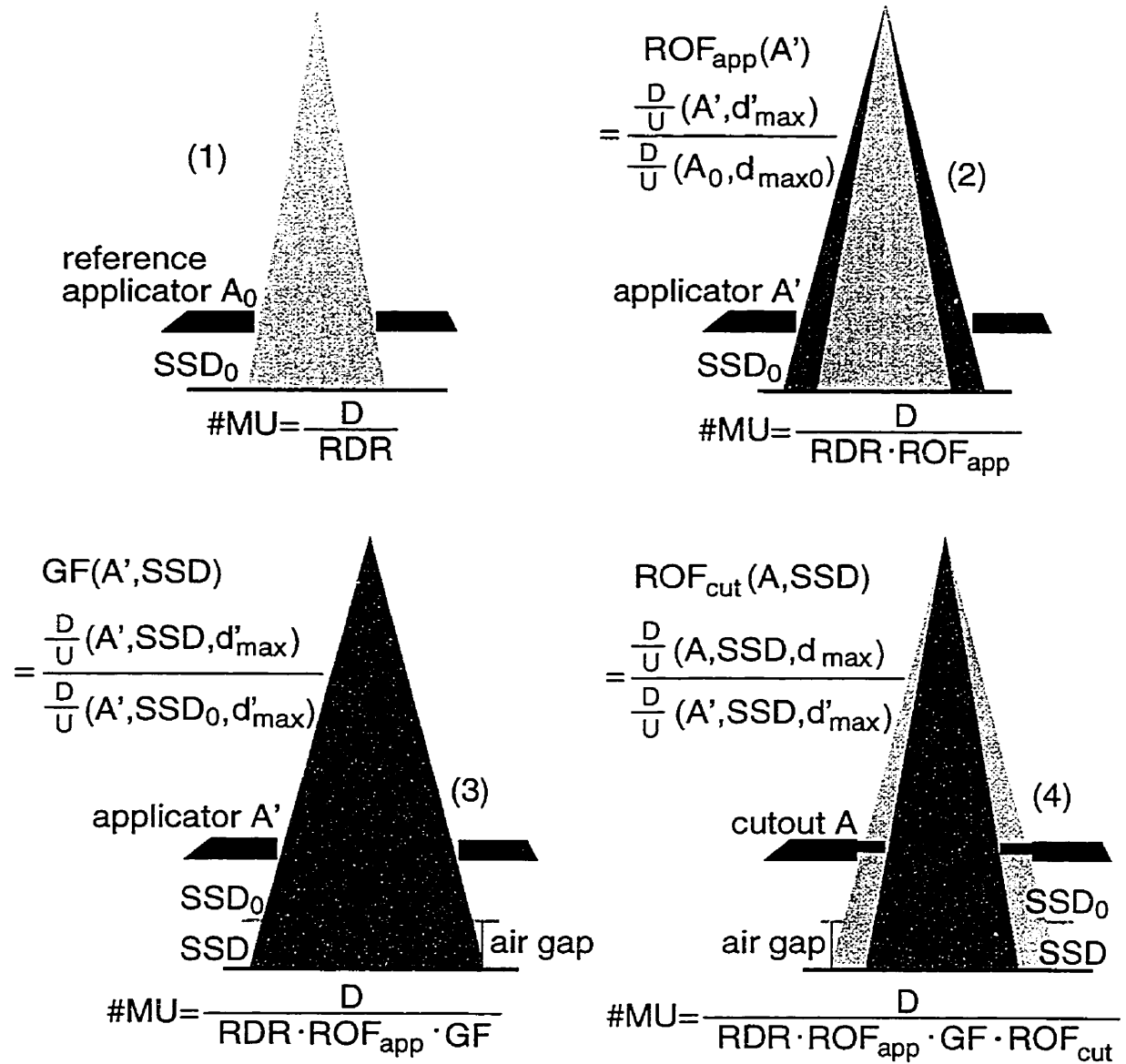
Figure 1.3: Definitions of ROFs and their usage in treatment planning. #MU is the number of monitor units which is the reading from the monitor chamber. Different set-ups of electron beams need different ROF data to calculate #MU needed to deliver the prescribed dose D to the patient.

cases, introduce inaccuracy, which often exceed the clinical tolerance on ROF values, usually 3% error. For these reasons, clinical physicists do not use these theories in ROF calculations.

Many methods have been introduced to predict the output at extended SSDs. For example, a major method currently employed in clinics to calculate GFs at any SSD is the effective point source method[4,17] in which one finds an effective source position to best fit the output data with the inverse square law. Then one can predict GF by using the inverse square law based on this effective source position. The problem is that the value of SSD_{eff} varies strongly with both field size and beam energy, and hence this method requires many measurements for each applicator and beam energy to determine the effective SSD. One needs the square root of the ratio of the chamber reading at d_{max} with no air gap, Q_o, to the reading at its own d_{max} with air gap, Q_g, which is $[Q_o/Q_g]^{1/2}$, versus the air gap g for each beam energy and field size[5,18].

There are many papers[19–22] that deal with the calculation of ROFs directly. For example, two methods, SQRT and 1-D, were introduced by Mills *et al.*[19] to calculate ROFs for rectangular fields based on other known ROF values of square and rectangular fields. The SQRT method gives:

$$ROF(X \times Y) = \sqrt{ROF(X \times X) \cdot ROF(Y \times Y)} \,, \qquad (1.6)$$

which needs ROFs for square fields of $X \times X$ and $Y \times Y$ to calculate the ROF for an $X \times Y$ field. The one-dimensional method gives,

$$ROF(X \times Y) = ROF(X \times X_0) \cdot ROF(X_0 \times Y) \,, \qquad (1.7)$$

which needs the measured ROFs for two rectangular fields, $X \times X_0$ and $X_0 \times Y$, to calculate the ROF for the rectangular field $X \times Y$, where $X_0 \times X_0$ is the standard field. Both methods require extensive measurements to be used clinically.

For electron beam irregular fields, since the equivalent square concept from photon beam calculations cannot be applied to electron beam calculations[23], many other

algorithms have been developed. Some of them use a pencil beam algorithm to calculate the variation in electron fluence and take into account the electron scatter from the collimator system[21,22,24]. Others employ Clarkson type integration and also consider the fluence variation with field size which is obtained by measurements for beams with various radii[25,26]. All these algorithms require a lot of measurement data for the scattered component in ROF calculations.

Although there are many algorithms introduced to calculate ROFs for electron beams, for the reasons discussed above, measurement is the most commonly used approach in clinics. In cancer clinics using electron beams for radiotherapy, since many different field sizes and SSDs are used in treatments, commissioning of an accelerator includes the measurement of electron beam relative output factors versus field sizes and SSD, which takes a lot of work and time. Especially for irregular fields, measurements are usually done at night when there is no treatment ongoing with the accelerators.

1.4 Monte Carlo, another possible approach

1.4.1 What is Monte Carlo?

History

Monte Carlo is the name of a city in Monaco which is famous for gambling. In the 1940s, a group of scientists working on nuclear weapons in Los Alamos applied this name to a class of mathematical methods which use random numbers to simulate stochastic process and produce useful numerical results. Although Monte Carlo techniques have been enhanced enormously by the rapid development of modern computers since World War II, the first experiment using random sampling to solve a problem was carried out by Comte de Buffon[27,28] in 1777. The problem was like this:

A needle of length L is thrown at random onto a horizontal plane filled with parallel straight lines which are a distance d ($d > L$) apart. What is the probability P that the needle intersects one of the lines? Comte de Buffon determined P by throwing the needle many times and also solved the problem by mathematical analysis. The probability is $P = \frac{2L}{\pi d}$. Later, Laplace[29] suggested that π could be evaluated by throwing this needle, which is a Monte Carlo method again.

In the 1930s, Enrico Fermi carried out numerical experiments on neutron interactions with condensed matter[28]. These are called Monte Carlo calculations. After World War II, Monte Carlo methods started to be applied in statistical mechanics[30,31], evaluation of finite-dimensional integrals[32,33], radiation transport[34-36], heat transfer[37], economic modeling, *etc.*. The fast growth of computer power in recent years makes Monte Carlo applications cover many fields including medical physics.

The major Monte Carlo codes used in medical physics now, including EGS[38-40], $ETRAN$[41] and its progeny $SANDYL$[42], $CYLTRAN$[43], *etc.*, were originally created in the 1960s and 1970s. $BEAM$[44], an EGS4 user-code, which models clinical radiation units, was developed in this decade at the National Research Council of Canada. More details about EGS4 and $BEAM$ are discussed in the following chapter. There are also many other Monte Carlo codes which use other Monte Carlo techniques, such as MMC[45,46], VMC[47,48], $MCNP$[49,50], $PENELOPE$[51], *etc.*, that aim for clinical usage, but EGS4 is the most widely used code.

Basic ideas in Monte Carlo

Although there are many different techniques used in Monte Carlo methods, random number sampling is the core of Monte Carlo. Two examples in different applications are given in this section to show how random number sampling works in Monte Carlo calculations.

A very simple example is to calculate the area of a circle with a diameter of 1,

or radius $r = 0.5$. Since the area of a square with side-width of 1 is 1, the ratio of the area of the circle to that of the square is the area of the circle. So we can use rejection techniques which pick a pair of random numbers R_1 and R_2, which are uniformly distributed between 0 and 1, and compare $(R_1 - 0.5)^2 + (R_2 - 0.5)^2$ with $r^2 = 0.25$. If $(R_1 - 0.5)^2 + (R_2 - 0.5)^2 > 0.25$, the position determined by the pair of random numbers as coordinates is out of the circle and is rejected. Otherwise, it is in the circle and is accepted. Repeat this many times. The area is approximately the ratio of the number of accepted trials (which corresponds to the area of the circle) to the total number of trials (the area of the square).

This example also shows that the Monte Carlo method can be used to solve mathematical problems. This case evaluates a definite integral,

$$I = \int_0^1 \int_0^{\sqrt{1-x^2}} dx \; dy \; . \tag{1.8}$$

Since the area ratio of the circle to the square is $\pi/4$, this is also a way that Monte Carlo calculates the value of π.

The value of π can be calculated faster and more accurately using other non-Monte Carlo methods, however, in multiple dimensions, Monte Carlo methods are often the only effective means of evaluating integrals.

The rejection techniques are easy to understand and are good approaches for some problems like the one above, but they are low in efficiency for other kinds of problems. The rejection techniques are also used in particle transport simulations.

In particle transport simulations, random numbers are used to determine a parameter of a random event governed by the probability distributions. For example, the probability P that an interaction takes place after a flight through a distance greater than x in a given material for a photon at a given energy follows

$$P(x) = e^{-\mu \cdot x} \; , \tag{1.9}$$

where μ is the narrow beam linear attenuation coefficient, in cm^{-1}, at the given

energy. To determine the path length x of a photon, a random number R_1 is picked, and the path length is calculated as

$$x = -\frac{1}{\mu} \ln R_1 \quad (\text{cm}) , \qquad (1.10)$$

which is exponentially distributed between 0 and infinity with a mean value of $1/\mu$[52].

To further determine which kind of interaction happens, more random numbers are needed. For example, suppose only Compton scattering and pair production are included in the photon transport for the above example, *i.e.*,

$$\mu = \mu_{Compton} + \mu_{pair} . \qquad (1.11)$$

One more random number R_2 is generated. If $R_2 \leq \mu_{Compton}/\mu$, a Compton interaction is selected. Otherwise, a pair production event occurs. These two examples are the simplest but the most often used sampling techniques in photon-transport Monte Carlo simulations[52]. Some other samplings are complex, such as those based on the complimentary bremsstrahlung and pair production differential cross sections.

The accuracy of Monte Carlo calculations depends on the number of trials (the number of histories in particle transport simulation) simulated. The more trials, the more accurate the result. For example, in the evaluation of π as illustrated in Fig. 1.4, if the number of trials is 100,000, the calculated value of π is 3.14 ± 0.01. If the number of trials is 10 million, the value is 3.1422 ± 0.0015 which is closer to the true value 3.141593 and the one standard deviation uncertainty is smaller.

Since Monte Carlo calculations require large numbers of trials and the calculations are usually complex, they are time consuming. That is why the development of Monte Carlo methods is heavily dependent on the growth of computer power and applications of Monte Carlo methods in various fields are more promising in the future.

1.4.2   Advantages of Monte Carlo in ROF calculations

The problems that block many algorithms from use in clinics are that they are either too complicated or not accurate enough for extreme cases. The Monte Carlo method, on the other hand, is simple and accurate in many clinical dosimetry and radiotherapy applications[44,53–58]. The calculation for ROFs is straight forward because an ROF for any field size at any SSD can be calculated directly from a single accelerator simulation. In principle, within the range of clinical applications, no matter how small the field is, how low the energy is, or how thick the air gap is, the calculation is performed in the same way.

One advantage of Monte Carlo calculations is that they allow us to deduce what is going on. For example, in Monte Carlo calculations, every particle can be labeled so that we can look at its history, and its dose contribution can be catalogued in different components and accumulated in different regions separately. This is called the "component analysis technique". This technique is extensively applied in this ROF study to understand the physics of clinical beams.

Two major paths of electrons, scattered and direct, are illustrated in Fig. 1.5. Those electrons that experience at least one scattering off field defining components belong to the scattered component which has two sub-groups: one scattered off the photon-jaws, the other one off the applicator. Those scattered only in the air, scattering foils and monitor chamber, and never experiencing scattering off the photon-jaws or applicator are defined as the direct component. Besides electrons, there are many contaminant photons created in the exit window, scattering foils or elsewhere in the accelerator head by electron bremsstrahlung. The number of photons at the phantom surface is often greater than the number of electrons, especially for high-energy electron beams and small fields. Every component of the electron dose behaves differently. In general, the direct component is the major source of the dose on the central axis. The component scattered off the applicator is very dependent on the field size,

while the one off the photon-jaws is relatively constant. The contaminant photon component is dependent on electron energy and field size as well. All the scattered components and photon component together contribute less than 10% of the total dose at d_{max}. More detailed discussion on the dose contributions from the different components is presented in the following chapters.

1.5   Measurements at the Ottawa Cancer Centre and elsewhere

All the measured depth-dose curves and ROFs for a Siemens MD2 accelerator which are compared with Monte Carlo calculations were made by Joanna Cygler at the Ottawa Regional Cancer Centre, and those for a Varian Clinac 2100C accelerator are from Rock Mackie of the University of Wisconsin in Madison, and from Denise Davis of the Radiological Physics Center (RPC) in Houston[59].

At the Ottawa Regional Cancer Centre, ROFs are measured for a Siemens MD2 linear accelerator for electron beams of energies 6-13 MeV using an RFA 300 dosimetry system (Therados) with a Scaditronix Si p-type electron detector silicon diode. The active volume is 2.5mm in diameter and 0.45mm thick. The outputs are also measured with an RK chamber (0.12 cm^3) with negative bias which needs correction for the polarity effect[19,60]. The % depth-dose curves and lateral profiles for each field size are measured using the silicon diode. The accelerator has various electron applicators with nominal source to applicator-end-distance of 95 cm. This introduces a 5 cm air gap between the applicator end and the standard SSD=100 cm plane. Cutouts made of cerrobend with a thickness of 1.2 cm are inserted into applicators to define field sizes smaller than a given open applicator. In this thesis, for an MD2 accelerator, a 10 × 10 cm^2 applicator means an applicator that defines a field of 10 × 10 cm^2 at SSD = 100 cm. The actual size of the opening in the last scraper in the applicator is

9.5×9.5 cm^2. Similarly, the size of opening in a 2×2 cm^2 cutout is actually 1.9×1.9 cm^2, 3×3 cm^2 cutout is 2.85×2.85 cm^2, and so on. For a Clinac 2100C accelerator, a 10×10 cm^2 applicator also means the applicator which defines a field of 10×10 cm^2 at an SSD $= 100$ cm, although the openings of the scrapers in the applicator are not 10×10 cm^2. The field defined by photon-jaws is usually much larger than that defined by applicators. For example, at SSD $= 100$ cm, the field size projected from the photon-jaws setting for a 10×10 cm^2 field defined by the applicator is 19×19 cm^2 for an MD2 accelerator.

1.6   The structure of this thesis

The purpose of the project was to calculate electron beam ROFs and analyze the related physics using Monte Carlo methods.

- Chapter 2 describes the widely-used Monte Carlo code *EGS*4 and its user code *BEAM* in more detail, and discusses various considerations in electron beam ROF calculations using *BEAM*.

- Chapter 3 presents the Monte Carlo calculations of applicator factors for a Siemens MD2 and a Varian Clinac 2100C accelerator and comparisons to measurements. The results in this chapter are based on parts of two papers submitted to *Medical Physics*[61,62].

- Chapter 4 presents the results of applicator gap factor calculations. The values of SSD$_{\text{eff}}$ are also calculated based on the calculated gap factors. The reasons why the gap factors do not follow the inverse-square law are explained using Monte Carlo techniques. The results in this chapter were also presented in

Zhang *et al.*[62].

- Chapter 5 discusses stopping-power ratio corrections for small fields due to the field-size change and the difference between mono-energetic and realistic electron beams if an ion chamber is used in output measurements. The main idea in this chapter is published in a paper by Zhang *et al.*[63].

- Chapter 6 talks about the calculations of ROFs for square cutouts and compares the calculations with measurements. Different dose components are analyzed. This chapter is based on another paper[64].

- Chapter 7 presents comparisons between ROF calculations, measurements and other algorithms for rectangular, circular and other irregular fields. The paper by Zhang *et al.*[61] gives the main ideas discussed in this chapter.

- A few examples of input files for *BEAM* and other user codes are given in Appendix A and supporting data in figures not used directly in the text of this thesis are given in Appendix B.
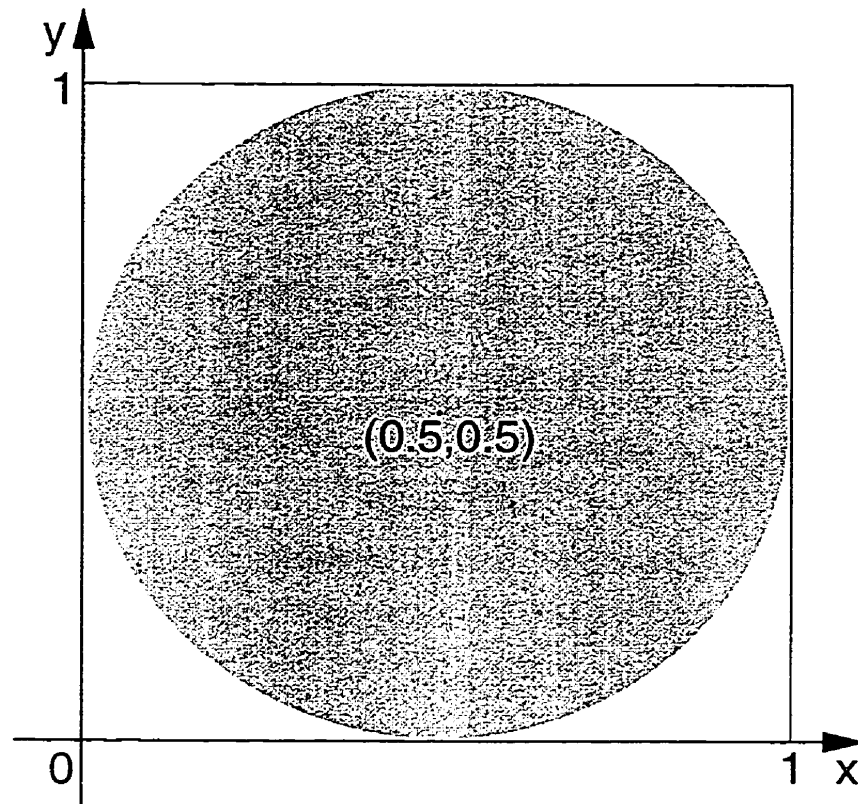
Figure 1.4: Monte Carlo calculation of the area of a circle and the value of π. The circle is centered at (0.5, 0.5). Every point (x, y) inside the circle should be $(x-0.5)^2 + (y-0.5)^2 \leq$ 0.25. A pair of random numbers uniformly distributed between 0 and 1 are picked to be (x, y) coordinates.

exit window & scattering foil

monitor chamber

jaws

SSD

No.1

scrapers

No.2

applicator

No.3
No.4

cutout

No.5

phantom
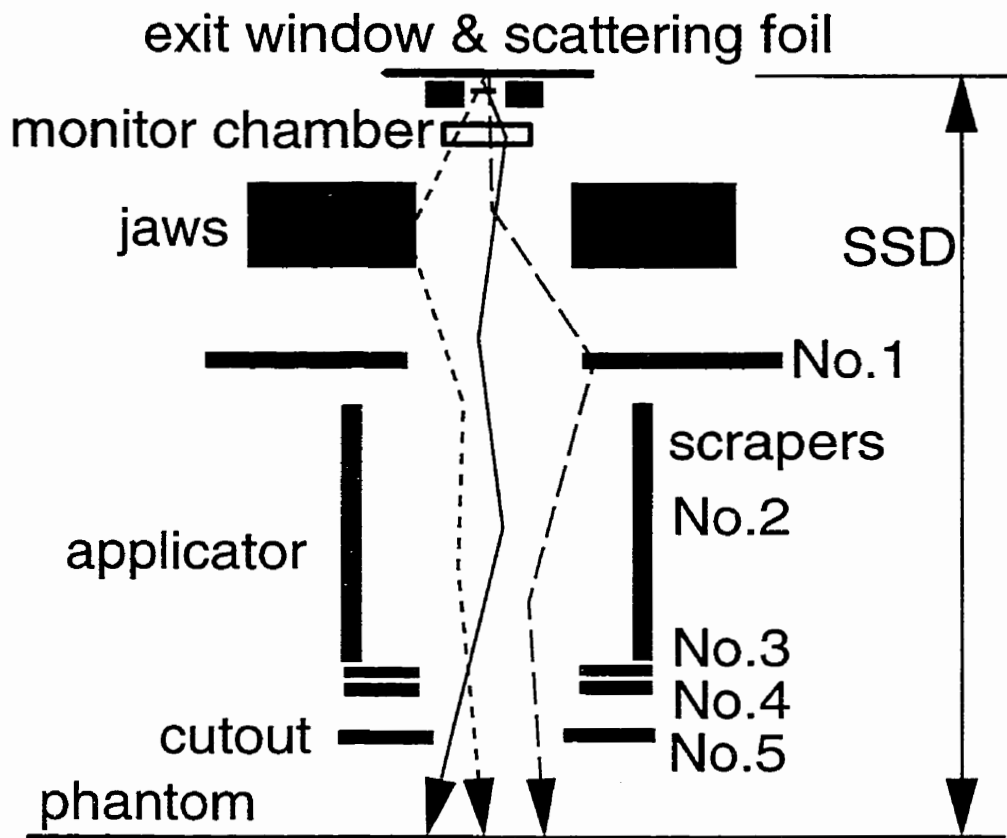
Figure 1.5: A simplified model of an MD2 Siemens accelerator head, and various electron beam paths. The long-dashed line represents electrons scattered off the applicator, the dashed line represents the electrons scattered off the photon-jaws, while the solid line represents the path of direct electrons. A cutout, if applicable, is inserted in the fifth scraper. The model used in the simulation is more realistic.

Chapter 2

Monte Carlo Simulations Using BEAM

tering, coherent (Rayleigh) scattering and photoelectric effect. The material cross section and branching ratio data are created and fit by the companion code *PEGS4* and picked up by subroutine *HATCH* for a particular simulation.
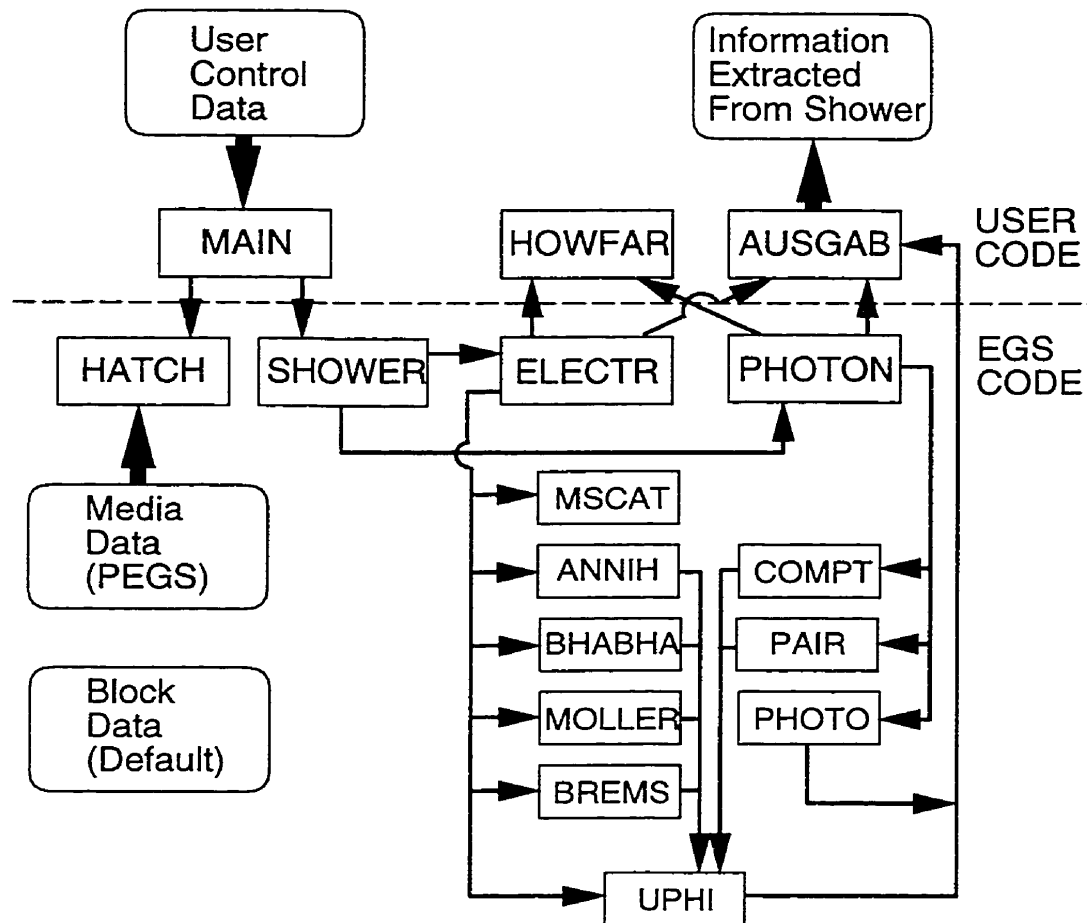
Figure 2.1: *EGS4* flow diagram, from Nelson *et al.*[39]. The part below the dashed-line is *EGS* code and above is user-code.

To use the *EGS4* code, one needs to write a user-code to define the geometry (subroutine *HOWFAR*) and to calculate parameters of interest (subroutine *AUSGAB*), such as energy deposited in a volume of a material and/or electron fluence at a plane. *BEAM*, which is coded at the National Research Council of Canada, Ottawa, as part

of the OMEGA project[77,78], is such a user-code[44,79] to model clinical radiation units, such as ^{60}Co units, electron or photon-beam accelerators.

BEAM

```
         ┌─────────────────┐
         │     Specify     │
         │   Accelerator   │
         └─────────────────┘
                  │
                  ▼
         ┌─────────────────┐
         │      Build      │
         │   Accelerator   │
         └─────────────────┘
                  │
┌──────────────┐  ▼
│cross section │ ┌─────────────────┐
│    data      │→│                 │
└──────────────┘ │  Do Simulation  │
┌──────────────┐→│                 │
│users input file│└─────────────────┘
│ –geometry    │        │
│ –incident beam│       │
│ –output spec │        │
│ –simulation  │        │
│  parameters  │        │
└──────────────┘        ▼
```

| phase space files | output listing | graphics |

| analysis programs | → | patient simulation |
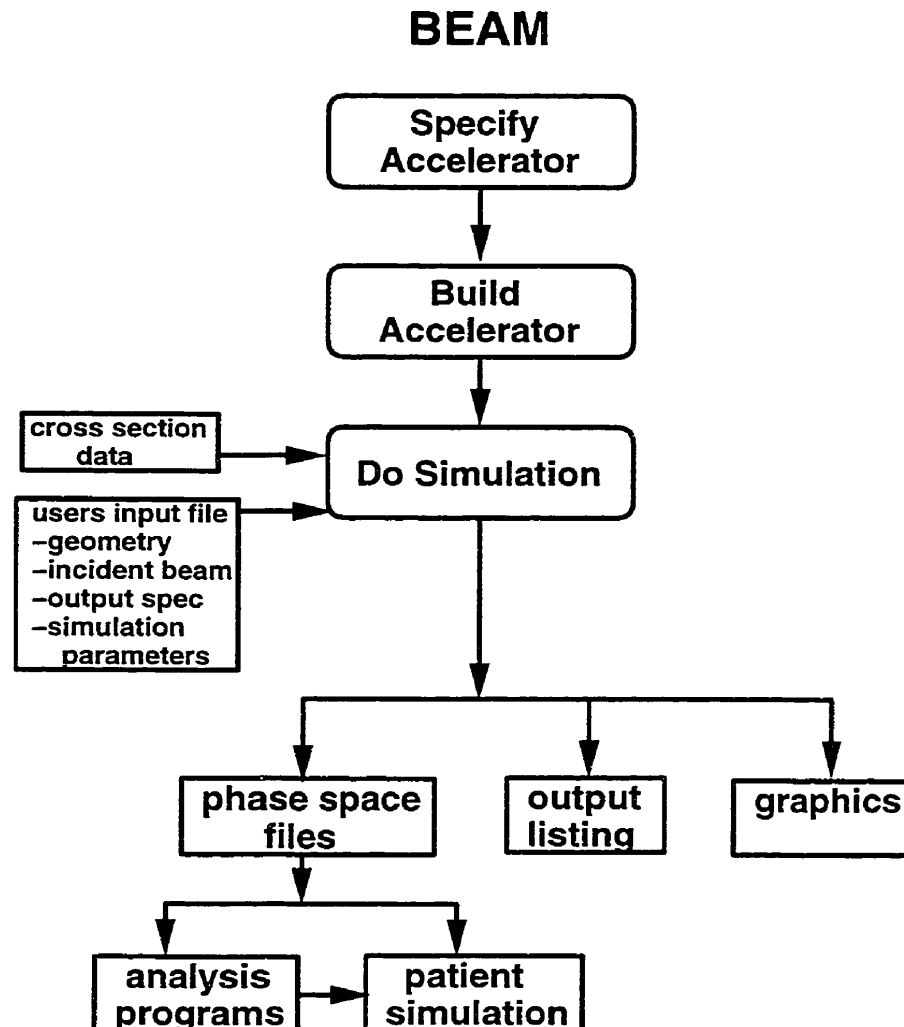
Figure 2.2: The steps involved in using the *BEAM* system, from Rogers *et al.*[44].

In *BEAM*, the geometry is defined by a series of individual component modules (CMs). Each CM occupies a slab at a right angle to the beam axis which is defined as the *Z* axis. In the simulation of the accelerator head in Fig. 1.5 (page 18), the exit window is defined by a CM of *SLABS* which can simulate multi-layer slabs of

different materials perpendicular to the beam, the monitor chamber by *CHAMBER* which also can simulate a cylindrical phantom and score dose along the central axis, the photon-jaws by *JAWS* and the applicator by *APPLICAT*. Rogers *et al.*[44,80] and Ding[79] give a full description of each CM in *BEAM*.

Another feature of *BEAM* is that it creates phase-space files at specified $X - Y$ planes in the model simulated. In the files, the position, direction, energy, charge and history tag for each particle which reaches the specified planes are stored. These files can be re-used as input particle source for another simulation, or be analyzed.

Fig. 2.2 shows how *BEAM* works. To specify an accelerator is to choose CMs which can best suit the geometry of the parts of the accelerator and put them in the order from the particle source to the end of the accelerator or the phantom. To build an accelerator is to put the relevant source code for the CMs together and edit the code so that there are no duplicate variable names in it. The next step is to compile the accelerator to create an executable file for the simulation. Then the simulation can be done with the cross section data and a users input file in which the geometry is set up in detail, the particle source is specified and the outputs are defined.

2.2 Modified and new CMs

Since *BEAM* was first released in 1995, many CMs have been modified to be more flexible in applications and many new ones have been added to the system to make *BEAM* even more powerful and practicable in clinics[80]. In this thesis, only the ones which were modified or written by the thesis author are presented, including *APPLICAT*, *CIRCAPP*, *PYRAMIDS* and *BLOCK*.

2.2.1 *APPLICAT*

The component module *APPLICAT* simulates multi-scraper applicators with rectangular or square openings and outer boundaries while the previous version, *APPSQ*, only simulated square openings and boundaries. This improvement makes *APPLICAT* more flexible. For example, to simulate an accelerator with a rectangular cutout inserted in an applicator, one no longer needs another CM for this cutout. It can be set up within *APPLICAT*. Fig. 2.3 is an example of this CM.

2.2.2 *CIRCAPP*

The difference between *CIRCAPP* and *APPLICAT* is that *CIRCAPP* models multi-scraper applicators with circular openings while *APPLICAT* models rectangular or square openings. The outer boundaries for *CIRCAPP* can also be either rectangular or square. *CONESTAK*, another *BEAM* CM, also models circular openings but also with circular outer boundaries which is not the case for applicators with circular openings. This CM was released in 1997. Fig. 2.4 is an example of *CIRCAPP*.

2.2.3 *PYRAMIDS*

PYRAMIDS now can have outer boundaries for the block materials (Fig. 2.5). The old version of this CM, which was in *BEAM*95, set the block material boundaries automatically to be the same as the boundaries of the CM, RMAX_CM, beyond which the particles are not followed. With outer-boundaries, *PYRAMIDS* can be used to model simple blocks with pyramid-shaped rectangular apertures.

APPLICAT with 2 scrapers
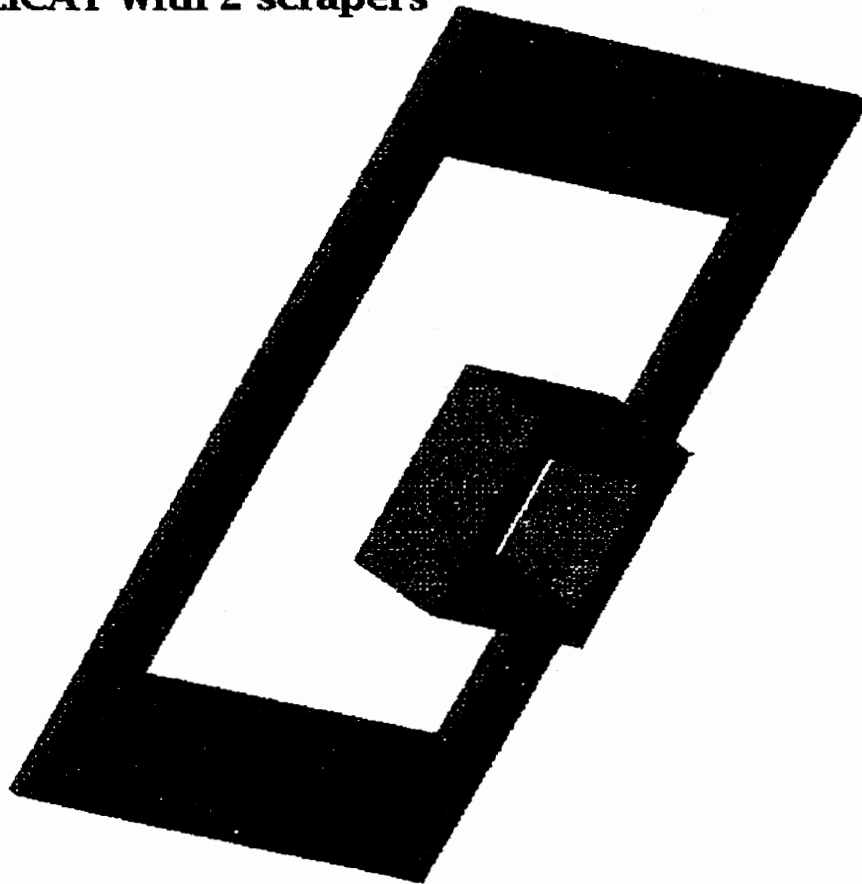
Figure 2.3: An applicator with 2 scrapers with rectangular openings and outer bound-aries modeled by *APPLICAT*. The half-width in the X and Y-direction for each opening and boundary are specified independently. This and similar figures are produced via the EGS_windows display package and standard output from *BEAM*.
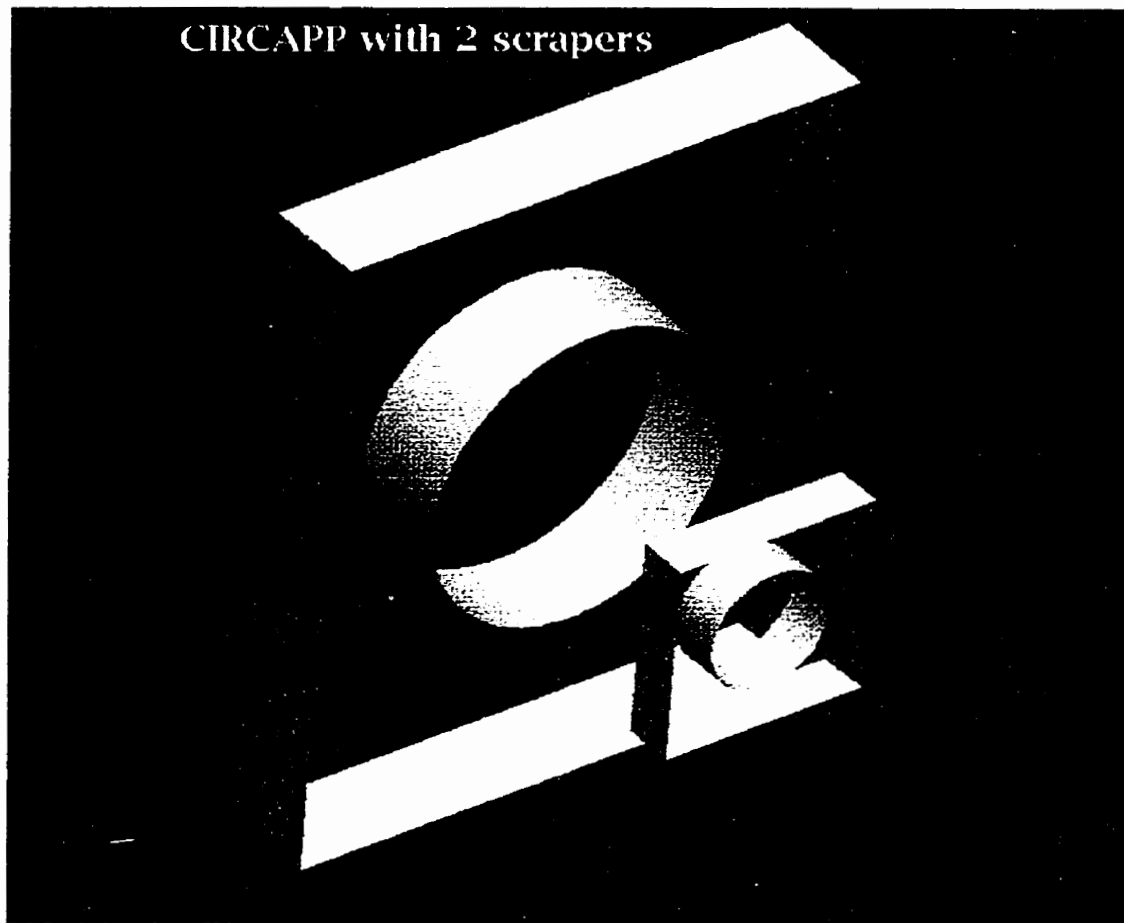
Figure 2.4: An applicator with 2 scrapers with circular openings and rectangular outer boundaries modeled by $CIRCAPP$. The radii for the openings and the half-width in X and Y-direction for the boundaries are specified independently.

Beam Axis
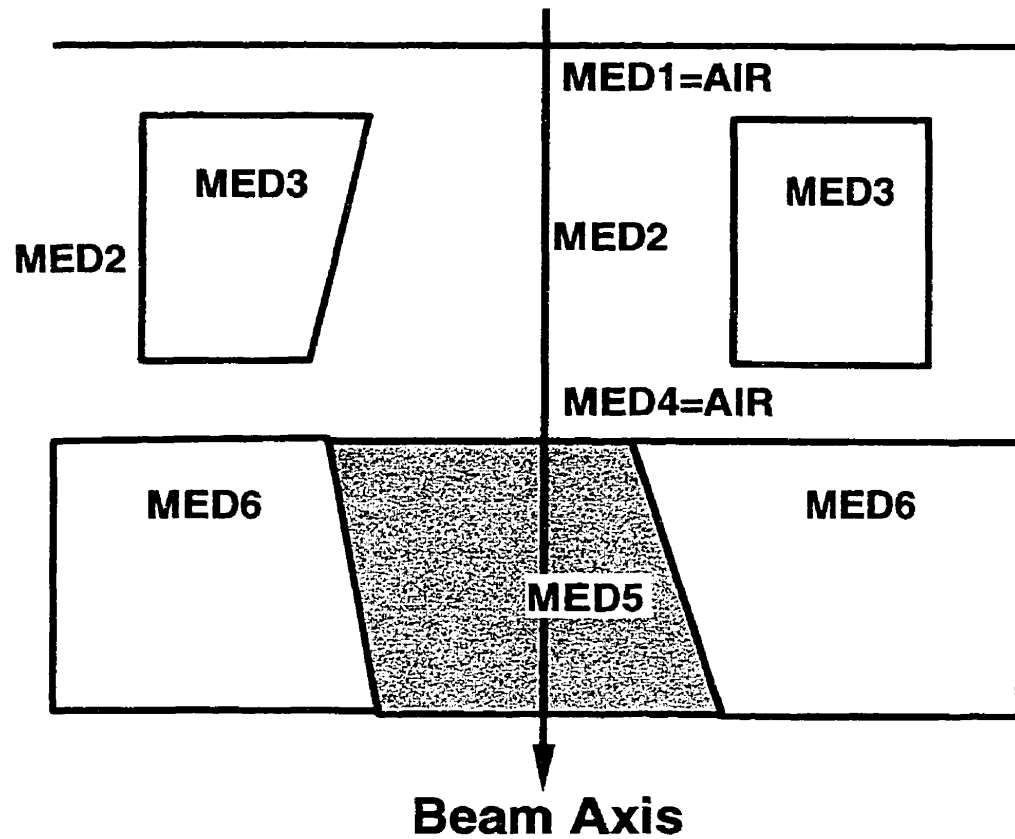
Figure 2.5: A side view of *PYRAMIDS*, from Rogers *et al.*[80]. Before the modification, there was no outer boundary for this CM.

2.2.4 *BLOCK*

BLOCK can be used to simulate a single layer cutout or block with single or multiple-openings of arbitrary shape. It allows for edges which converge to an arbitrary focus along the beam axis. This CM has been in *BEAM* since 1996. Fig. 2.6 and 2.7 is an example of a *BLOCK* simulation.

One of the limitations of this CM is that it can only shape an opening by straight lines. For a curved opening edge, one has to use multiple lines to approximate the curve. For example, a circle can be approximated by a 25-sided polygon.
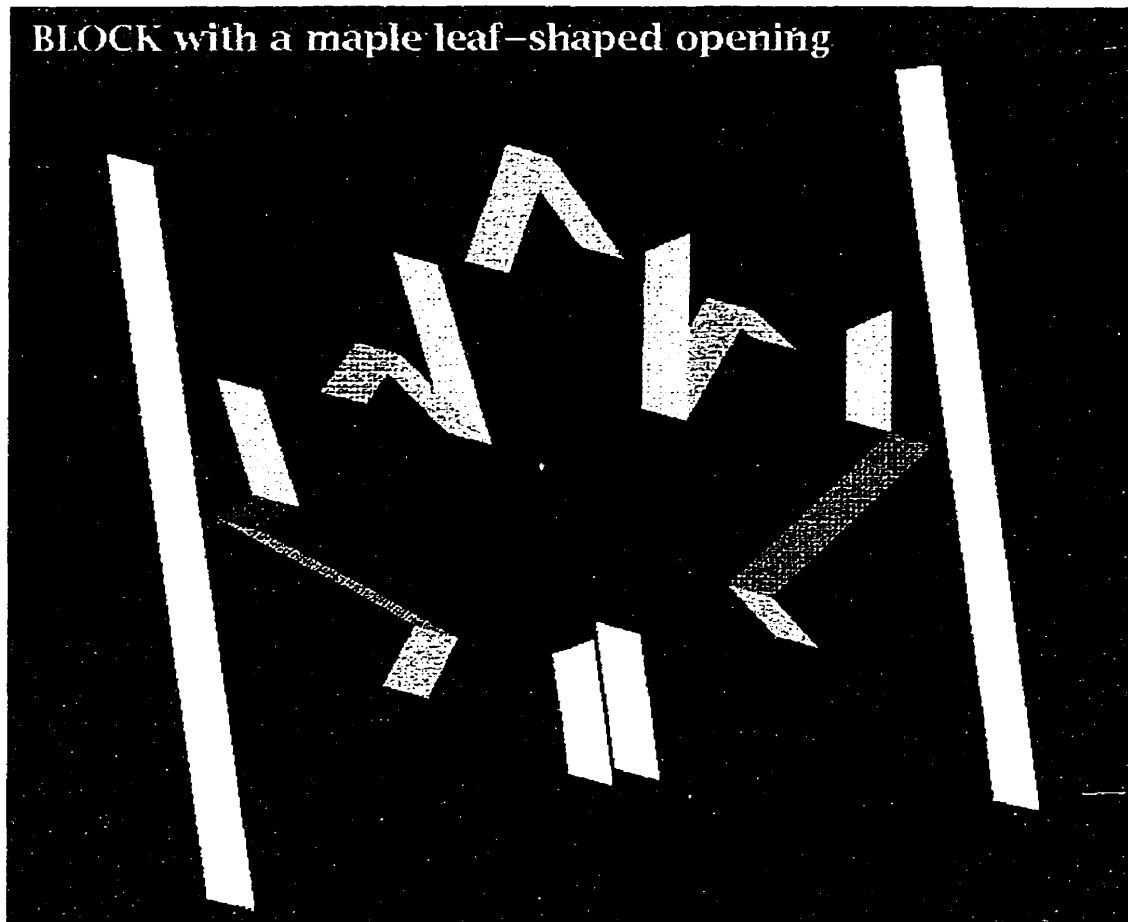
Figure 2.6: *BLOCK* with a maple-leaf shaped opening. This CM can also simulate multiple irregular openings on a rectangular block. The input file for this maple leaf-shaped cutout is given in Appendix A.
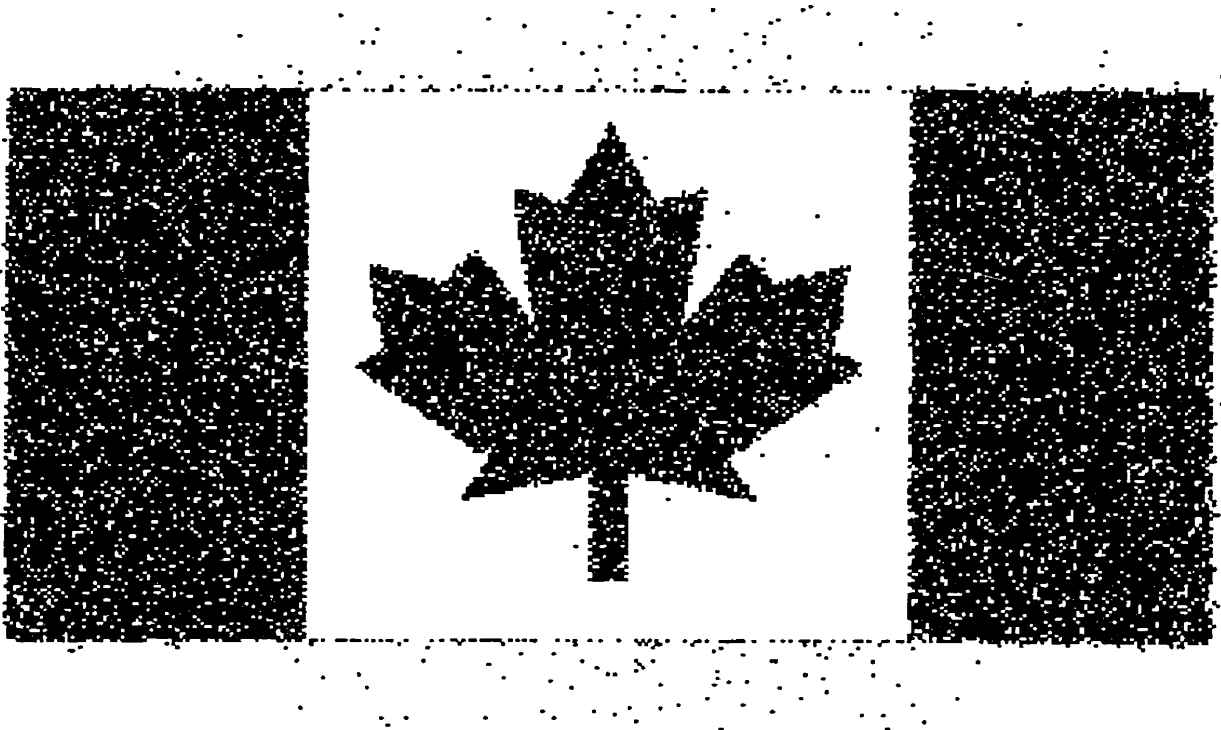
Figure 2.7: Particle distribution at a plane behind and parallel to the block shown in Fig. 2.6 when a rectangular-parallel electron beam is incident on the block in the direction perpendicular to the opening surface. Every dot represents a particle in the plane. This figure is obtained by analyzing the phase-space file.

Usually, one layer of irregular cutout is all that is needed to simulate clinical applications, however, it might be the case that more than one layer of irregular opening inserts are needed and this can be done by using *BLOCK* more than once in an accelerator simulation. In simulations for MD2 applicators, *BLOCK* is used several times to simulate the scrapers with rounded-corner openings.

Since *BLOCK* can easily be used to simulate square or rectangular openings, in principle, it can replace *APPLICAT* in simulating a square or rectangular cutout. But *APPLICAT* has the advantage of multi-layers. Also, *BLOCK* runs much more slowly

due to its complicated geometry programming. In the calculations, *APPLICAT* is used for square and rectangular fields, and *CIRCAPP* for circular fields.

With *BLOCK*, *BEAM* can be applied in ROF calculations for irregular fields in clinical treatment planning, which could save a lot of labor and time.

2.3 Monte Carlo calculation of ROFs

2.3.1 General methods

The *BEAM* code is used to simulate the beams from an MD2 accelerator and a Clinac 2100C accelerator and the dose deposited in a water phantom. Usually, a complete simulation of an electron beam and the dose deposited in the phantom consists of two steps.

The first step is to simulate the transport of particles inside the accelerator head, and create a phase-space file at the end of an applicator or just before the last scraper where the cutout is inserted. The geometry is set up according to the design blueprint provided by the manufacturer. The cross section data for the materials used in the accelerator are produced by *PEGS*4, the preprocessor of *EGS*4, before any simulation of the accelerator. The phase-space files for the ROFs calculations are output at a plane right before the cutout.

The accelerator head is composed of a series of component modules which represent the exit window, primary collimator, scattering foil, monitor chamber, x and y photon-jaws, applicator, and so on. A mono-energetic electron pencil beam is incident on the exit window in the simulations discussed in this thesis. A previous study by Ding *et al.*[81] showed that there is little difference in the depth-dose curves using either mono-energetic or symmetric spectra sources incident onto the exit window. We start the simulation by selecting incident electron energies to fit the R_{50}s (the

depth of 50% of maximum dose in phantom) of the measured depth-dose curves for the open 10×10 cm^2 applicator and use the selected energies to simulate beams with other applicators and cutouts. The incident electron energies on the exit window are usually higher than the nominal beam energies. For example, the incident energy for 11 MeV beam simulations is 11.95 MeV, however, at the surface of the phantom, the mean energy of the 11 MeV beam inside the 10×10 cm^2 field is about 10.5 MeV. For smaller beams the value of R_{50} decreases substantially. This is not due to the change of the mean energy in the beam but is entirely an in-phantom effect which is discussed in detail in following sections. For example, the average energy on the phantom surface in the 2×2 cm^2 11 MeV beam is 10.6 MeV, even slightly larger than that of the 10×10 cm^2 field despite the fact that R_{50} decreases from 4.5 cm for the 10×10 cm^2 field to 3.6 cm for the 2×2 cm^2 field.

From the exit window, the particles travel in the geometry defined by the component modules. Fig. 2.8 is an example of the *BEAM* simulation of Siemens MD2 accelerator and its electron beam.

The second step in calculating the dose in the phantom is to use the phase-space file created in the first step to simulate the particle transport through the last scraper or cutout and in the phantom, which gives the depth-dose curve along the central axis in the phantom. The component module *CHAMBER* is used to simulate the phantom since the concern is the dose along the central axis, which is one of the features of *CHAMBER*. For dose profiles at different depths in the phantom, *DOSXYZ*, another users-code of *EGS*4, is used. In this second step of the simulation, the depth bin size and central volume radius in which the dose is calculated are set up according to the detector size. Fig. 2.9 † presents two pairs of depth-dose curves for an MD2 accelerator and Fig. 2.10 presents the depth-dose curves for small fields to demonstrate that the agreement between the calculations and measurements is very

---

†Axis labels follow the ICRU (International Commission on Radiation Units and Measurements) convention that axis labels are quantities divided by units to give pure numbers.
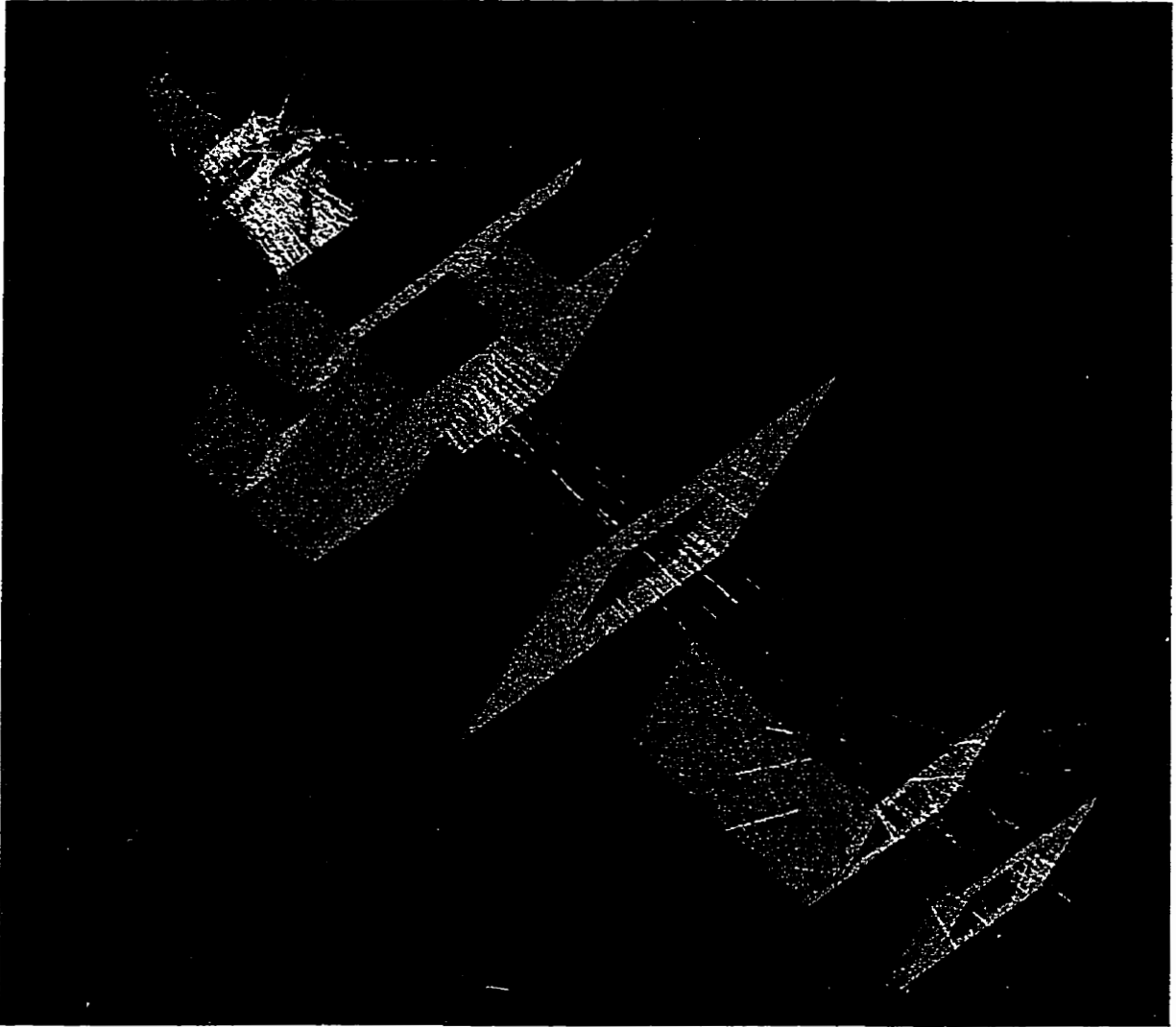
Figure 2.8: *BEAM* simulation of Siemens MD2 electron beam accelerator. The last scraper, corresponding to No. 5 in Fig. 1.5 (page 18), where the cutout is inserted, is 5 cm above the phantom surface. Electrons are represented by blue lines while photons are yellow lines. In this example of nominal 11 MeV electron beam, there are 200 incident electrons and 10 electrons, 24 photons registered at the scoring plane which is at the phantom surface.
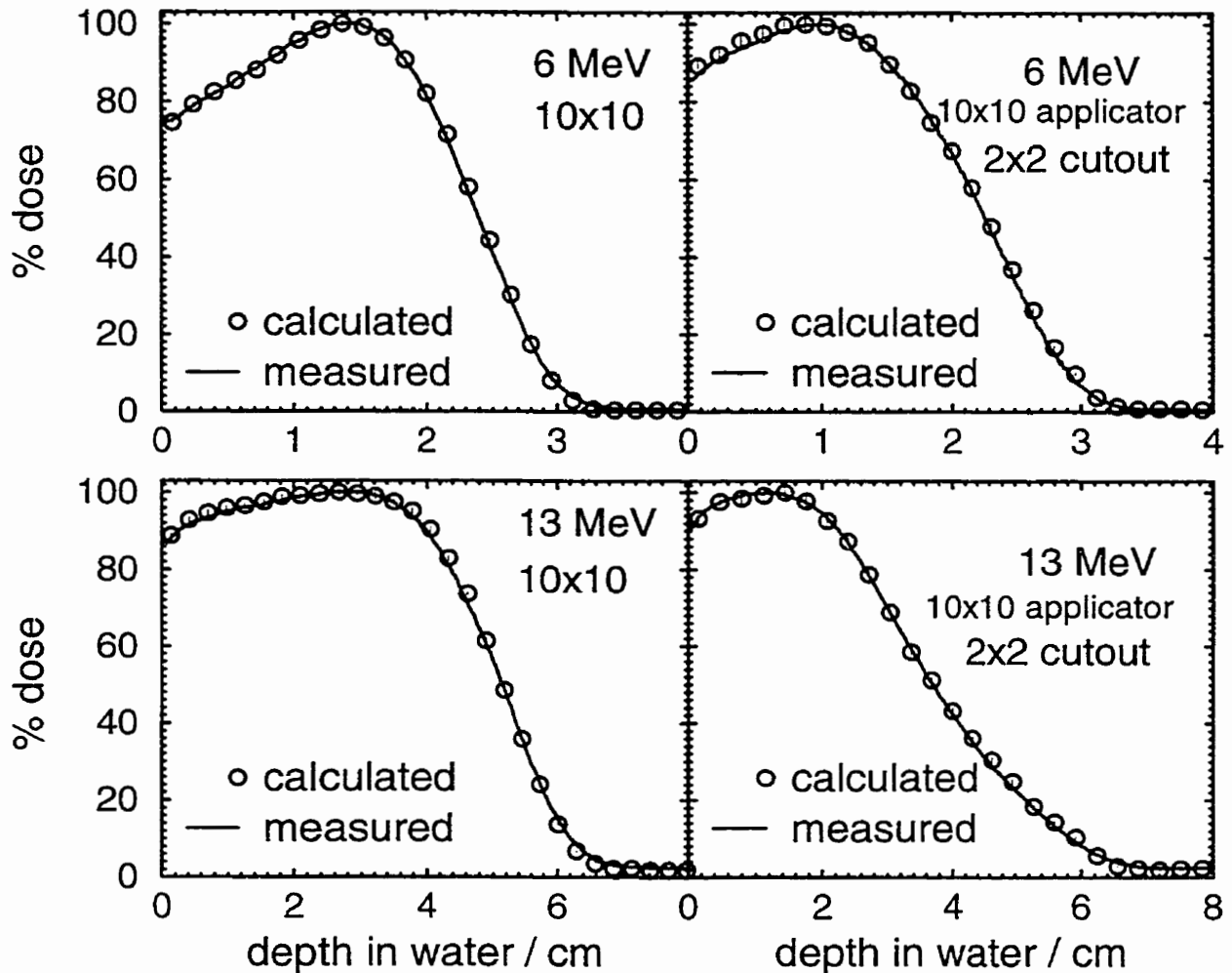
Figure 2.9: Depth-dose curves of 6 and 13 MeV beams at SSD = 100 cm for Siemens MD2 accelerator. A 10×10 cm^2 applicator is used. The measurements are done at the Ottawa Regional Cancer Centre by Dr. Joanna Cygler using a silicon diode detector. The Monte Carlo calculations agree with measurement very well.
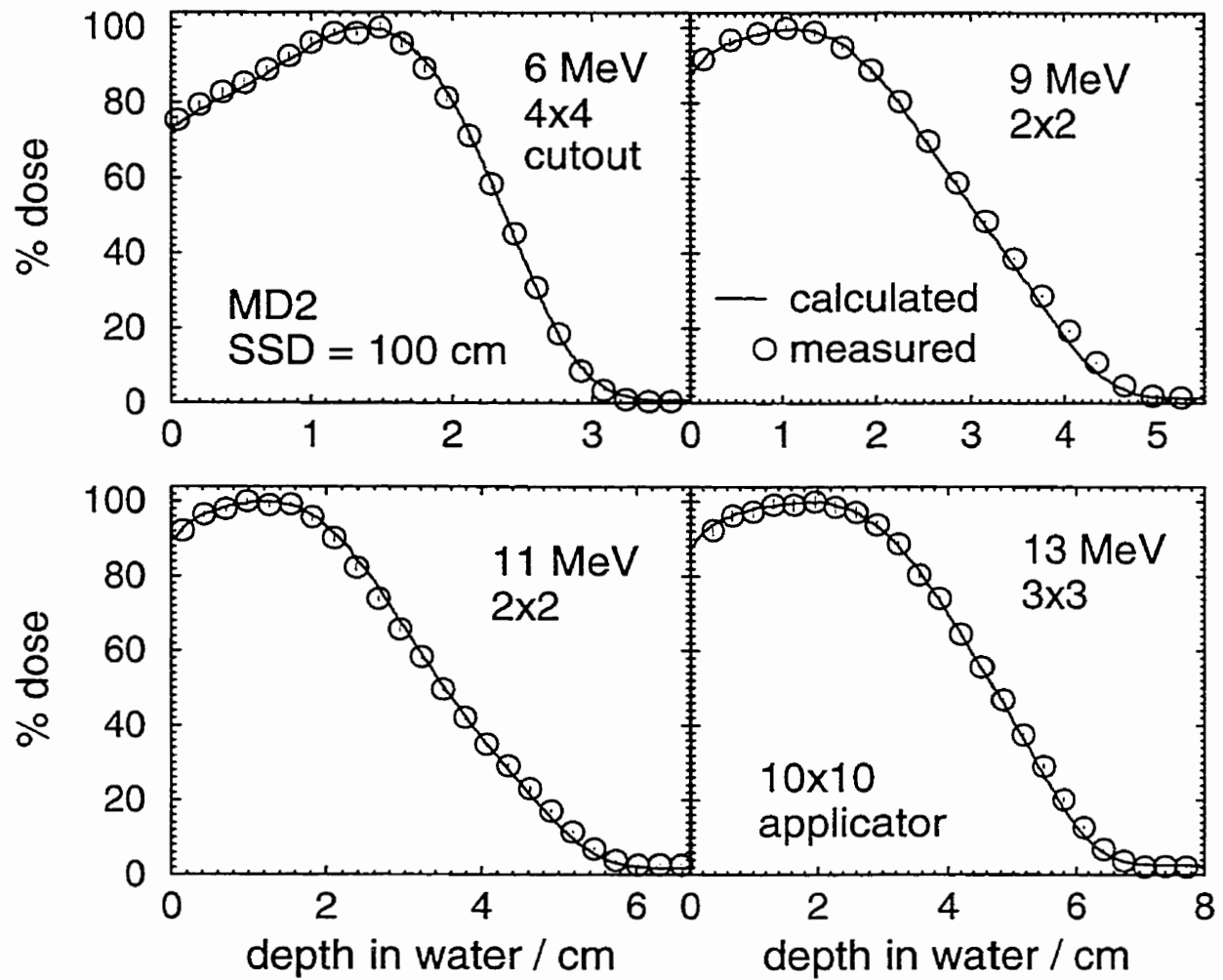
Figure 2.10: Depth-dose curves for small fields of 6, 9, 11 and 13 MeV beams at SSD = 100 cm for Siemens MD2 accelerator. The curves for a 2×2 cm^2 field for 6 and 13 MeV beams are shown in Fig. 2.9. A 10×10 cm^2 applicator is used.

good (further data are presented in Appendix B). The statistical uncertainties in all Monte Carlo calculations in this thesis are obtained by dividing the total simulation into ten batches. The calculated value is the mean value of the ten batches and the square of the one standard deviation uncertainty s^2 on the mean value is calculated as:

$$s^2 = \frac{1}{n(n-1)} \sum_{i=1}^{n} (x_i - \bar{x})^2 \, , \tag{2.1}$$

where $n = 10$ in all cases, x_i is the value from the ith batch and $\bar{x}$ the mean value.

Although the concern of this thesis is ROFs, *i.e.*, the maximum dose along the central axis, to implement Monte Carlo methods in clinical treatment planning, which is the ultimate goal of the research work in which this thesis program is involved, the dose profiles must also agree with measurements very well. So far, this agreement has not been reached for large fields for an MD2 accelerator using a small incident pencil beam on the exit window (Fig 2.11). Ding and Rogers[82] showed that the calculated dose profiles for many other accelerators agreed with measurements very well, although their studies were restricted to 10×10 cm^2 applicators. Preliminary results of a study on this profile problem show that the profiles can be flattened by introducing a beam divergence in the initial electron beam, *e.g.*, using a point source incident on the exit window to make the direct component flat. This source type does not significantly change the depth-dose curves or ROFs.

2.3.2 Monitor units

In the simulations, there is a monitor chamber inside the accelerator. The dose is registered in the monitor chamber in the same way as that in the phantom, *i.e.*, dose per particle incident on the exit window. For applicator factors, since the photon-jaw setting changes with applicator size, dose per incident particle in the monitor chamber changes slightly with applicator size due to different backscattering from the photon-jaws[79,83,84]. For example, for MD2 6 MeV beams, when the field size decreases from
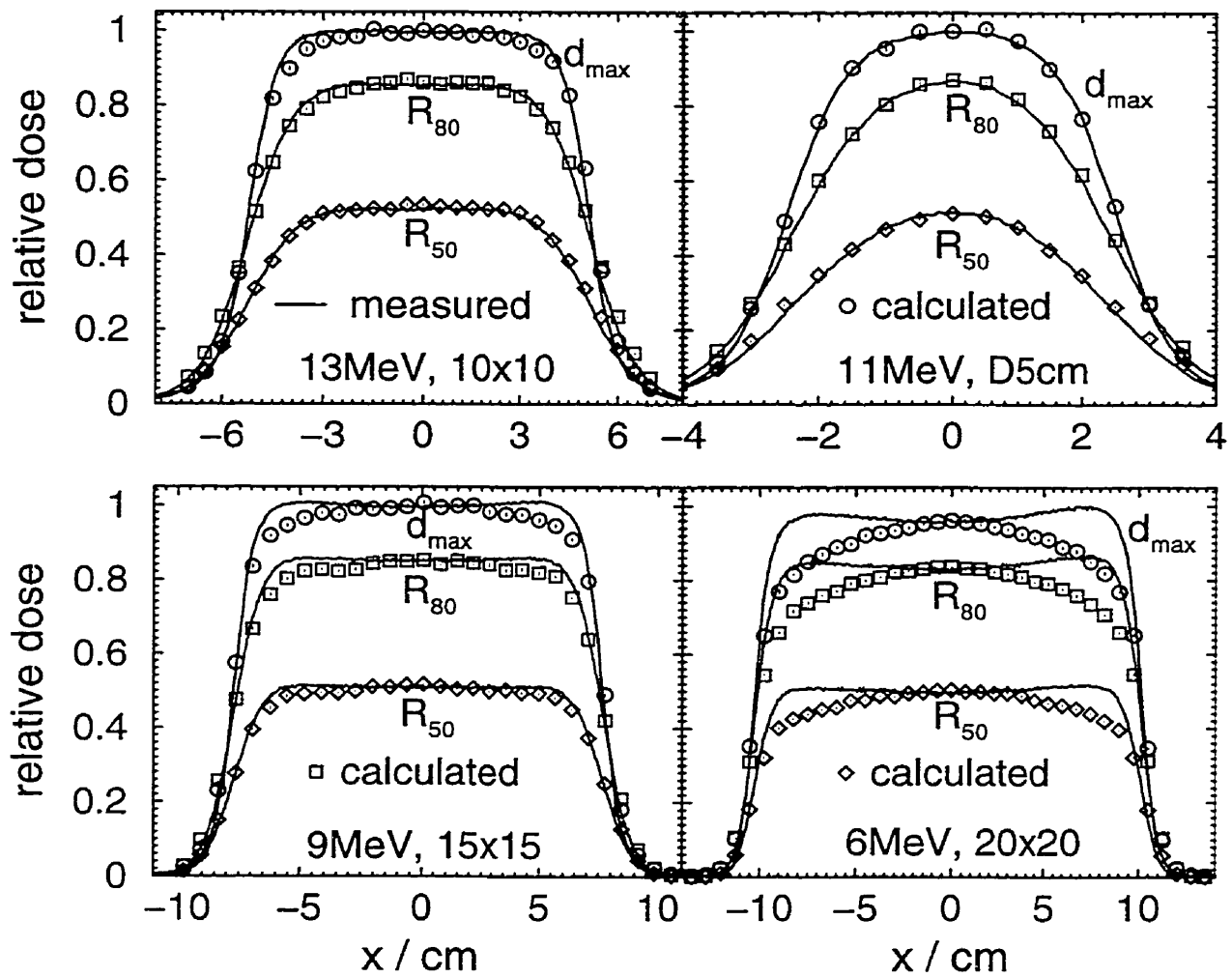
Figure 2.11: The calculated dose profiles are not as flat as measurements at the top for an MD2 accelerator, especially for large fields. In the figure, D5cm stands for a circular field of 5 cm in diameter.

20×20 cm^2 to the circular field of 5 cm in diameter, the dose in the monitor chamber per particle incident on the exit window increases by 0.7%. For this reason, dose in the phantom needs to be normalized to the dose in the monitor chamber to get the quantity dose per monitor unit.

As long as the setting of the photon-jaws and the applicator size are not changed, *e.g.*, with different cutouts, the dose deposited in the monitor chamber per incident particle on the exit window is the same. Thus, in the calculations of cutout factors, dose at d_{max} per electron incident on the accelerator vacuum window is used as the beam output instead of dose per monitor unit.

2.3.3 Applicator factors

Among the ROFs, applicator factors are relatively more difficult to calculate. In this study, applicator factors are calculated for a Siemens MD2 and a Varian Clinac 2100C accelerator. Both accelerators work in this way: when the applicator size is changed, the photon-jaw setting is also changed. For the MD2 accelerator, the scattering foils also vary with energy, and for the Clinac 2100C, different energies use different photon-jaw settings. All these changes imply that each applicator factor corresponds to a new geometry in the accelerators. The discussion in Chapter 3 will show that applicator factors are very sensitive to the geometry of the collimation system. To calculate accurate applicator factors, the geometry simulation must be very accurate. More discussion on the geometry sensitivities for ROFs is given in Chapter 3 and 6.

2.3.4 Gap factors

The component module *APPLICAT* in the *BEAM* code is for the simulation of applicators. It can simulate square and/or rectangular openings. In an MD2 machine, all applicators have rounded corners. For the large size applicators, the area that is

being irradiated could be 2% less due to the rounding of the corners compared to the opening with right angle corners. We use the *BEAM* component module *BLOCK*, which in principle can simulate any shape of opening, to simulate the applicators with rounded corners. At SSD = 100 cm, there is a negligible difference in the dose at d_{max} in the phantom between the simulations with *APPLICAT* and *BLOCK*, however, at extended SSDs, there is a difference of up to 3% for reasons discussed in the next section.

BLOCK is also used in the simulation of the circular opening applicator with square outer-boundaries. When these calculations were performed, there was no other component module in the *BEAM* code that could model this geometry combination. Though *BLOCK* was used to approximate circular fields using a 25-sided polygon, the comparison between the calculations and measurements shows that this approximation is good enough for the gap factor calculations. After these calculations were completed, we completed a new component module, *CIRCAPP* (section 2.2.2), which models this geometry combination, *i.e.*, the circular applicator. *CIRCAPP* is about two times faster than *BLOCK* in simulating the circular applicator since *BLOCK* is more general.

2.3.5 Cutout factors

In this study, cutout factors are calculated for an MD2 accelerator. The cutout is made of cerrobend, a bismuth(50.0% by weight)-lead(26.7%)-tin(13.3%)-cadmium(10.0%) alloy. The sizes of the opening are between 1.9×1.9 cm^2 (defines a field size of 2×2 cm^2 at SSD = 100 cm) and the open applicator, all with a thickness of 1.2 cm.

The cutout simulation together with the dose deposition simulation in the phantom is done so that the phase-space file for the rest of the accelerator simulation can be used repeatedly for all the cutout sizes. The same phase-space file is also used in the calculations at extended SSDs. For an SSD of 115 cm, one just needs to put the

chamber with a 1 cm long air cavity is used in the output measurements. All the $(\bar{L}/\rho)_{air}^{water}$ calculations are based on the stopping powers of ICRU Report 37[87], and $\Delta = 10$ keV. The statistical uncertainty (1σ) on the $(\bar{L}/\rho)_{air}^{water}$ calculations is 0.1% or less.

2.3.7 Important *BEAM* input variables

The values of some important *BEAM* input variables, such as *ECUT* (cutoff energy for electrons), *PCUT* (cutoff energy for photons), *ESAVE* (the maximum charged particle energy in MeV at which range rejection is considered), *ESTEPE* (the maximum fractional energy loss per electron step), *etc.*, can affect the accuracy and efficiency of a simulation[52,88]. For dose in-phantom calculations, *ECUT*, *PCUT* can be quite high[52,88], thus in the simulations, *ECUT* = 0.7 MeV and *PCUT* = 0.01 MeV. *AE*, the threshold energy for secondary electron production, is 0.7 MeV which corresponds to 189 keV kinetic energy. For similar reasons, *ESTEPE* is set to 0, which means there is no *ESTEPE* control and *PRESTA*, an algorithm for electron transport, is used to determine the default step-size so that the fastest simulation can be reached. To save simulation time, the range-rejection technique is used in all simulations in the mode that a history is terminated if the energy of the electron is less than *ESAVE* and the electron cannot escape from the current region with E > *ECUTRR* (*ECUT* for the current region). *ESAVE* is set to 2.0 MeV, a moderate value, so that not too many bremsstrahlung events are lost. For in-phantom simulations, range rejection is also done on a region-by-region basis.

2.4 Simulation time

The simulation time is applicator size and beam energy dependent. An accelerator simulation for a 11 MeV beam with a 10 × 10 cm² applicator takes about 6 hours of

CPU time on a single Pentium Pro 200MHz PC with Linux system to create about 1.4 million particles in the phase-space file which takes about 40 Mbytes of disk space. This typical file implies an uncertainty in the on-axis number of electrons in a 1 cm^2 area of about $\pm$ 1%. The second step for various cutout sizes takes about 1–2 hours of CPU time. This typical phase-space file size for a large field gives statistical uncertainties on the dose at d_{max} of about 1%.

3.1   Why applicator factors are difficult to calculate

Accelerators from different manufacturers have different collimation systems. Fig. 2.8 (page 32) and 3.1 show the simulated accelerators of Siemens MD2 and Varian Clinac 2100C. The value of an applicator factor depends on not only the beam energy, field size, but also the collimation system. Therefore, different accelerators have different applicator factors even for the same energy and field size. That is why applicator factors are hard to predict without details of the collimation system. Since many other algorithms do not have the ability to include the effects of different collimation systems, they are usually used to predict cutout factors for which only the cutout size changes while the rest of the collimation system remains the same.

Monte Carlo methods, on the other hand, model the geometry of the whole collimation system and hence they take care of any effect of the collimation system. This is an advantage of Monte Carlo methods. Applicator factors for different models of accelerators can be calculated explicitly. But this is also a disadvantage. Without correct details of the collimation-system geometry, Monte Carlo may give wrong answers. The correct applicator factors for a Siemens MD2 accelerator could not be calculated until a ring was found to be wrongly inserted between the monitor chamber and the photon-jaws in the simulations. This ring, which was "outside" the beam, had a blocking effect[62] on the beam outputs and caused discrepancies in applicator factors of up to 4%. At the same time we were able to accurately calculate the central-axis % depth-dose curves for the applicators and cutout factors. The blocking effect, *i.e.*, the prevention of electrons outside the beam reaching the phantom, is discussed in Section 3.2.3 and Chapter 4. To simulate the correct geometry is usually the hardest part of Monte Carlo calculation of applicator factors. Because of this problem, some measurement data are still necessary to make sure Monte Carlo works correctly.

3.2 Results

3.2.1 Applicator factors

Applicator factors are calculated for a Siemens MD2 accelerator for 6, 9, 11 and 13 MeV electron beams for applicators of 5 cm in diameter, 10×10, 15×15 and 20×20 cm^2, and for a Varian Clinac 2100C accelerator for energies between 6 and 18 MeV electron beams for applicators of 6×6, 10×10, 15×15 and 20×20 cm^2. The agreement between the calculations and measurements is better than 1% for all cases except for the 6 MeV beam with a 5 cm diameter circular applicator (Fig. 3.2) which agrees within 2% for the MD2 cases and 1.5% for the Clinac 2100C cases (Fig. 3.3). The statistical uncertainties on the calculations are about 1%. Due to the difference in collimation systems, applicator factors for these two accelerators are completely different in pattern even for the same energy. More comparisons of calculated and measured applicator factors can be found in Appendix B.

3.2.2 Side-scatter equilibrium

The idea of side-scatter equilibrium is very important in understanding the relative output from the direct electrons which dominates the total output. At the collimator level, if more than 99% of the particles that could reach the point of interest in the phantom pass through the collimator opening, side-scatter equilibrium is said to exist at that point[5,64].

To study the variation of relative output factor and side-scatter equilibrium at d_{max} as a function of field size and energy, we simulated parallel mono-energetic electron beams of different energies incident on a water phantom with field sizes from 2 to 20 cm in diameter (Fig. 3.4). The study shows that for a given beam energy there is a critical field size needed to establish side-scatter equilibrium at d_{max} in the
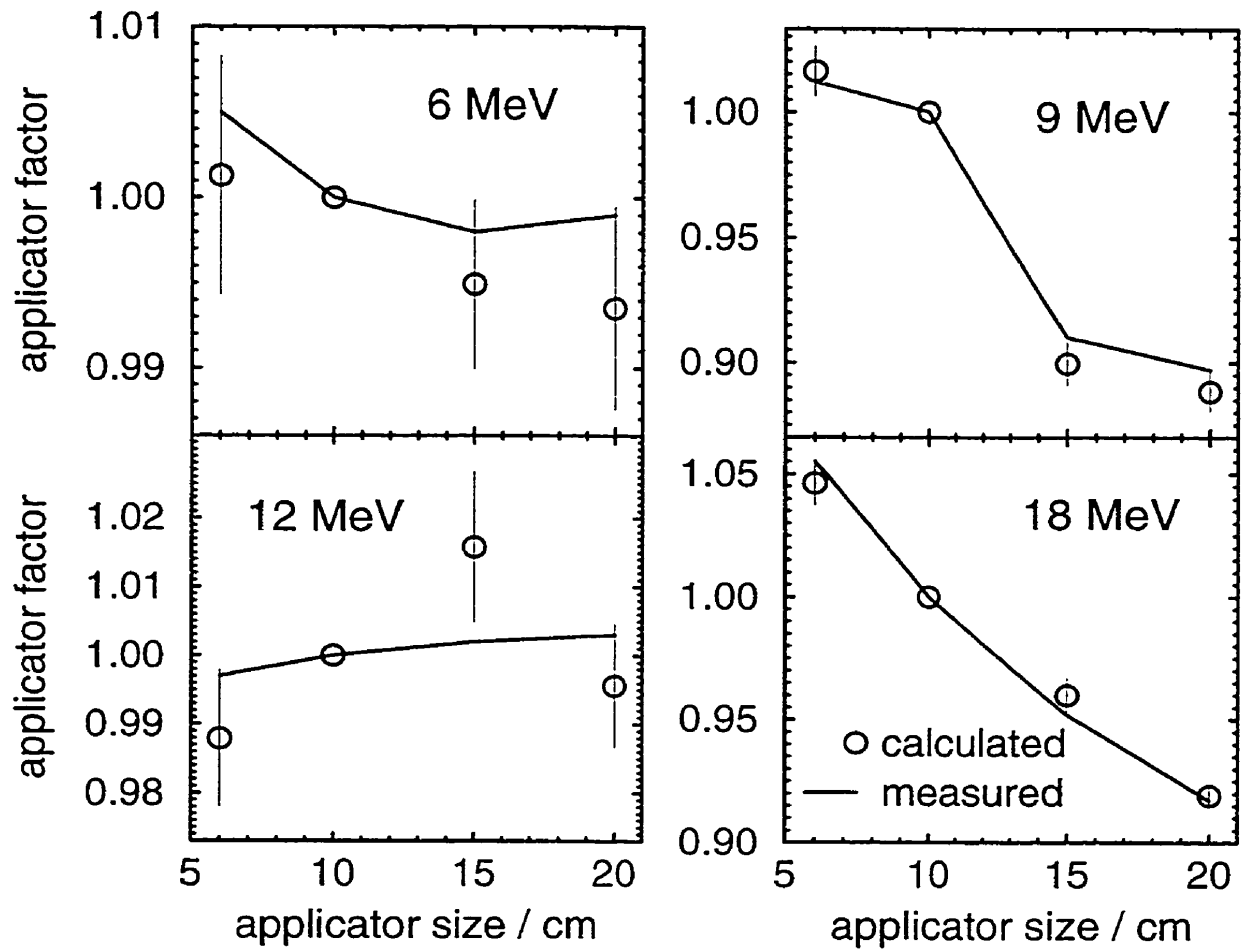
Figure 3.3: Measured vs calculated applicator factors for a Varian CLINAC 2100C accelerator at 6, 9, 12 and 18 MeV. The agreement between calculations and measurements is better than 1.5% in all cases studied. All the measured ROF data shown in this figure, except ROFs for 9 MeV beams, were measured at the University of Wisconsin. ROFs for 9 MeV beams were measured by the RPC of Houston.

phantom (Fig. 3.5). It is not necessarily true that the higher the energy is, the larger the field size to reach side-scatter equilibrium at d_{max} should be. Figs. 3.4 and 3.5 show that the 40 MeV beam reaches the 99% dose criterion before the 30 MeV beam does as the field size increases.

As long as side-scatter equilibrium at d_{max} is established, no matter how much wider the opening of the collimator is, the dose at d_{max} from the direct electrons will remain the same, and hence the total output usually changes little since the direct electrons often dominate the total output of the beam. Thus it is a "broad beam" output[18,65,89–91].

A detailed dose-component analysis is presented in Chapter 6.

3.2.3 Blocking and outscattering effects

An implication of a broad beam is that the output does not change if the beam size is larger. For non-broad beams (or narrow beams), the lack of side-scatter equilibrium at d_{max} reduces the output[5,19]. The lack of side-scatter equilibrium is usually due to tight collimation at different levels along the beam axis. We call this effect from the collimation system the "blocking effect". In addition to the blocking effect, the "outscattering" of the beam between the last collimator and phantom surface due to air scattering makes the output of a beam even smaller.

Fig. 3.6 explains what these effects are. Although the projected field at the phantom surface might be "broad" if it were defined at the phantom surface, with an air gap between the collimator and the phantom surface, the electrons represented by the dashed lines in Fig. 3.6 could be scattered back into the field by the air if there were no collimator, but they are stopped by the collimator, which means that the side-scatter equilibrium is not established yet for this projected "broad" beam. The photon-jaw setting is usually wide, *i.e.*, "outside" the beam, but with a thick air gap between the photon-jaws and the phantom surface, the beams defined by the photon-jaws could
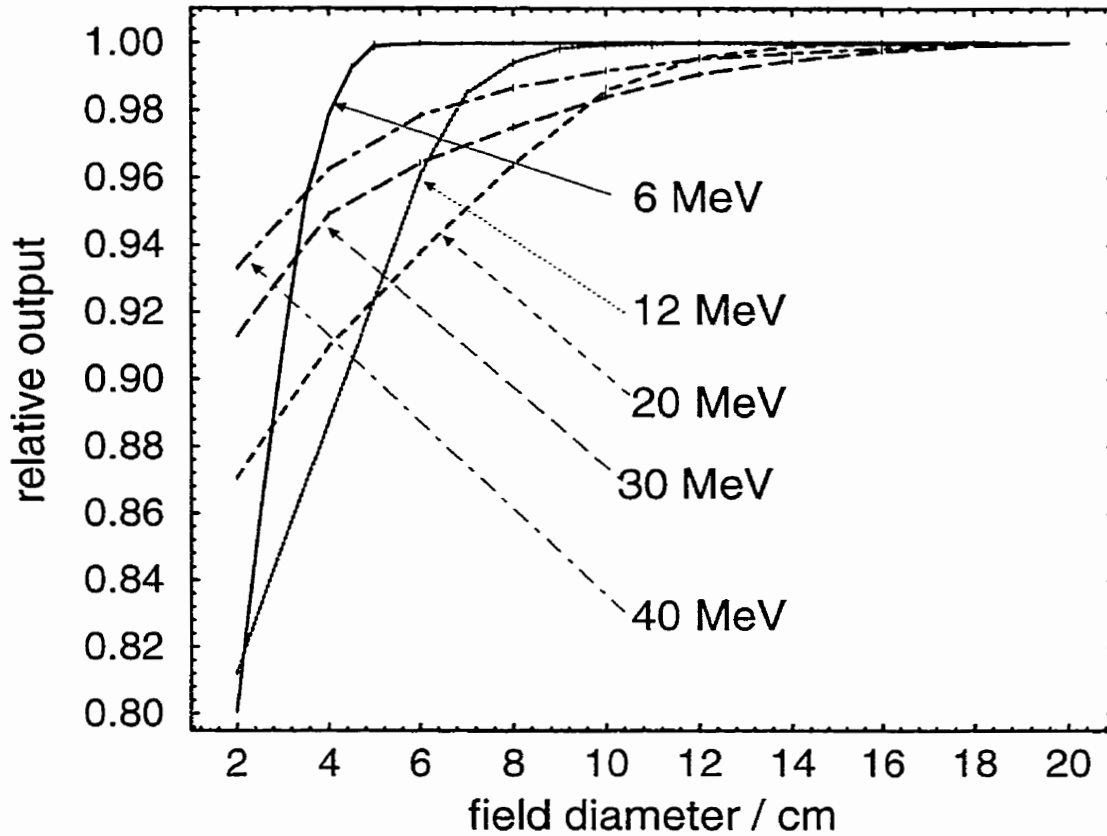
Figure 3.4: Calculated relative output versus circular field size for mono-energetic parallel electron beams. Each beam is incident from vacuum on a water phantom. For each energy, the output reaches a plateau. This means side-scatter equilibrium at $d_{\max}$ is established. The field size to establish side-scatter equilibrium at $d_{\max}$ is energy dependent. All the curves are normalized to their own outputs at a field diameter of 20 cm which is wide enough for all these energies to have side-scatter equilibrium at $d_{\max}$. For the field with radius ∞, the output of the beam is less than 0.1% larger than that of the 20 cm diameter field for all the energies.
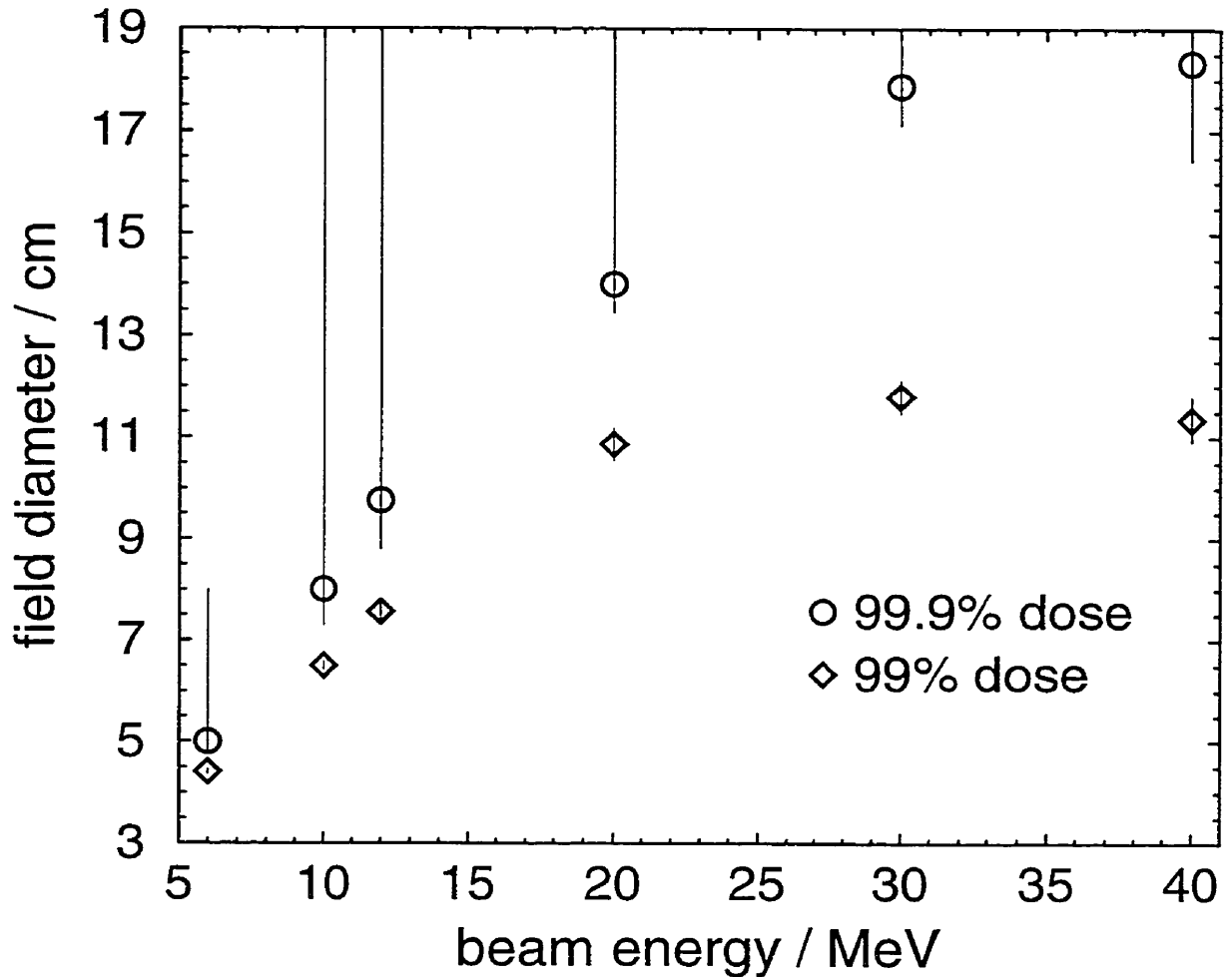
Figure 3.5: Energy dependence of the field size to establish side-scatter equilibrium at $d_{\max}$ defined in terms of dose as a fraction of a broad beam dose. For the 40 MeV beam, the field size to establish side-scatter equilibrium at $d_{\max}$ is smaller than that of 30 MeV beam if 99% of dose maximum is the criterion. The upper error for the 99.9% dose curve is meaningless because the error bars on most dose calculations are larger than 0.1% which makes most of the low dose within the error bar never reach 99.9% criterion, and hence the upper error for the field size to reach 99.9% dose is infinity for most cases.

be non-broad beams. In the other words, due to the blocking effect, the photon-jaw setting still affects the output of a beam. This effect is more significant for low-energy beams because the scattering of particles in air is more significant. Also, the smaller the field size, the more significant the effect, because the collimation system stops more particles which could be scattered back into the beam.

Fig. 3.7 shows how the blocking effect of the photon-jaw affects the relative output for the 5 cm diameter circular applicator which is the smallest applicator for an MD2 accelerator. The standard photon-jaw setting corresponds to a field of 13×13 cm^2 at SSD $= 100$ cm, and hence the photon-jaws are far outside the geometric edge of the 5 cm diameter field. The upper photon-jaws sit at a distance of about 20 cm from the vacuum exit window. Thus a small displacement of the photon-jaws is enlarged by about 5 times as it is projected to SSD $= 100$ cm. In Fig. 3.7, if each of the upper photon-jaws moves 1 mm towards the beam axis (1 cm smaller width of the projected field at SSD $= 100$ cm), the applicator factor is smaller by about 4%. This dramatic dependence of ROFs on the photon-jaw setting is well known and discussed in other papers[5,92].

The blocking and outscattering effects on beam outputs versus SSD are discussed more in Chapter 4.
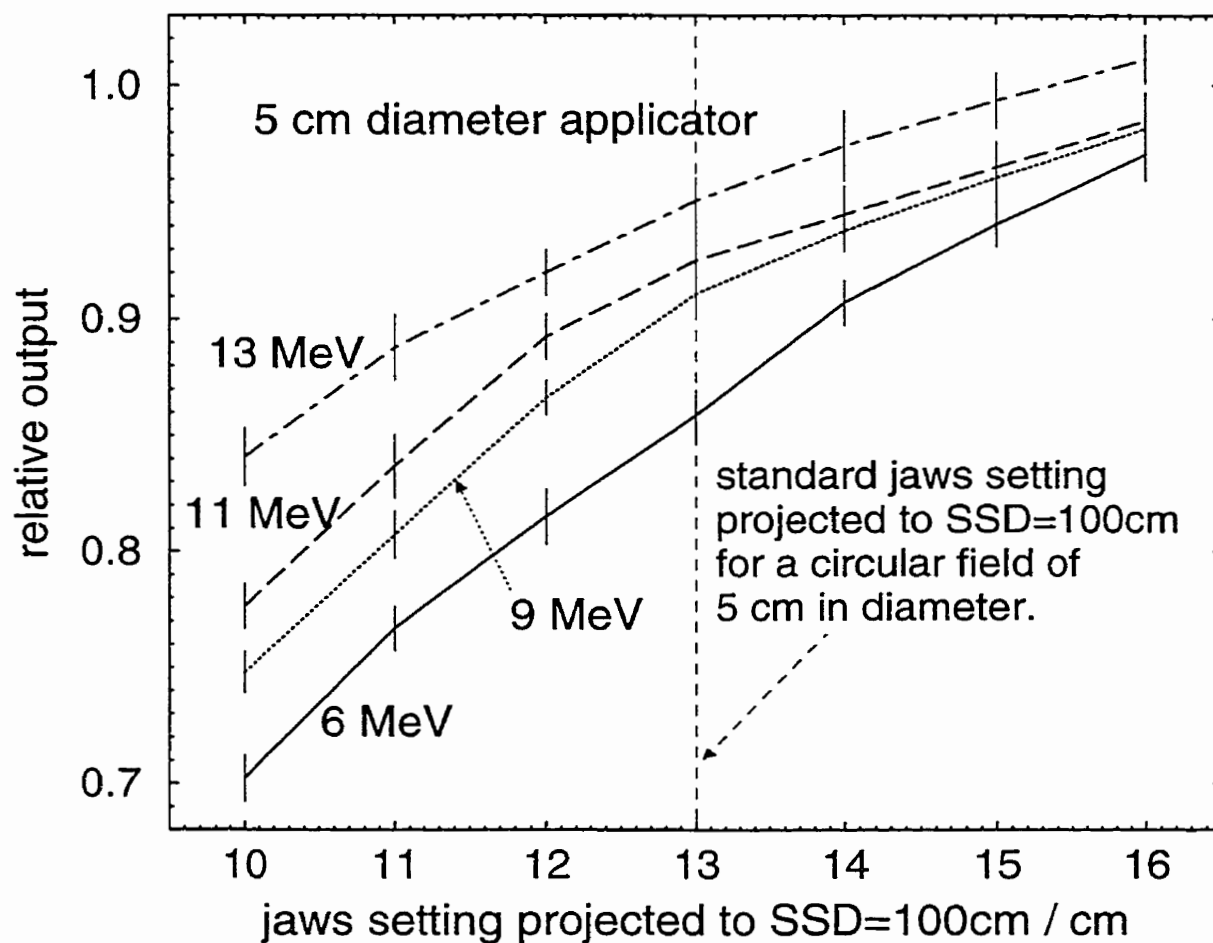
Figure 3.7: ROF of a 5 cm diameter circular applicator versus the position of the photon-jaw which are "outside" the beam. For this applicator, the standard photon-jaws setting is 13×13 cm^2 projected to SSD $= 100$ cm. By moving the first photon-jaws 1 mm towards the beam axis, the projected field is 12×12 cm^2 at SSD $= 100$ cm. All ROFs are normalized to the output of the open applicator of 10×10 cm^2.

Chapter 4

Applicator Gap Factors

4.1 Purpose of the gap factor study

This chapter discusses the calculation, using *BEAM*, of the variation in electron beam output with nominal source to surface distance (SSD) or air gap size, *i.e.*, gap factors (GFs). The study shows that this method is both accurate and practical for calculating these factors, and the Monte Carlo calculation of gap factors can replace the measurements if the accelerator is modeled properly. A unique advantage of the calculations is that a detailed knowledge can be obtained about components of the dose, such as the dose deposited in phantom by the particles scattered off the applicator, the photon-jaws, *etc.*, and thus a better understanding of the variation in gap factors can be developed.

The gap factor, GF, is defined as in Eq. 1.4 (page 6). Note that for extended SSDs, the field size on the surface of the phantom will be larger than A' by $(SSD/SSD_0)^2$. Usually, $SSD_0 = 100$ cm which is the reference SSD.

If the nominal SSD is used, the output for an extended treatment distance does not usually follow the inverse-square law, even for those large beams which are broad in the sense that side-scatter equilibrium for the dose at d_{max} is well established. Monte Carlo simulation is the best way to understand why. With *BEAM*, one needs the same accelerator simulation with standard SSD for each energy and then shorter additional calculations for each air gap of interest. The simulation data can also be used to find the effective SSD by following the clinical methods mentioned in Chapter 1. Ma *et al.*[93] presented Monte Carlo based techniques for extracting various effective and virtual SSDs. They used electron fluence to determine the effective SSD of a beam. In this chapter, the calculation of effective SSD based on Monte Carlo calculated dose versus air-gap size is discussed.

4.2 Results

4.2.1 Applicator gap factors

GFs are calculated for 10×10 cm^2 and 15×15 cm^2 square applicators and a circular applicator with 5 cm of diameter and the calculations are compared with the measurement. Fig. 4.1 shows part of the comparison. The additional air gap thickness is up to 20 cm which corresponds to a nominal SSD of 120 cm (air gap size g is between 0 and 20 cm inclusive). The calculations agree with the measurement within the statistical uncertainties of about 1% for all cases except one, which agrees to better than 2%. It can be concluded that the calculations are reproducing the gap factors accurately.

4.2.2 Effective SSDs

For a given beam energy and open applicator size, with the spatial resolution along the depth direction in our calculation, d_{max} changes little for g between 0 and 20 cm. Thus we can write the inverse-square law as:

$$GF(A', SSD_0 + g) = \frac{(SSD_{\mathrm{eff}} + d'_{\mathrm{max}})^2}{(SSD_{\mathrm{eff}} + d'_{\mathrm{max}} + g)^2} , \qquad (4.1)$$

where SSD_{eff} is the distance between the effective point source, for which the inverse-square law is best fit, and the phantom surface at reference SSD_0, g is the air gap between the plane normal to the beam axis at SSD_0 and the phantom surface. Here $SSD_0 = 100$ cm.

From Eq. 4.1, we get:

$$GF^{-1/2}(A', SSD_0 + g) = \frac{g}{SSD_{\mathrm{eff}} + d'_{\mathrm{max}}} + 1 . \qquad (4.2)$$

A plot of $GF^{-1/2}(A', SSD_0 + g)$ versus g is a straight line with a slope of $1/(SSD_{\mathrm{eff}} +$
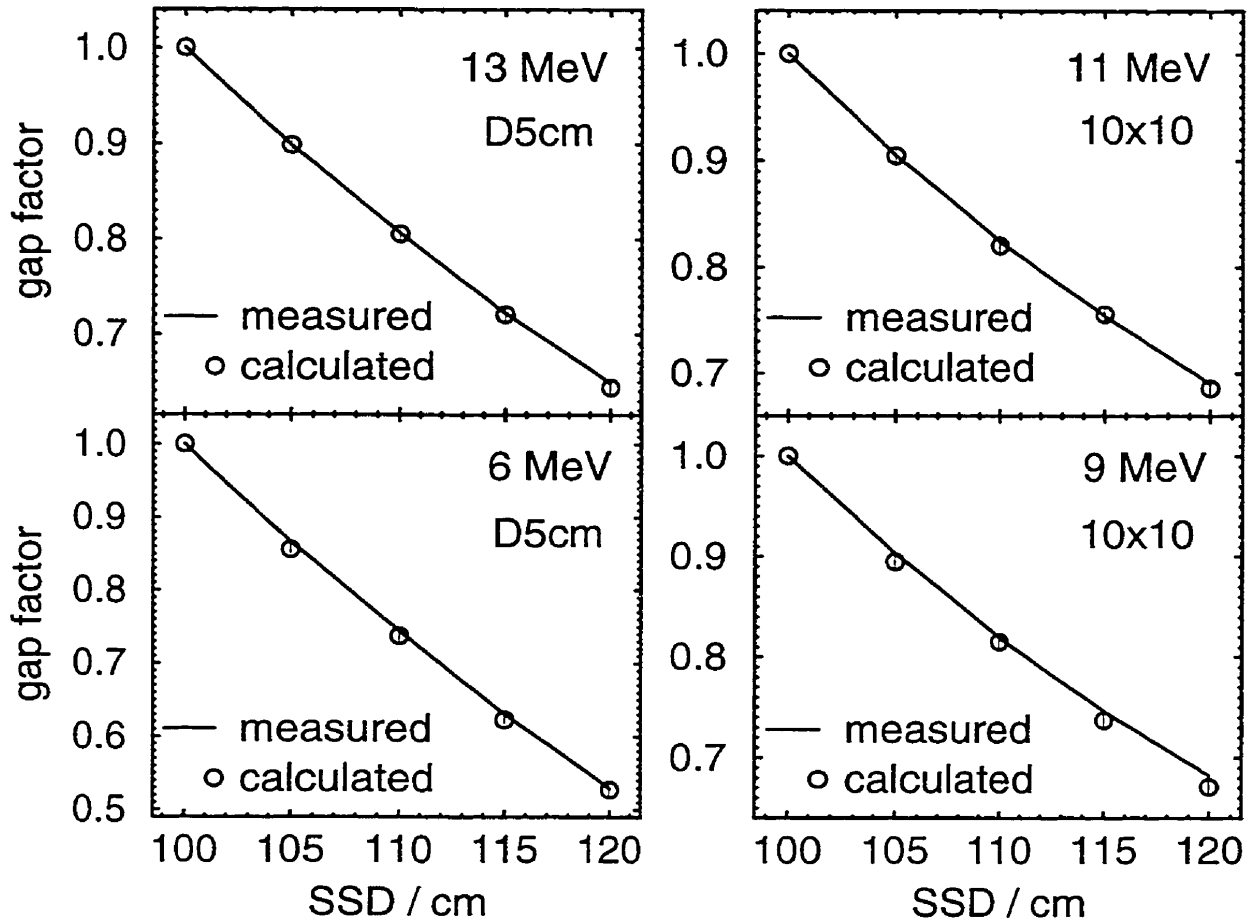
Figure 4.1: Measured and calculated gap factors for the 10×10 cm^2 applicator at 9 and 11 MeV and the circular applicator of 5 cm diameter for 6 and 13 MeV for an MD2 accelerator. The agreement between calculations and measurements is better than 2% in all cases and 1% in most cases. Similar agreement is found for all cases studied. The experimental data were measured at the Ottawa Regional Cancer Centre by Dr. Joanna Cygler.

$d'_{\max}$) and hence:[5],

$$SSD_{\text{eff}} = 1/slope - d'_{\max} .$$ (4.3)

Clinically, gap factors are needed only for open applicators. To get the relative output factor $ROF(A, SSD)$ for a field defined by a cutout A with reference to the reference open field A_0, usually 10×10 cm^2, at the reference SSD_0, usually 100 cm, the following equation is used:

$$ROF(A, SSD) = \frac{\frac{D}{U}(A, SSD, d_{\max})}{\frac{D}{U}(A_0, SSD_0, d_{\max 0})}$$

$$= \frac{\frac{D}{U}(A', SSD_0, d'_{\max})}{\frac{D}{U}(A_0, SSD_0, d_{\max 0})} \cdot \frac{\frac{D}{U}(A', SSD, d'_{\max})}{\frac{D}{U}(A', SSD_0, d'_{\max})} \cdot \frac{\frac{D}{U}(A, SSD, d_{\max})}{\frac{D}{U}(A', SSD, d'_{\max})}$$

$$= ROF_{\text{app}}(A', SSD_0) \cdot GF(A', SSD) \cdot ROF_{\text{cutout}}(A, SSD) ,$$ (4.4)

where $ROF_{\text{app}}(A', SSD_0)$ is the relative output factor for the open applicator A', also known as the applicator factor; $ROF_{\text{cutout}}(A, SSD_0)$ is the factor for the cutout, also called cutout factor. This implies that we need apply the idea of SSD$_{\text{eff}}$ only to open applicator fields for which $d_{\max}$ usually does not change with SSD[5,17,65]. In fact, the value of $d_{\max}$ can change significantly for small field sizes, for example, for a cutout of 2×2 cm^2, $d_{\max}$ for a 13 MeV beam changes from 1.4 cm at SSD = 100 cm to 0.8 cm at SSD = 115 cm. Hence the concept of effective SSD can only be applied to the open applicator case in general and hence if one is using effective SSDs for the gap factors, the order of the factors in Eq. 4.4 is mandatory, *i.e.*, one may not use $GF(A, SSD) \cdot ROF_{\text{cut}}(A, SSD_0)$.

Fig. 4.2 presents calculated values of $GF^{-1/2}$ and from the slopes of the fitted lines one determines the values of SSD$_{\text{eff}}$ in Table 4.1. The prediction of outputs using calculated values of SSD$_{\text{eff}}$ agree with measurements within 1%.

Most of the beams do not follow the inverse-square law using nominal SSDs. For small field beams, such as the ones of 5 cm in diameter, the values of SSD$_{\text{eff}}$ are less
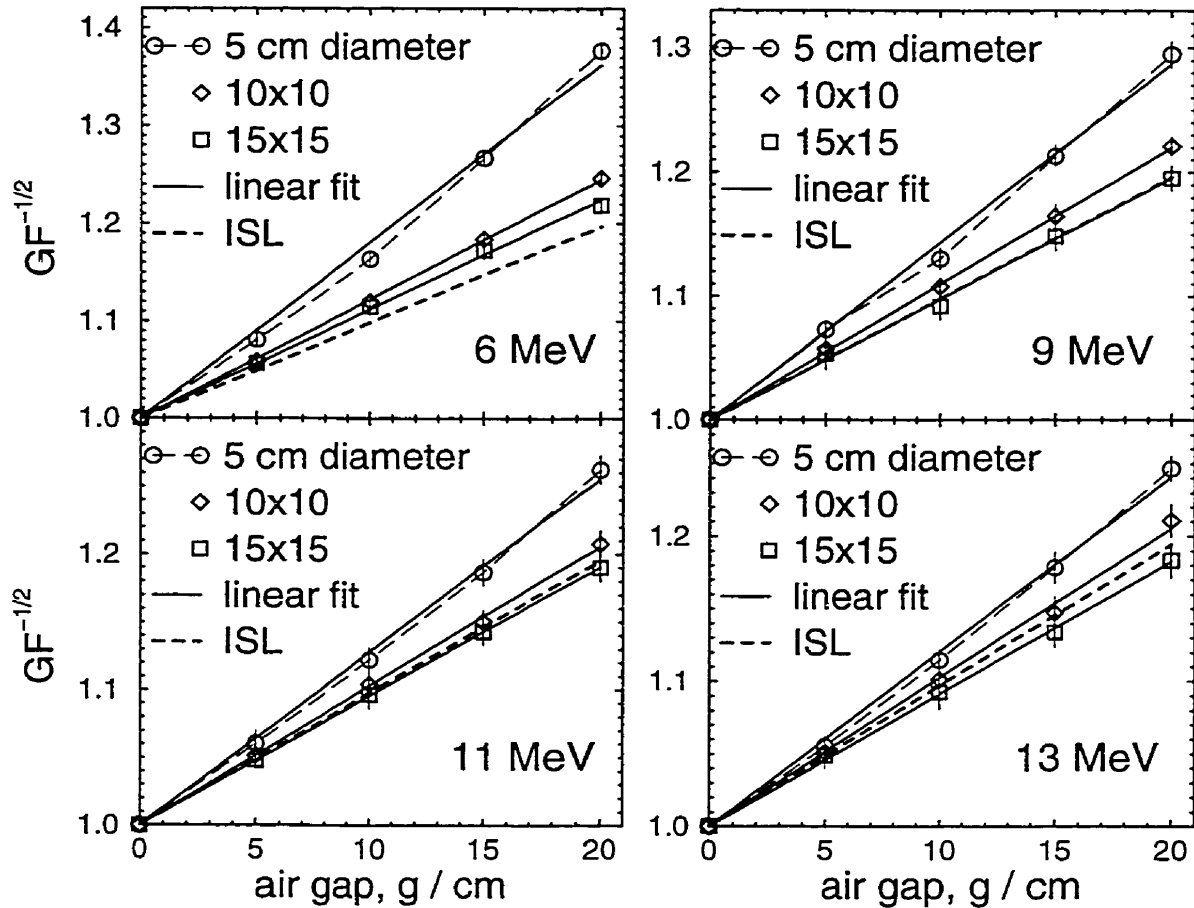
Figure 4.2: Calculated $GF^{-1/2}$ versus air gap g for the circular applicator with a diameter of 5 cm and the square applicators of 10×10 cm^2 and 15×15 cm^2. $g = 0$ corresponds to SSD $= 100$ cm. d_{max} varies with beam energy and applicator size but not with SSD. Values of SSD$_{eff}$ from Eq. 4.3 are shown in Table 4.1. The heavy-dashed lines represent the inverse-square law (ISL) using nominal SSDs and correspond to the reference SSD of 100 cm. The lines above the ISL lines correspond to smaller values of SSD$_{eff}$ and those below the ISL lines correspond to larger values of SSD$_{eff}$.

This means that the output would increase relative to the expected $1/r^2$ decrease, which means that the value of SSD_{eff} for these beams should not be smaller than the nominal reference SSD. Calculations with vacuum replacing air throughout the model confirm this $1/r^2$ decrease for narrow beams, however, in air, not only the in-phantom effect, but also the blocking and outscattering effects (see Chaper 3), which are discussed below, must be considered. These effects dominate and explain the observation that values of SSD_{eff} are smaller than the nominal reference SSD for small beams.

Blocking and outscattering effects versus SSD

The lack of side-scatter equilibrium at d_{max} reduces the output of a beam[5, 19]. With SSD varying, it makes the value of SSD_{eff} smaller than the nominal SSD for small beam sizes[94]. The lack of side-scatter equilibrium at d_{max} for small beams is caused by what we call blocking and outscattering effects (Section 3.2.3, page 48). With an air gap, the electrons represented by the dashed lines in Fig. 3.6 (page 51) could be scattered back into the field by the air if there were no collimation, but they are stopped by the collimation. Predictions with the inverse-square law include the contribution from these stopped electrons. This means a lower dose contribution from the direct component to the dose at d_{max} in the phantom with larger SSD, compared to that predicted by the inverse-square law using nominal SSDs. Since the direct component dominates the total dose (usually more than 90% of the dose is from the direct component), the total dose with an extra air gap is thus lower than the prediction of the inverse-square law using nominal SSDs. This is the major reason for the smaller SSD_{eff}.

The outscattering of the beam in the air gap makes the fluence of the beam decrease with air gap size faster than the inverse-square law prediction, and thus makes the dose at d_{max} decrease faster too, which corresponds to a smaller SSD_{eff}.

The outscattering effect is actually a consequence of the blocking effect. If there is no blocking effect, the decrease of the fluence of a beam due to outscattering is compensated by the in-coming particles from outside of the beam, and thus there is no net effect. These two effects together mean that there is lack of side-scatter equilibrium at d_{max} for a beam with a small field, or even with a large field but with a large air gap. For beams with small fields, they make the lack of side-scatter equilibrium at d_{max} for the direct component more significant with large air gaps.

Both the blocking and outscattering effects vary with the air-gap size.

To analyze quantitatively the blocking and outscattering effects on output, we compare simulations of the beams in air with those in vacuum. Fig. 4.3 shows schematically how this analysis is done. The results of simulations of an MD2 machine in vacuum (Cases Vacuum(100) and Vacuum(115) in Fig. 4.3) show that for all beams, both large and small, the outputs of the direct component at different SSDs follow the inverse-square law using nominal SSDs within 1%. In air, this is usually not true. For example, for the 6 MeV beam with field size at an SSD of 100 cm of 5 cm diameter, with an air gap g of 15 cm, *i.e.*, SSD = 115 cm (Case Air(115) in Fig. 4.3), the total output of the beam is 18% lower than the prediction of the inverse-square law using nominal SSDs. The prediction of the inverse-square law is based on the output of the beam at a nominal SSD = 100 cm in air (Case Air(100) in Fig. 4.3). This comparison between the simulation in air and the inverse-square law prediction shows that the blocking and outscattering effects together make the output 18% lower.

Comparing the output of Case Vacuum_gap(115) in Fig. 4.3 to the prediction of the inverse-square law based on Case Air(100), we know that the blocking effect alone makes the output of the 6 MeV beam 16% lower. Similarly, by comparing Case Vacuum_gap(115) and Air(115), we find that the outscattering effect alone makes the output of the 6 MeV beam to be 2.5% lower. To see the absolute blocking effect versus SSD (including the 5 cm air gap which is right after the last scraper for the
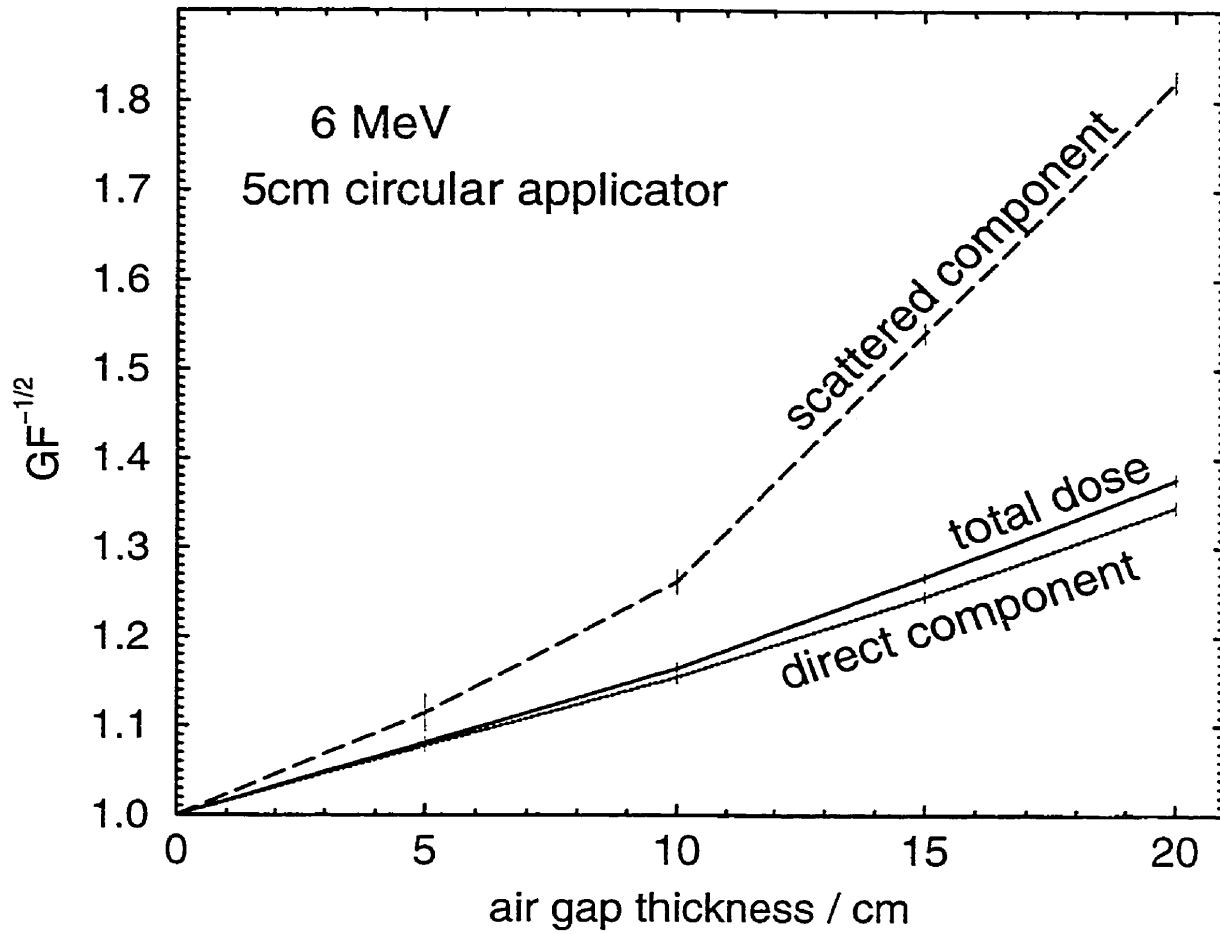
Figure 4.4: Calculated $GF^{-1/2}$ versus air-gap size g for component doses for a 6 MeV beam with a 5 cm circular applicator. The slopes of the curves go up with g, which means the values of SSD_{eff} are smaller with larger air gap, *i.e.*, the output drops off more quickly.

blocking effect), we compare the ratios of outputs of Cases No_outscattering(100) to Vacuum(100) and No_outscattering(115) to Vacuum(115). The ratio is 75.5% for SSD = 100 cm and 66.5% for 115 cm. This is consistent with the expectation, the larger the gap, the larger the blocking effect.

Fig. 4.4 explains why for small fields the data show a systematic curvature about the fit straight line (Fig 4.2). As discussed above, the value of SSD_{eff} for these small beams is much smaller than the nominal SSD because of the blocking and outscattering effects. But the curves of $GF^{-1/2}$ versus g both for the direct and scattered components are not straight lines. This is more pronounced for the scattered component. Since the opening edge is close to the central axis for small fields, most of the scattered particles can contribute to the central axis dose for small air gaps but go away from the central axis if the air gap is large, and hence contribute less to the dose at d_{max} along the central axis relative to $1/r^2$ decrease. This causes the points to go above the straight lines. For the direct component, the slight distortion for large air gap is due to larger blocking and outscattering effects for larger air gap.

If the field size is defined by collimation at the phantom surface, the inverse-square law should hold even with a large SSD, no matter whether it is a large beam or a small beam since there is neither a blocking nor an outscattering effect. Clinically, field size usually is not defined at the phantom surface especially for extended SSDs. The blocking and outscattering effects then must be considered and the output cannot be calculated just using the inverse-square law.

4.2.4   Large field beams

For the 15 × 15 cm^2 field beams, except for the 6 MeV beam, the values of SSD_{eff} are slightly larger than the nominal reference SSD, which means the output of a large field beam at increased SSD is larger than predicted by the inverse-square law using nominal SSDs. This would not happen unless there are extra particles which con-

tribute to the central-axis dose at $d_{\max}$ at larger SSD. These extra particles are not from the direct component. The only possibility is that they come from the particles scattered off the collimators.

In Fig. 4.5, the ratios of gap factors for the direct and scattered components and the total dose to the prediction of the inverse-square law are shown versus nominal beam energy for a nominal SSD = 115 cm with an open 15×15 cm^2 applicator. The solid line at unity represents the output of a beam which follows the inverse-square law. A value below the line means the output drops off faster than the inverse-square law. Except for the 6 MeV beam, the ratios of the GF to the inverse-square law using nominal SSDs for the direct component are very close to unity, which means that the values of SSD$_{\text{eff}}$ for the direct component are very close to the nominal SSD. That is because the side-scatter equilibrium at $d_{\max}$ is well established for the direct electrons in the beams and thus the dose component from direct electrons approximately follows the inverse square law using the nominal SSD. The calculations show that the output from the scattered component at larger SSDs is often larger than the prediction by the inverse square law, which means that the ratio of the scattered dose component to the total dose increases with SSD. For example, the scattered dose component for the 13 MeV beam with an open 15×15 cm^2 applicator at nominal SSD = 100 cm is 6.6% of the total dose at $d_{\max}$ along the central axis in the phantom while it increases to 9.4% at SSD = 115 cm. Almost all of the difference comes from electrons scattered off the last 2 scrapers. Fig. 4.6 explains how this happens. Since the field is large, the edge of the collimator is far from the central axis, thus the angle is large if a scattered electron is to influence the maximum dose along the central axis, $D_{\max}$, for an SSD of 100 cm. For this reason, many of the scattered electrons do not influence $D_{\max}$. With a thick air gap, the angle to influence $D_{\max}$ decreases. More scattered electrons thus contribute to $D_{\max}$. This effect is more significant for high-energy beams as seen in Fig. 4.5.

For the 6 MeV beam, the output with increased air gap is lower than the prediction
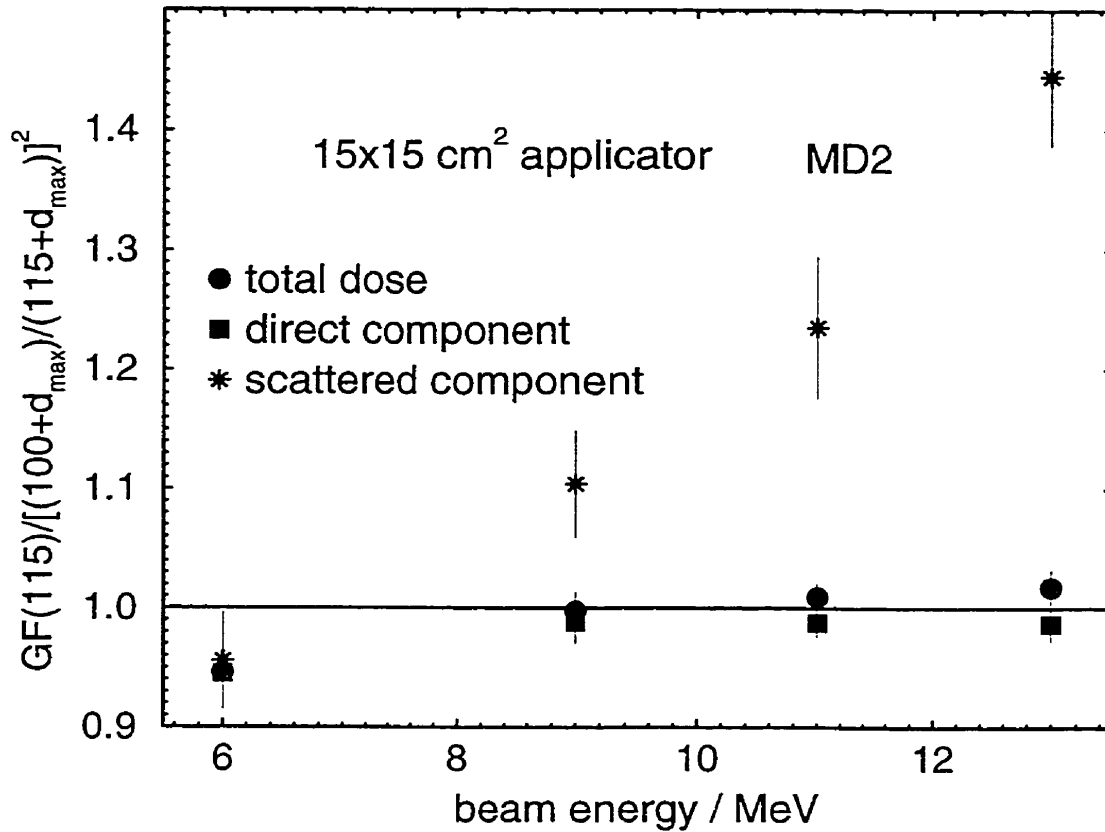
Figure 4.5: Gap factors at SSD =115 cm normalized to the inverse square law prediction using nominal SSDs for different dose components — the direct, scattered and total — are shown versus beam energy. Unity represents the nominal reference SSD. A value below unity means the output of a beam drops off faster than the inverse-square law, $i.e.$, SSD_{eff} is smaller than the nominal reference SSD.

by the inverse-square law using nominal SSDs because the blocking and outscattering effects are still there for such a low-energy beam. For this case the blocking effect is at many layers of the collimator system — the applicator, the photon-jaws and the container of the secondary scattering foil, each has a blocking effect which causes about 1% loss of output of the beam as the SSD increases from 100 to 115 cm.

For the 10×10 cm^2 beams, the values of SSD$_{\text{eff}}$ are slightly smaller than the nominal reference SSD because of the blocking and outscattering effects too. Since this field is larger than the 5 cm diameter field, we can see that the effects are less important for this field than the latter one.

As described in Section 2.2.4 (page 27), the component module *BLOCK* is used to simulate the rounded corners of the applicator and better results are obtained than that using *APPLICAT* which can only simulate right-angle openings. The reason is similar to that discussed previously about the scatter-angle needed to make contribution to D_{max} for the scattered component (Fig. 4.6). For rounded corners this effect is bigger.

4.3 Summary and conclusions

It has been shown that for open applicators for an SSD range between 100 and 120 cm, Monte Carlo calculations for gap factors agree with measurements within 1% for most cases and 2% for all. Based on the calculated gap factors, the values of SSD$_{\text{eff}}$ are calculated. The prediction of outputs using the calculated values of SSD$_{\text{eff}}$ agree with measurements within 1%. The Monte Carlo method has been used to analyze the dose components for a better understanding of the beams and the related physics. The Monte Carlo results are used to explain why the gap factors do not follow the inverse-square law using nominal SSDs. For small fields, the blocking and outscattering effects on the direct component causes the lack of side-scatter equilibrium at d_{max} to be more
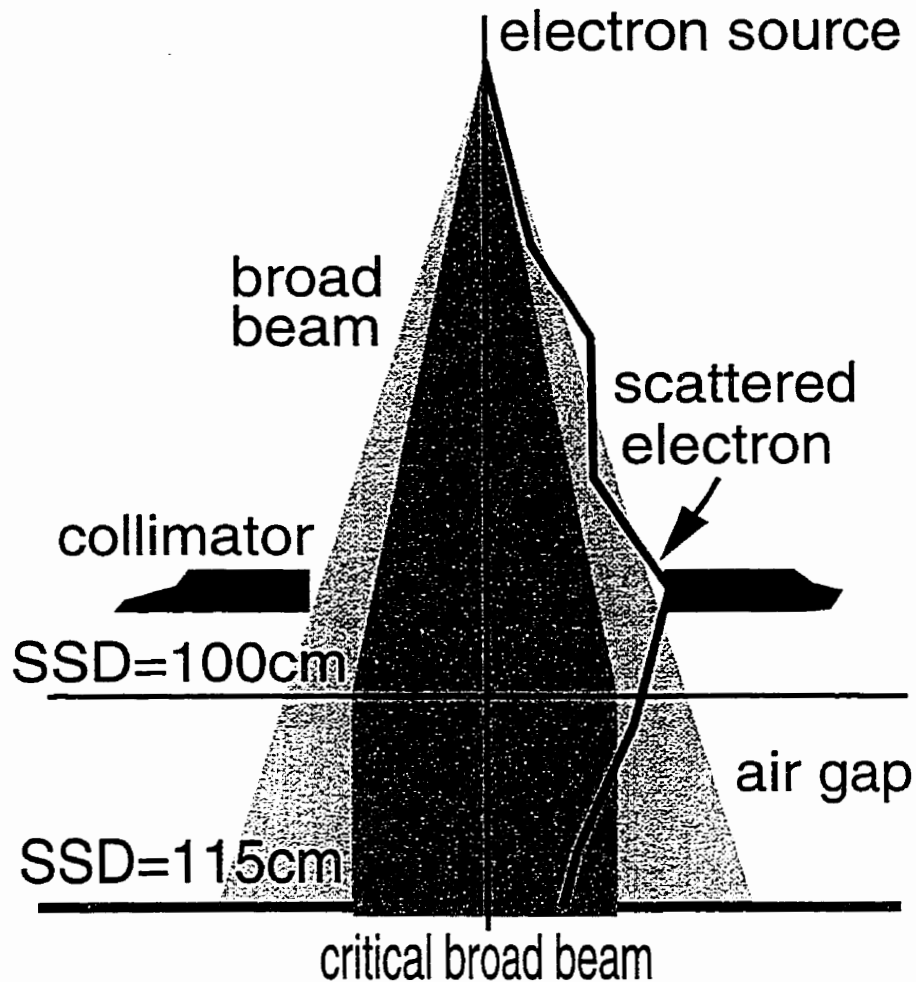
Figure 4.6: For a large field beam, side-scatter equilibrium at d_{max} for the direct component is well established (darker shadow indicates the critical field size to establish side-scatter equilibrium at d_{max}), thus the SSD_{eff} for the direct component is very close to the nominal SSD. Due to the large scatter angle needed, many of the electrons scattered off the collimator cannot contribute to D_{max} if the air gap is thin. With a large air gap, the angle needed is smaller and thus more electrons from the collimator contribute relatively more to the output of the beam. The value of SSD_{eff} is thus greater than the nominal SSD.

significant with larger SSDs, and this results in the values of SSD_{eff} being smaller than the nominal reference SSDs. For large fields, the relatively larger scattered component contributing to D_{max} with larger SSD makes the values of SSD_{eff} larger than the nominal reference SSD.

Chapter 5

Stopping-Power Ratio Corrections for Small Fields

5.1 The purpose of the stopping-power ratio study

The output of electron beam accelerators is strongly dependent on the size of the field. Thus the measurement of outputs for different beam sizes is an important component of electron beam dosimetry in clinical practice. This is usually done as measurement of the output for a given field size relative to that of a reference field size, *i.e.*, a relative output factor or ROF. Although people use different detectors for this kind of measurement, such as film[95, 96] and silicon diode[64], in most clinics ion chambers are used. To convert ionization to absorbed dose to water, a fundamental equation of ion chamber dosimetry[97] is:

$$D = M N_{\text{gas}} (\bar{L}/\rho)_{\text{air}}^{\text{water}} P_{\text{ion}} P_{\text{repl}} P_{\text{wall}} \ , \tag{5.1}$$

where M is the electrometer reading corrected for polarity effects and for temperature and air pressure, in nC, N_{gas} is the cavity-gas calibration factor which is a constant in Gy/nC, and P_{ion}, P_{repl}, P_{wall} are ion recombination, replacement (water is replaced by air) and chamber wall correction factors, respectively, which may vary with beam conditions. P_{wall} is taken as unity for electron beams[97] and hence is constant. When P_{ion} is close to unity, its value does not change significantly with dose rate[98] (and hence field size and depth in a phantom) although the size of the correction is proportional to the dose rate, however, if it is not close to unity, which might happen with a high-dose rate pulsed-swept beam, halving the dose rate would reduce it significantly towards unity. If this is the case, ignoring P_{ion} variation could introduce a couple of percent overestimate of ROFs.

The water to air restricted mean mass collision stopping-power ratio, $(\bar{L}/\rho)_{\text{air}}^{\text{water}}$, is a function of depth in water[95, 97, 99]. As discussed below, our calculations show that it is also a function of field size. For electron beam relative output measurements, which are usually done at d_{max} for each beam, P_{repl} is thought to be unity if a well-guarded plane-parallel chamber is used[97, 100, 101]. For cylindrical or poorly-guarded plane-parallel chambers, P_{repl} is also a function of depth in phantom.
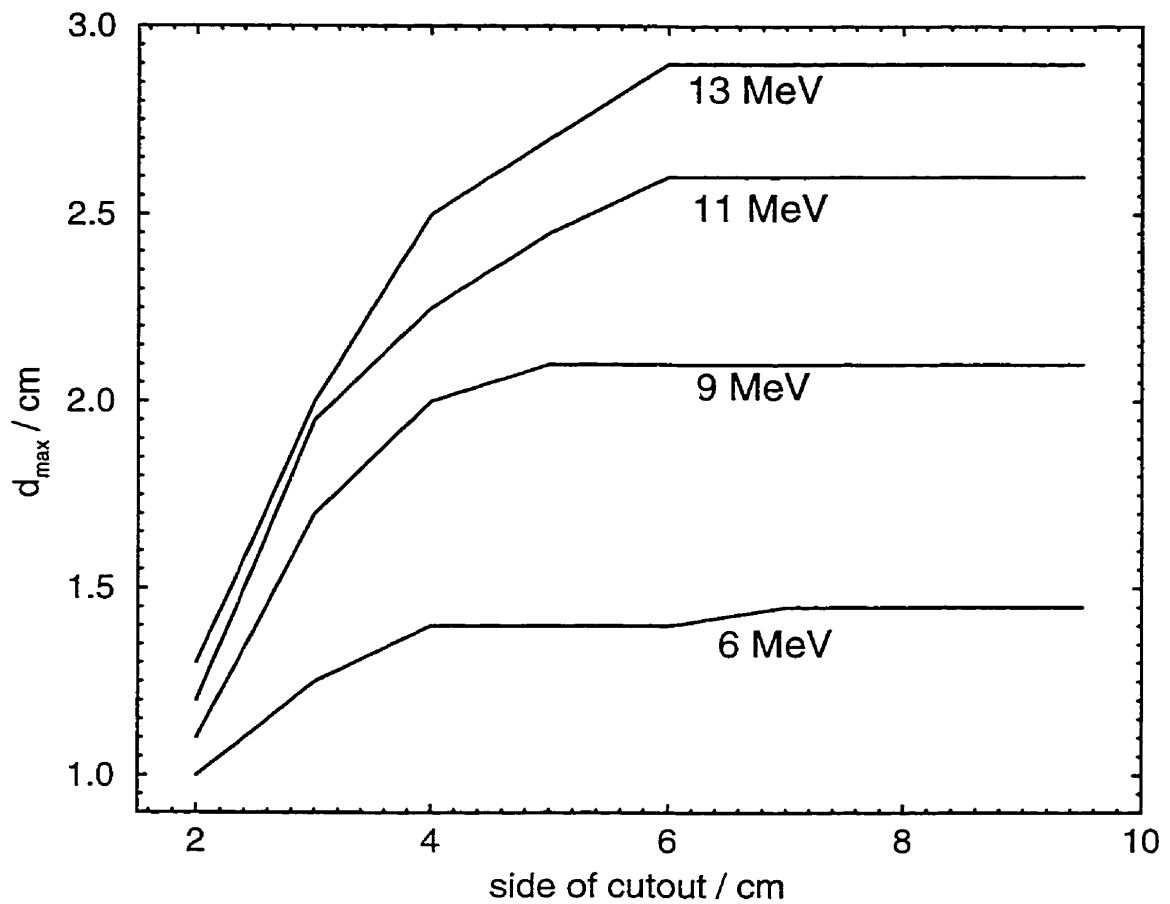
Figure 5.1: Measured values of $d_{\max}$ versus cutout size for MD2 accelerator, from Cygler *et al.*[102]. Values of $d_{\max}$ change significantly for small fields, especially for high-energy beams.

Given the above variations in these parameters, the ROF of beams with different field sizes defined by cutouts within a given applicator are deduced from measurements as:

$$ROF_{cut}(A) = \frac{\frac{D}{U}(A, d_{max})}{\frac{D}{U}(A', d'_{max})} = \frac{\frac{M}{U}(A, d_{max}) \cdot (\bar{L}/\rho)_{air}^{water}|_{A,d_{max}} \cdot P_{repl}|_{d_{max}}}{\frac{M}{U}(A', d'_{max}) \cdot (\bar{L}/\rho)_{air}^{water}|_{A',d'_{max}} \cdot P_{repl}|_{d'_{max}}} , \qquad (5.2)$$

where $\frac{D}{U}$, $\frac{M}{U}$ are dose and ionization reading per monitor unit, respectively; A is the field size defined by a cutout; and A' is the reference field size defined by an open applicator, and any variation in P_{ion} and polarity effects has been ignored. It is well known that for small field sizes, the depth of dose maximum, d_{max}, moves towards the surface with decreasing field size (Fig. 2.9, page 33 and Fig. 5.1). If one follows the recommendation of the AAPM's report on clinical electron beam dosimetry (TG-25, Khan *et al.*)[5], then in Eq. 5.2 one would take into account the variation of the stopping-power ratio and P_{repl} with depth as d_{max} changes.

For large fields, there is no d_{max} shift among depth-dose curves with field size, *i.e.*, $d_{max} = d'_{max}$. The values of $(\bar{L}/\rho)_{air}^{water}$ and P_{repl} in Eq. 5.2 cancel out because they are not a function of field size in large beams. Thus the ROF for large beams can be calculated as the ratio of the two ionization readings per monitor unit, *i.e.*,

$$ROF_{cut}(A) = \frac{\frac{M}{U}(A, d_{max})}{\frac{M}{U}(A', d'_{max})} . \qquad (5.3)$$

For small fields where d_{max} values are closer to the surface than d_{max} for a broad beam, the values of $(\bar{L}/\rho)_{air}^{water}$ at the corresponding d_{max} values are no longer the same. The value of P_{repl} may change with depth as well, but the variation in P_{repl} is small compared to that of $(\bar{L}/\rho)_{air}^{water}$. Nonetheless, it should be corrected for if a cylindrical or poorly-guarded plane-parallel chamber is used.

Based on the values of P_{repl} versus mean energy at depth given in TG-21[97], the effect of P_{repl} variation due to the d_{max} shift is up to about one-half percent change in ROFs for MD2 machines for an RK 83-05 chamber with an inner diameter of 4 mm. This effect is in the opposite direction of that due to the $(\bar{L}/\rho)_{air}^{water}$ change with

depth. For a Farmer chamber with a 6.4 mm inner diameter the effect would be up to 1%. All measured values of P_{repl} are for broad beams[97,103]. Values for small beams are not known, thus in practice we assume that they are the same as for broad beams.

If TG-25[5] is carefully followed in clinical practice, this $(\bar{L}/\rho)_{air}^{water}$ variation due to d_{max} shift is taken into account and Eq. 5.3 should not be used in ROF measurement for small fields.

Since TG-21 or TG-25 only give $(\bar{L}/\rho)_{air}^{water}|_{\infty,d_{max}}$ for broad beams, the stopping-power ratio for the smaller field sizes, *i.e.*, $(\bar{L}/\rho)_{air}^{water}|_{A,d_{max}}$, is not available, and hence Eq. 5.2 can not be applied in clinical practice. Instead, the ratio of $(\bar{L}/\rho)_{air}^{water}|_{\infty,d_{max}}$ to $(\bar{L}/\rho)_{air}^{water}|_{\infty,d'_{max}}$ is used in Eq. 5.2 if TG-25 is carefully followed in clinical practice. This chapter will investigate how this approximation in TG-25 affects ROF measurements. Furthermore, the $(\bar{L}/\rho)_{air}^{water}$ data in TG-21 or TG-25 are for mono-energetic beams. In the real world, the beams from clinical accelerators are neither mono-energetic nor parallel. Values of $(\bar{L}/\rho)_{air}^{water}$ for the realistic beams from clinical accelerators differ by up to 1.4% from values for mono-energetic beams at d_{max} for broad beams[81]. In this chapter $(\bar{L}/\rho)_{air}^{water}$ data for realistic beams from Monte Carlo simulation are used and the results are compared with those using TG-21 or TG-25 data.

For good clinical practice, one also needs to pay attention to other effects, such as the stem effect or polarity effect[60]. These effects are not discussed in this chapter.

5.2   Results

5.2.1   Variations of stopping-power ratios

Fig. 5.2 shows calculated stopping-power ratios versus depth for both mono-energetic and realistic beams (see Appendix B for further calculated values). Fig. 5.2(d) com-
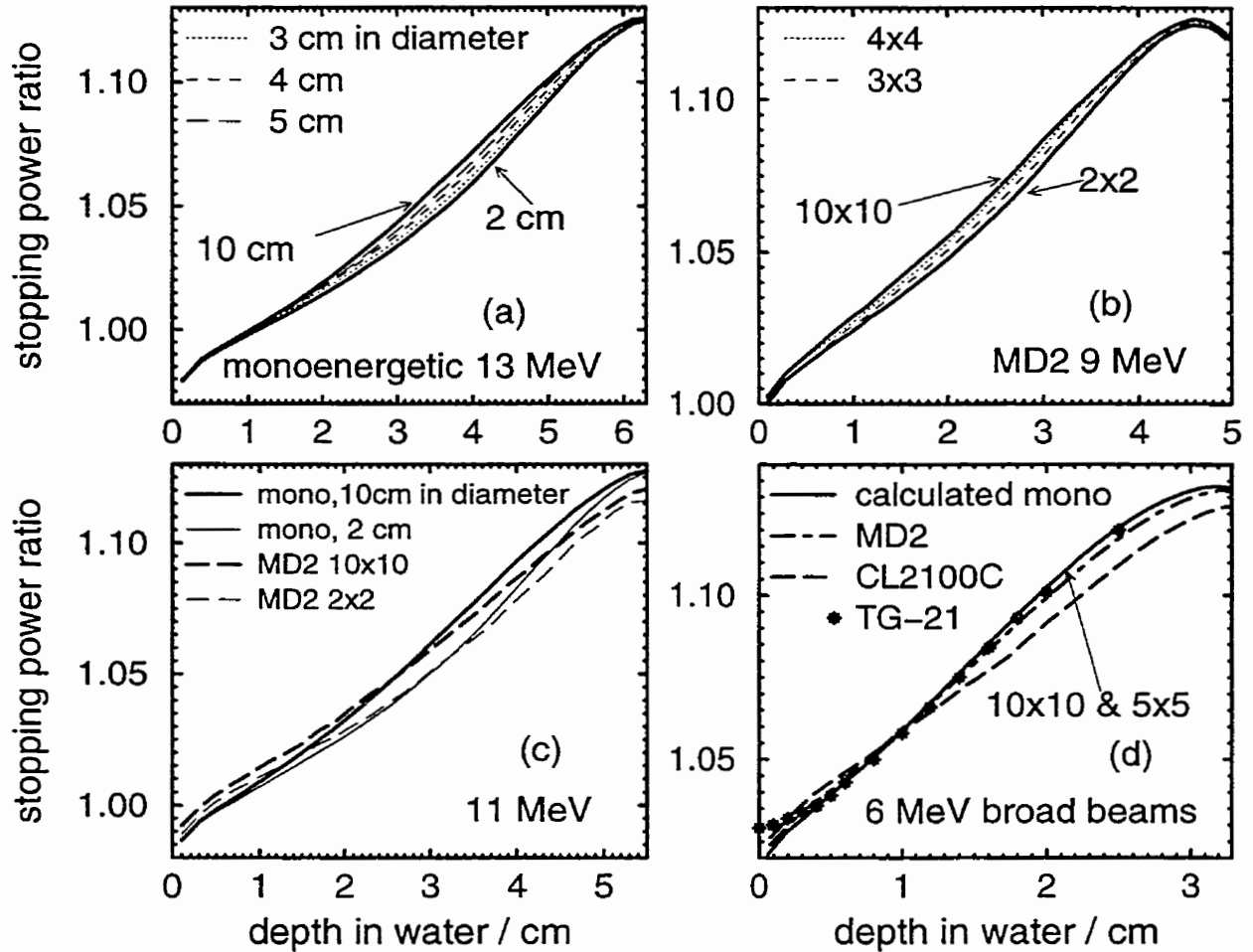
Figure 5.2: $(\bar{L}/\rho)_{\text{air}}^{\text{water}}$ versus depth curves (a) for 13 MeV mono-energetic parallel beams of various field sizes incident on a water phantom; (b) for 9 MeV realistic MD2 beams for various cutout sizes; (c) for 11 MeV mono-energetic and realistic MD2 broad and narrow beams; (d) for different broad beams of 6 MeV electrons.

pares values of $(\bar{L}/\rho)_{\text{air}}^{\text{water}}$ versus depth for broad mono-energetic beams of 6 MeV electrons as calculated here against those given in TG-21 or TG-25. The agreement is excellent except near the surface where Malamut *et al.* pointed out that the calculations in TG-21 have some approximations[85]. The calculated realistic $(\bar{L}/\rho)_{\text{air}}^{\text{water}}$ data for broad 6 MeV beams are also compared in this figure.

The calculations show that stopping-power ratio versus depth curves are a function of the beam field size. In Fig. 5.2(a), stopping-power ratios versus depth are presented for different field sizes for 13 MeV mono-energetic parallel beams. The values of stopping-power ratio at a given depth for small fields are lower than those for large fields. For example, at d_{max} in the 10×10 cm^2 beam (at 2.9 cm), the stopping-power ratio decreases by about 1% as the beam size decreases to a 2×2 cm^2 field. At d_{max} in the 2×2 cm^2 beam (at 1.3 cm), the difference of $(\bar{L}/\rho)_{\text{air}}^{\text{water}}$ values between 10×10 cm^2 and 2×2 cm^2 fields is only 0.2% since the curves are less spread out at this depth. Fig. 5.2(b) shows that stopping-power ratio curves for realistic beams also differ with field size, although in this case, slightly less than in the mono-energetic case. The reason for the decrease with field size is that the low-energy electrons are easily scattered away from the central axis and a corresponding number is not scattered in for small fields, thus the mean energy of the beam close to the central axis for a small field is larger than that of a large beam at a given depth, which corresponds to a smaller $(\bar{L}/\rho)_{\text{air}}^{\text{water}}$ value for a small field than that of a large field at that depth. At the phantom surface, the mean energy is about the same for different field sizes (for mono-energetic beams, it is exactly the same) and hence the $(\bar{L}/\rho)_{\text{air}}^{\text{water}}$ curves for different field sizes are the same at the phantom surface. Fig. 5.2(c) compares the curves for 11 MeV mono-energetic and realistic beams. The curves for mono-energetic beams always have larger slopes than those of realistic beams[81].

The following observations can be drawn from Fig. 5.2.

The maximum difference between stopping-power ratios for realistic beams and mono-energetic beams is more significant at higher energies for a given accelerator

(compare Fig. 5.2(c) with (d) for MD2 curves), though at d_{max}, it depends on the position of d_{max} relative to the cross over point of $(\bar{L}/\rho)^{\text{water}}_{\text{air}}$ versus depth for mono-energetic and realistic beams. The difference between the curves with different field sizes is also energy dependent. At 6 MeV, the stopping-power ratio curve for the beam defined by a 5 × 5 cm^2 cutout is identical to that of the broad beam (Fig. 5.2(d)) while for 13 MeV case there is an obvious difference (Fig. 5.2(a)). At d_{max} for small beams, the difference is larger for lower energies since for low-energy beams, curves of $(\bar{L}/\rho)^{\text{water}}_{\text{air}}$ versus depth are well spread out at d_{max} for small fields while for high energy beams they are not. The slope of a stopping-power ratio curve also varies with energy, the higher the energy, the smaller the slope.

5.2.2 Corrections to relative output factors

Since d_{max} moves upstream for small fields, $(\bar{L}/\rho)^{\text{water}}_{\text{air}}$ values decrease and thus ROFs for small fields are over-estimated using Eq. 5.3 instead of Eq. 5.2. To measure ROFs accurately, proper values of $(\bar{L}/\rho)^{\text{water}}_{\text{air}}$ for the corresponding depth and field size should be used. To correct Eq. 5.3 completely for the effects of changes in $(\bar{L}/\rho)^{\text{water}}_{\text{air}}$ one needs:

$$f_{\text{f.s.}} = \frac{(\bar{L}/\rho)^{\text{water}}_{\text{air}}|_{A,d_{\text{max}}}}{(\bar{L}/\rho)^{\text{water}}_{\text{air}}|_{A',d'_{\text{max}}}} \ . \tag{5.4}$$

This is the field-size (f.s.) dependent correction method in which values of $(\bar{L}/\rho)^{\text{water}}_{\text{air}}$ from curves for different field sizes are used.

The above correction is accurate but it requires knowing $(\bar{L}/\rho)^{\text{water}}_{\text{air}}$ as a function of field size for each accelerator beam. This makes the correction complicated. Clinically, it is not practical. A simple approach is to use just broad-beam data:

$$f_{\text{broad}} = \frac{(\bar{L}/\rho)^{\text{water}}_{\text{air}}|_{\infty,d_{\text{max}}}}{(\bar{L}/\rho)^{\text{water}}_{\text{air}}|_{\infty,d'_{\text{max}}}} \ . \tag{5.5}$$

The $(\bar{L}/\rho)^{\text{water}}_{\text{air}}$ data for mono-energetic broad beams are given in TG-21 or TG-25.

Table 5.1: Corrections needed for MD2 ROFs for small cutout sizes measured without accounting for changes in $(\bar{L}/\rho)^{\text{water}}_{\text{air}}$ with depth (Eq. 5.3). Values of $f^{\text{mono}}_{\text{broad}}$ and $f^{\text{realistic}}_{\text{broad}}$ correspond to the broad-beam method based on TG-21 (or TG-25) and realistic beam data respectively, $f^{\text{mono}}_{\text{f.s.}}$ and $f^{\text{realistic}}_{\text{f.s.}}$ to the field-size dependent method based on calculated mono-energetic data and realistic accelerator beam data respectively.

energy	13 MeV					9 MeV			
cutout / cm^2	2x2	3x3	4x4	5x5	10x10	2x2	3x3	4x4	10x10
d_{max}/ cm	1.3	2.0	2.5	2.7	2.9	1.1	1.7	2.0	2.1
$f^{\text{mono}}_{\text{broad}}$	0.965	0.979	0.990	0.995	–	0.968	0.987	0.997	–
$f^{\text{realistic}}_{\text{broad}}$	0.970	0.983	0.992	0.996	–	0.975	0.990	0.997	–
$f^{\text{mono}}_{\text{f.s.}}$	0.963	0.976	0.987	0.993	–	0.965	0.983	0.994	–
$f^{\text{realistic}}_{\text{f.s.}}$	0.967	0.979	0.989	0.994	–	0.972	0.986	0.996	–
energy	11 MeV					6 MeV			
cutout / cm^2	2x2	3x3	4x4	5x5	10x10	2x2	3x3	4x4	10x10
d_{max}/ cm	1.2	1.95	2.25	2.45	2.6	1.0	1.25	1.4	1.45
$f^{\text{mono}}_{\text{broad}}$	0.966	0.983	0.990	0.996	–	0.982	0.992	0.998	–
$f^{\text{realistic}}_{\text{broad}}$	0.971	0.985	0.992	0.997	–	0.983	0.992	0.998	–
$f^{\text{mono}}_{\text{f.s.}}$	0.963	0.979	0.987	0.994	–	0.977	0.989	0.997	–
$f^{\text{realistic}}_{\text{f.s.}}$	0.967	0.983	0.988	0.996	–	0.978	0.989	0.998	–

Values of $f_{\text{f.s.}}$ have been calculated for open applicators using $(\bar{L}/\rho)^{\text{water}}_{\text{air}}$ values for realistic MD2 beams. These corrections are within 1% of unity for the smallest applicator (5 cm diameter), even at the higher energies, and are not needed for other applicators because d_{max} does not shift significantly for open applicators and there is little field size dependence.

In contrast, it is well known that the d_{max} shifts are significant for small fields defined by cutouts[5]. Based on the d_{max} data measured by Cygler et al.[102], Table 5.1 presents corrections based on the different $(\bar{L}/\rho)^{\text{water}}_{\text{air}}$ data and methods. To specify $(\bar{L}/\rho)^{\text{water}}_{\text{air}}$ values based on TG-21 or TG-25, the mean incident energy is calculated based on Rogers and Bielajew's specification of electron beam energy[104] and linear interpolation is applied to the tabulated values. The $(\bar{L}/\rho)^{\text{water}}_{\text{air}}$ change due to the d_{max} shift is insensitive to the details of the energy which is selected for the TG-21 or TG-25 data. The factors $f^{\text{mono}}_{\text{broad}}$ and $f^{\text{realistic}}_{\text{broad}}$ are based on the broad-beam method, with $(\bar{L}/\rho)^{\text{water}}_{\text{air}}$ data from TG-21 or TG-25 and from realistic MD2 beams respectively. The factors $f^{\text{mono}}_{\text{f.s.}}$ and $f^{\text{realistic}}_{\text{f.s.}}$ are based on the field-size dependent method, with mono-energetic and realistic beam data respectively.

The factor $f^{\text{mono}}_{\text{broad}}$, which is the factor used if TG-25 is followed, is about 3% less than unity for 2×2 cm^2 fields for all energies except 6 MeV (Table 5.1). This means that if Eq. 5.3 is used in ROF measurements for small fields, the ROFs are overestimated by up to 3% based on the $(\bar{L}/\rho)^{\text{water}}_{\text{air}}$ data from TG-25, however, the factor $f^{\text{mono}}_{\text{broad}}$ does not take into account the effect of field size on stopping-power ratio and ignores the difference in $(\bar{L}/\rho)^{\text{water}}_{\text{air}}$ between realistic and mono-energetic beams.

To take into account the field-size effect on stopping-power ratio, the factor $f^{\text{mono}}_{\text{f.s.}}$ is calculated for different field sizes and energies. This factor still uses stopping-power ratio data for mono-energetic beams. The factor is a few tenths percent (up to 0.5%) smaller than the factor $f^{\text{mono}}_{\text{broad}}$ which means the correction is up to 0.5% larger. This is the size of the difference of $(\bar{L}/\rho)^{\text{water}}_{\text{air}}$ values between the field size of interest and

the reference field at $d_{\max}$ of the field of interest (which tends to be larger at lower energies).

The factor $f_{\text{broad}}^{\text{realistic}}$ is the same as $f_{\text{broad}}^{\text{mono}}$ but uses $(\bar{L}/\rho)_{\text{air}}^{\text{water}}$ values for incident realistic broad beams instead of the stopping-power ratio data from TG-21 or TG-25 for incident mono-energetic beams. Since the slope of a broad mono-energetic $(\bar{L}/\rho)_{\text{air}}^{\text{water}}$ data curve is always higher than that of a curve for a realistic beam with the same mean energy, values of $f_{\text{broad}}^{\text{mono}}$ in Table 5.1 are always smaller than $f_{\text{broad}}^{\text{realistic}}$ for small fields by up to 0.7%, *i.e.*, the implied corrections are smaller for $f_{\text{broad}}^{\text{realistic}}$ by up to 0.7% compared to $f_{\text{broad}}^{\text{mono}}$.

To consider both the field-size effect on stopping-power ratio and using stopping-power ratio data for realistic beams, the factor $f_{\text{f.s.}}^{\text{realistic}}$ is calculated. In Table 5.1, the values of factors $f_{\text{broad}}^{\text{mono}}$ and $f_{\text{f.s.}}^{\text{realistic}}$ are very close for every field size for a given energy. The analysis of factors $f_{\text{f.s.}}^{\text{mono}}$ and $f_{\text{broad}}^{\text{realistic}}$ above shows that the field-size effect and the difference between using realistic and mono-energetic stopping-power ratio data are in the opposite directions for the correction factors, thus tend to cancel each other in the factor $f_{\text{f.s.}}^{\text{realistic}}$. In principle, using $f_{\text{f.s.}}^{\text{realistic}}$ is the most accurate correction. The calculations show that the difference between $f_{\text{broad}}^{\text{mono}}$ and $f_{\text{f.s.}}^{\text{realistic}}$ is not more than 0.4%, which means, from the view of clinical practice, following TG-25, *i.e.*, using $f_{\text{broad}}^{\text{mono}}$, will correct the error due to using Eq. 5.3 in the ROF measurement to within 0.4%.

In the example of $(\bar{L}/\rho)_{\text{air}}^{\text{water}}$ versus depth for a Varian Clinac 2100C accelerator (Fig. 5.2(d)), the difference between the values of $(\bar{L}/\rho)_{\text{air}}^{\text{water}}$ for realistic and mono-energetic beams at $d_{\max}$ in a 10×10 cm^2 field is well compensated by the difference between the $(\bar{L}/\rho)_{\text{air}}^{\text{water}}$ values for 10×10 cm^2 and 2×2 cm^2 fields at the $d_{\max}$ of the 2×2 cm^2 field (not shown in the figure). The difference between using $f_{\text{f.s.}}^{\text{realistic}}$ and $f_{\text{broad}}^{\text{mono}}$ is thus smaller than 0.4% which is the difference for the same case but for the MD2 machine.

For other clinical accelerators which produce "dirtier" beams (which means more scattered component in the beams), the d_{max} shift is smaller compared to that of the MD2 machine which produces beams which are closer to mono-energetic beams. This is especially true for high-energy beams. Although the difference in values of $(\bar{L}/\rho)_{air}^{water}$ between realistic and mono-energetic beams can be quite large at d_{max} for broad beams (up to 1.4%[81]), the change in the ratio of $(\bar{L}/\rho)_{air}^{water}$ for realistic versus mono-energetic beams with a small change in d_{max} is usually small. Considering the field-size effect on $(\bar{L}/\rho)_{air}^{water}$, which is in the opposite direction to the change in this ratio, the difference between using $f_{f.s.}^{realistic}$ and f_{broad}^{mono} is not expected to be significantly worse than the results for the MD2 machine.

Burns *et al.*[105] gave a single function which calculates $(\bar{L}/\rho)_{air}^{water}$ values for 10×10 cm^2 realistic beams as a function of R_{50} over a large range of depths in a water phantom. Using $(\bar{L}/\rho)_{air}^{water}$ values from this program (available at http://www.irs.inms.nrc.ca/inms/papers/SPRR50/sprR50.html) gives a result similar to $f_{broad}^{realistic}$ (less than 0.3% difference). Since this differs more from the values of $f_{f.s.}^{realistic}$ than f_{broad}^{mono}, there is nothing gained from using this more accurate function for broad beams in this application.

5.3 Summary and conclusions

It has been confirmed that when measuring ROFs for small field sizes using ion chambers, considerable care must be taken to follow TG-25, *i.e.*, insure that variations in the values of $(\bar{L}/\rho)_{air}^{water}$ and other factors are taken into account. Ignoring the variation in $(\bar{L}/\rho)_{air}^{water}$ due to the change of depth of the measurement point as the field size gets smaller can lead to overestimates of the ROF by up to 3%.

It has been shown that the stopping-power ratio is a function of field size and it leads to errors in ROF of up to one-half percent for small fields if this effect is not

considered.

Values of stopping-power ratio also vary with accelerator. Using stopping-power ratio data for mono-energetic beams instead of those for realistic beams introduces an error in ROF of up to 0.7% for small fields but in the opposite direction of the field-size effect.

Since the error from using stopping-power ratio data for broad beam and the error from using stopping-power ratio data for mono-energetic instead of realistic beams tend to cancel each other, following TG-25 will give an ROF result which is accurate within 0.4% for small fields for an MD2 machine. Due to the smaller d_{max} shift for other accelerators with beams which are less mono-energetic, this upper estimate of the error in using the mono-energetic broad beam data will still be correct.

Chapter 6

Cutout Factors for Square Fields

6.1 Purpose of the cutout factor study for square fields

Square fields are most commonly used in clinics. Although they are simplest in shape and hence look to have the easiest ROFs to calculate, cutout factors for most square fields are usually measured during accelerator commissioning. For those square fields which do not have measured ROFs, either the 1-D method[19] (discussed in Chapter 7) or extraction from data of ROF versus field size[19], is recommended for obtaining the ROFs. Both methods require a lot of measurements. In this chapter, Monte Carlo calculation of cutout factors for square fields is discussed with respect to accuracy and as a tool to analyze the features.

6.2 Comparison of ROF measurements using two detectors

Cutout factors are defined in Eq. 1.5 (page 6). Two detector systems are used in the cutout factor measurements for a Siemens MD2 accelerator at the Ottawa Regional Cancer Centre, a silicon diode and an ion chamber.

For the measurements using a silicon diode detector, the relative outputs do not need stopping-power ratio nor polarity effect corrections which are needed for the measurements using an ion chamber[19,60,63]. The data for the ion chamber measurements are corrected for stopping-power ratio changes due to different values of d_{max} and field sizes as discussed in Chapter 5[63]. After the stopping-power ratio corrections for ion chamber measurements, the most recently measured ROFs using an ion chamber agree with those made using the silicon diode system within 1% for all measured cutout sizes except the 2×2 cm^2 cutout for 6 MeV at SSD = 100 cm for which the ROF value from the ion chamber measurement is about 2% lower. The discrepancy

is likely related to a slight offset of the ion chamber from $d_{\max}$ in the phantom. The recent measurements using an ion chamber were originally to check the polarity effect of this ion chamber system since the previously measured ROFs using an ion chamber differed by up to 3% compared with ROFs measured with the silicon diode detector. The reason for the discrepancy was thought to be the polarity effect on the ion chamber system which, according to Aget and Rosenwald[60], was supposed to lead to a change by about 3% for the field-size range of 2×2 cm^2 — 10×10 cm^2. Surprisingly, the measured polarity effect for the RK chamber (0.12 cm^3) which was used in the measurements is less than 1% for the above field-size range. A possible explanation is that most of the polarity effect is due to cable induced effects and that the shielding of the cable changed between the two sets of measurements.

6.3 Results

All the depth-dose curves from calculations agree with measurements very well (a few are shown in Fig. 2.9, page 33, Fig. 2.10, page 34, and more in Appendix B). The absolute values of dose at $d_{\max}$ per incident particle are picked up from these calculated depth-dose curves and the output factors are calculated using these values.

6.3.1 Cutout factors

Fig. 6.1 shows the measured and calculated cutout factors for several different energies of electron beams for a 10×10 cm^2 applicator, at SSDs of 100 cm and 115 cm. Both curves in each plot are normalized to the open applicator which defines a 10×10 cm^2 field at SSD = 100 cm or a 11.5×11.5 cm^2 field at 115 cm. The difference between the measurement and the calculation is up to about 1%. The measurement data using the silicon diode system are used in this comparison. Similar agreement is found for data for the 15×15 and 20×20 cm^2 applicators (Fig. 6.2).
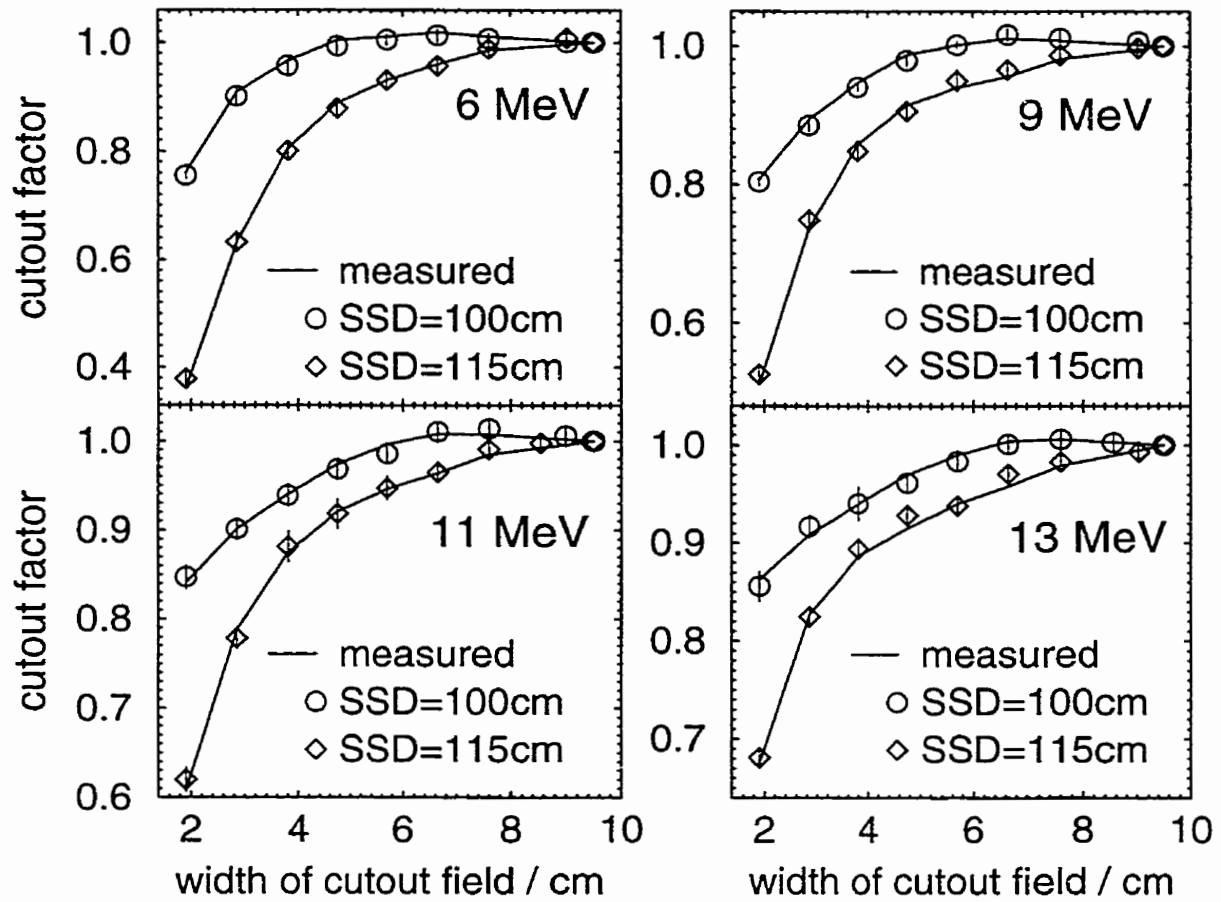
Figure 6.1: Calculated and measured cutout factors for 6, 9, 11 and 13 MeV beams. The reference field is the open applicator which defines a 10×10 cm^2 field at SSD = 100 cm. Note the different scales and the one standard deviation error bars. The measurements are performed using a silicon diode detector. The difference between the calculations and measurements is up to about 1%. The experimental data were measured at the Ottawa Regional Cancer Centre by Dr. Joanna Cygler.

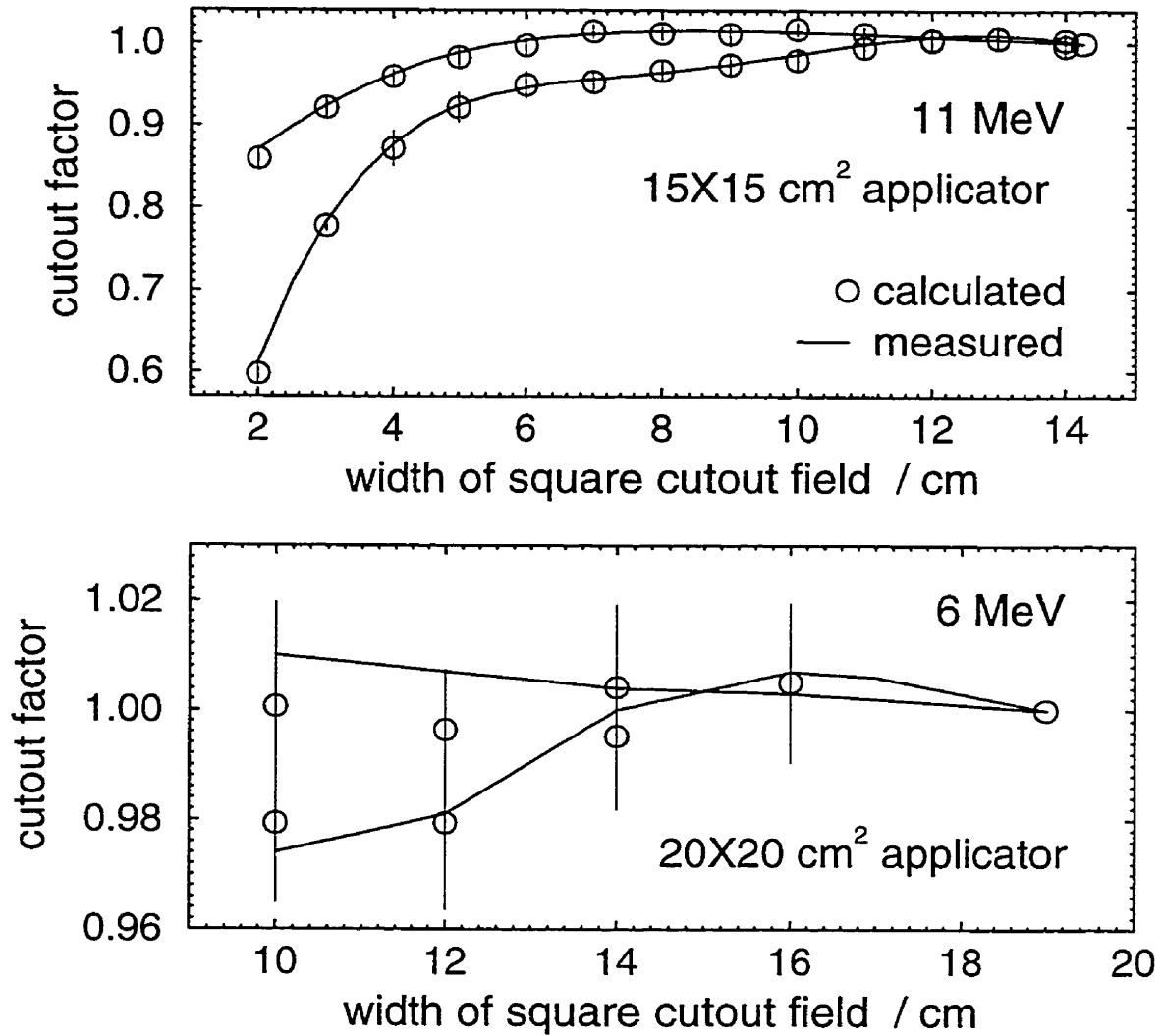Figure 6.2: Cutout factors for 15×15 and 20×20 cm^2 applicators for an MD2 linac. Calculations and measurements agree within 1%. The experimental data were measured at the Ottawa Regional Cancer Centre by Dr. Joanna Cygler.

6.3.2 Direct and scattered components

Fig. 6.3 presents contributions from the components to the total output versus cutout size for the 11 MeV beam with 10×10 cm^2 applicator at SSD = 100 and 115 cm, and with 15×15 cm^2 applicators at SSD = 115 cm, as well as a 6 MeV beam with 10×10 cm^2 applicator at SSD = 100 cm. In all cases, the difference between the output of the open applicator and the 2×2 cm^2 cutout is mainly due to the direct electrons and particles scattered off the applicator.

Although the real beam is not an ideal parallel beam, and is not mono-energetic as was the case in Fig. 3.4 (page 49), the critical opening size to establish side-scatter equilibrium at d_{max} for the direct electrons still exists. As shown by the direct components of the ROFs in Fig. 6.3, the curve of the direct component reaches a plateau as the cutout size increases. This usually is not true for the total dose. In both the measurements and calculations, as the cutout size increases at SSD = 100 cm, the total output decreases slightly after it reaches the highest point (see Fig. 6.1). According to the definition, side-scatter equilibrium at d_{max} still exists with large cutouts. The decrease of the total dose with further increase of the cutout size is caused by the reduction of the dose from the component scattered off the applicator. The reason for the reduction is that most of the scattered particles are from the edge of the opening (Fig. 6.4), and as the cutout size increases, the edge of the cutout is getting further away from the central axis, thus many electrons scattered off the cutout, usually with low energy, can no longer reach the central axis at d_{max}. This component thus contributes less dose to the total dose at d_{max}, however, the dose from the direct electrons remains the same after a certain cutout size. It is always true that the plateau exists for the dose from the direct electrons when the cutout size is large enough to establish side-scatter equilibrium at d_{max}.

Because the direct electrons undergo only multiple scattering in the air between the monitor chamber and the phantom, most of them have high energy and are
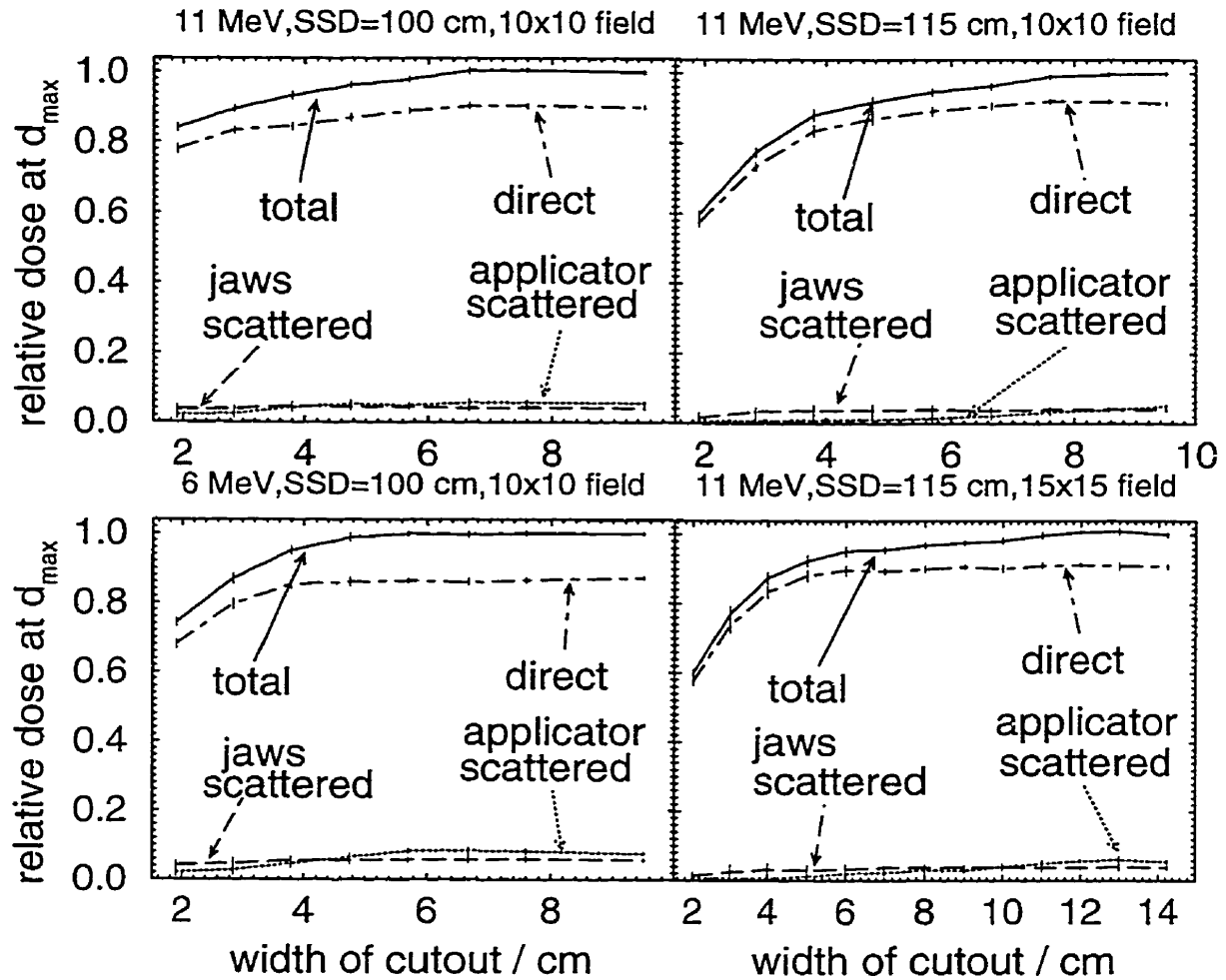
Figure 6.3: Contributions of dose components to relative output factors. The major change in the output versus cutout size comes from the direct electrons (6.5% between open 10×10 cm^2 and 3×3 cm^2 cutout for 11 MeV beam at SSD $=$ 100 cm, the total change is 10%) while the scattered component from the photon-jaws is relatively flat and the scatter from the applicator contributes a 3% change for the same beam. At SSD $=$ 115 cm, the difference between the outputs of open applicator and 3×3 cm^2 cutout is greater than that at SSD $=$ 100 cm, and the direct electrons contribute more to the difference. On the other hand, the lower the beam energy is, the greater the difference is, and the more the scattered components contribute to the difference. All the curves are normalized to the total dose at d_{max} of each open applicator.
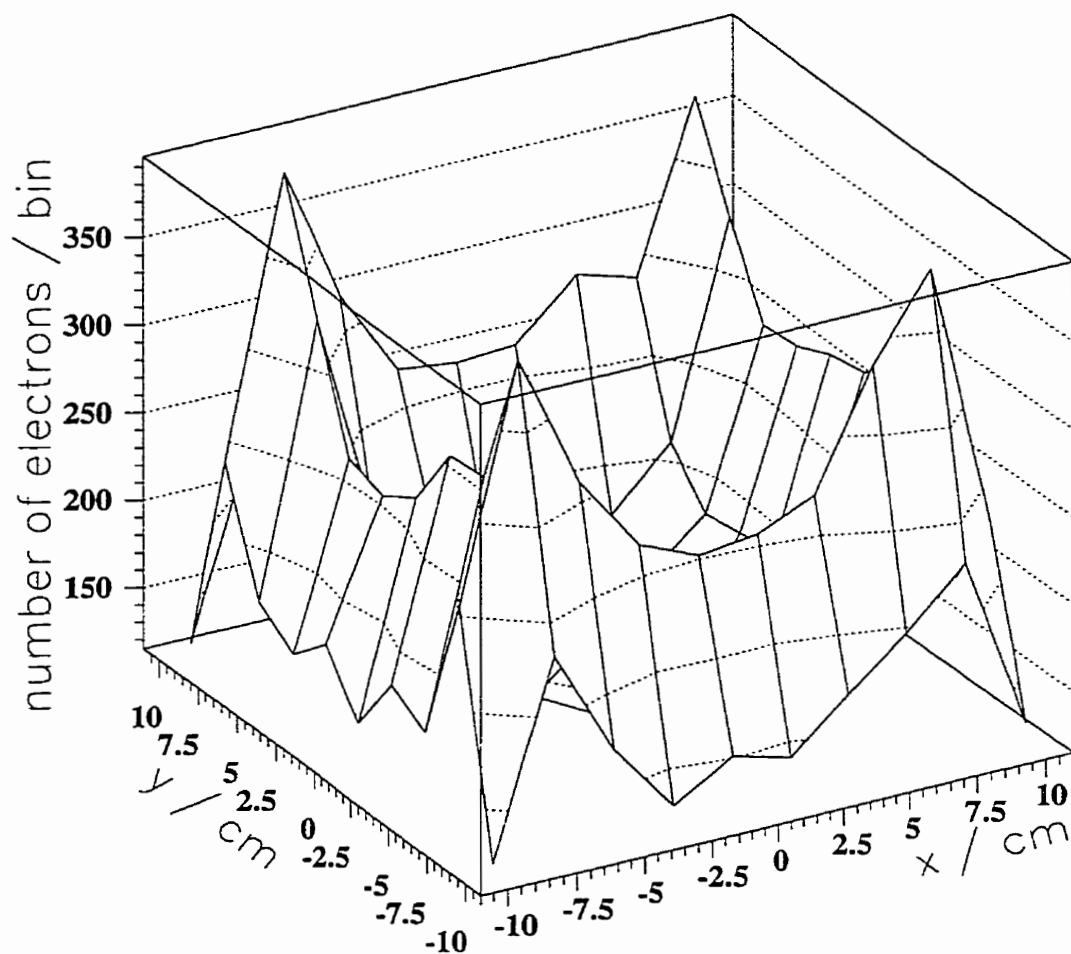
Figure 6.4: Planar fluence distribution at the phantom surface of the electrons scattered from the last scraper, SSD = 100 cm. The field size is 15×15 cm^2. The energy of the beam is 11 MeV. Most of the electrons are from the edge of the scraper. This figure is obtained by analyzing the phase space output at the phantom surface by using PAW software[106].
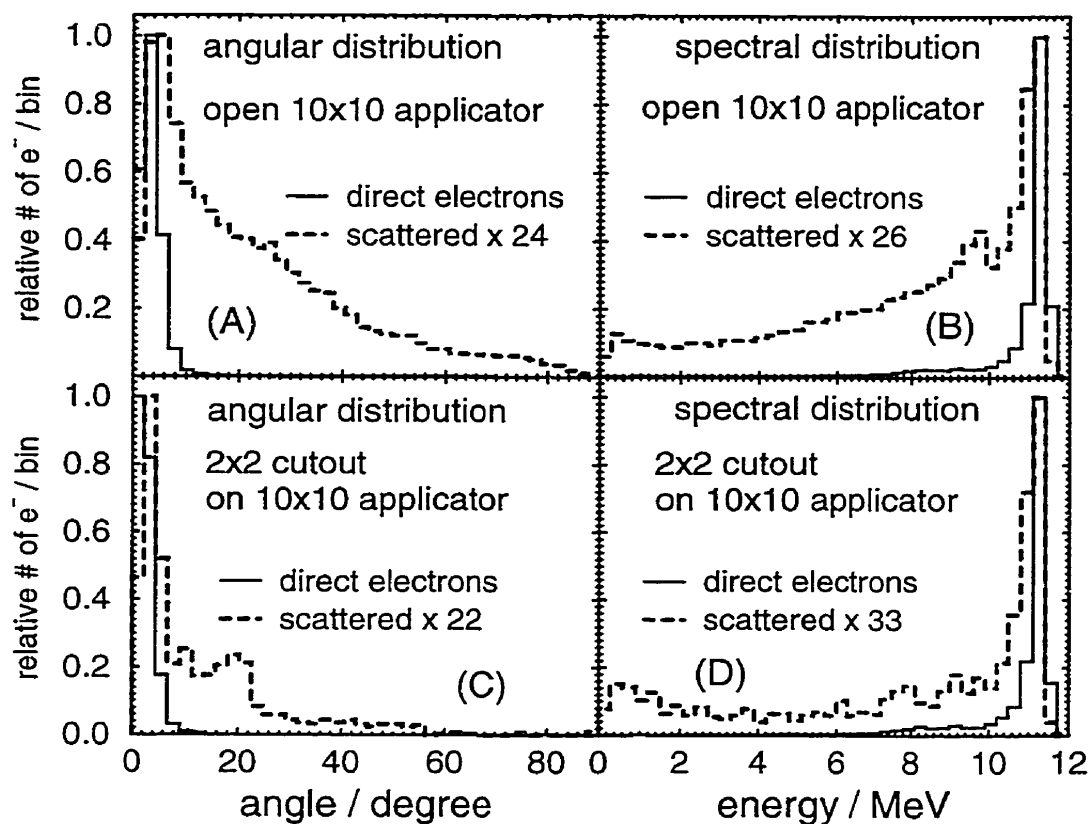
Figure 6.5: Angular (A, C) and spectral (B, D) distributions inside the 11 MeV beam for an open applicator of 10×10 cm^2 (A, B) and 2×2 cm^2 cutout (C, D) at the phantom surface. Most of the direct electrons go forward with high energy (the dip at 0° is a solid angle artifact). The lower peak in the scattered electrons curve in (B) is created by electrons going through the first scraper. There are 40 equal bins in each curve. The scattered component is normalized to the peak of the direct component.
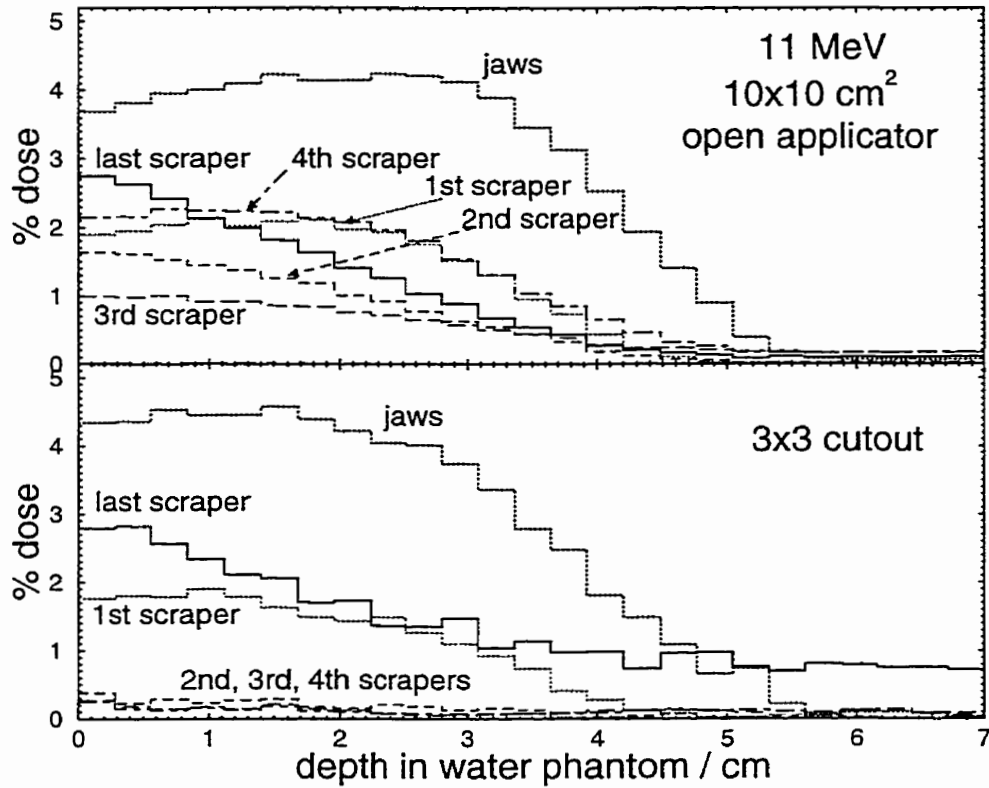
Figure 6.6: Scattered-component depth-doses for 11 MeV beam, 10×10 cm^2 applicator, SSD $= 100$ cm. Both cases are normalized to its own total dose at $d_{\max}$ which is 10% less for the 3×3 cutout case. Doses are from both electrons and photons.
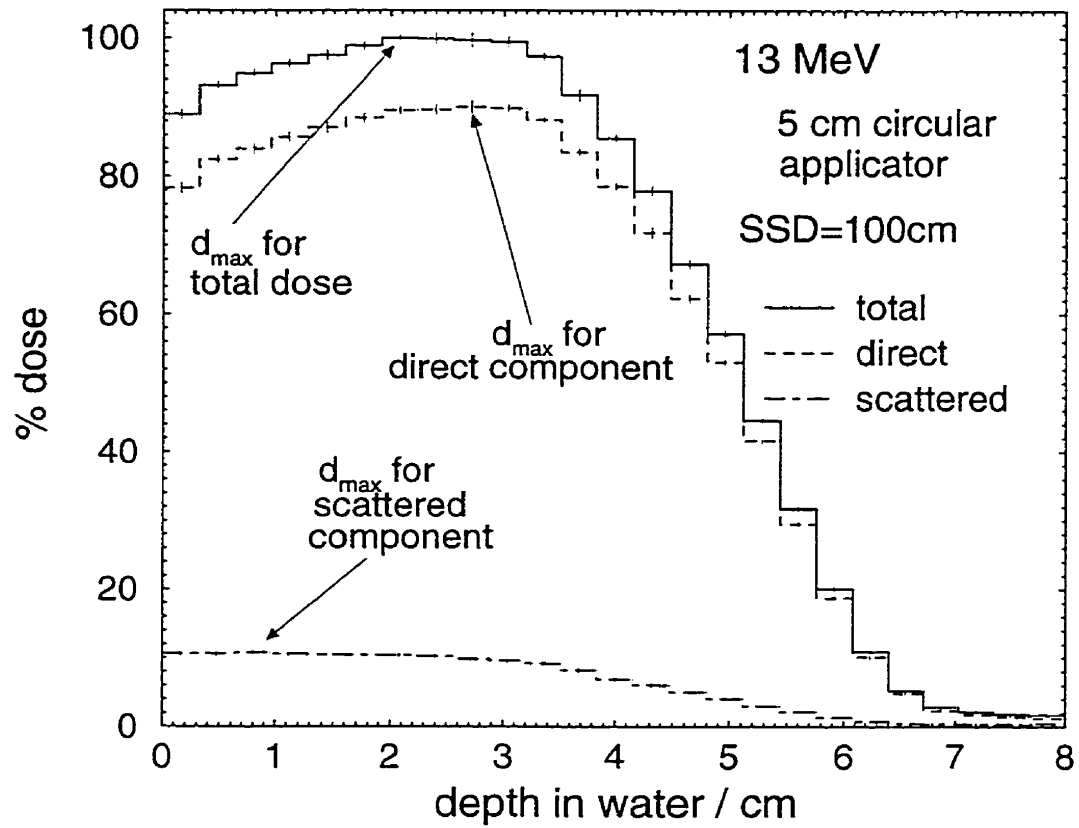
Figure 6.7: Values of d_{max} for different components. With higher mean energy, the d_{max} for the direct component is deeper than that for the total while that for the scattered component is closer to the surface.

going towards the central axis at a large angle.

At d_{max}, the scattered components are about 10% of the dose for the large fields. About half the scattered component dose comes from the photon-jaws. The other half comes from the scrapers. For those fields smaller than 4×4 cm^2 at SSD $= 100$ cm, the scattered component from the scrapers is less because of the blocking effect of the cutout.

Usually, the scattered components contribute only a few percent to the output. These components have lower energy than the direct component(see Fig. 6.5). Thus they contribute relatively more to the surface dose than to the dose at d_{max}, and move the d_{max} of the total depth-dose curve towards the surface (Fig. 6.7).

6.3.3 Contaminant-photon component

In the small field in Fig. 6.6, the dose from the cutout has a higher bremsstrahlung tail than in the large field. This is because there are many more high-energy electrons hitting the cutout in the small-field case, thus creating more photons that reach the phantom and contribute to this tail in the depth-dose curve. The photon tail from this component is less than 1% of the total dose at d_{max}.

The number of contaminant photons often exceeds the number of electrons for high-energy beams and small field sizes, but the dose contribution from photons is low and often negligible. The dose contribution from contaminant photons depends on energy and cutout size. The higher the energy is, the higher the contaminant photon dose will be since bremsstrahlung is more likely with high-energy electrons. Also the contaminant dose is higher for smaller cutout sizes. Table 6.1 shows the dependence of the contaminant dose on the beam energy and cutout size for the 10×10 cm^2 applicator at SSD $= 100$ cm. In the table, contaminant dose at d_{max} is normalized to the total dose at d_{max} of its own beam.

Table 6.1: Calculated contaminant photon dose at d_{max} versus energy and cutout size for the Siemens MD2 accelerator

beam	6 MeV		13 MeV	
field	open applicator	2x2 cutout	open applicator	2x2 cutout
photon dose	0.25%	0.72%	1.9%	3.1%

6.4 Summary and conclusions

It has been shown that Monte Carlo calculations for cutout factors agree with careful measurements within 1%. Thus Monte Carlo simulation can be an alternative to measuring ROFs versus cutout size in commissioning a clinical accelerator. Furthermore, it offers a powerful tool to better understand the related physics.

The output factor from the direct dose component will reach a plateau when the side-scatter equilibrium at d_{max} is established.

The scattered component, especially the particles from the last scraper/cutout, is also important to the beam output. It usually contributes about 10% to the total output.

The contaminant photon component contributes less than 1% to the total output for low energy beams and about 3% for 13 MeV beams. The larger the cutout, the less the contaminant dose component.

Chapter 7

Cutout Factors for Other Non-Square Fields

7.1 Advantage of *BEAM* in irregular-field calculations

In Chapters 3,4 and 6, Monte Carlo studies of ROFs for square fields are presented. One of the advantages of the *BEAM* code is that it can handle an arbitrary shape of field. Many other algorithms are designed for some specific field shapes. For example, SQRT for square fields and 1-D for rectangles. Although some algorithms claim that they work for arbitrary fields, due to their complexity, no one is actually using them routinely. In this chapter, examples are given for different field shapes to show that *BEAM* is general, flexible and accurate for ROF calculations.

Cutout factors are easier than applicator factors to calculate with Monte Carlo methods, even for irregular fields, since only the cutout changes and the upstream collimation system remains the same. This means that such calculations are not as sensitive to the details of the upstream collimation geometry as the applicator calculations, because the effects of the improperly simulated geometry cancel out when the output is normalized to that of the open applicator which shares the same improperly simulated upstream geometry. That is also why several other algorithms work without details of the collimation geometry. But this does not mean Monte Carlo methods can tolerate any kind of improperly simulated geometry, and it is important to model the accelerator accurately to ensure correct answers even in extreme cases.

Although cutout factor calculations are less difficult for Monte Carlo methods, the importance of such calculations in clinical practice is not less, because it is the measurement of cutout factors for treatment planning that takes a lot of clinical physicists' time.

7.2 Circular fields

Fig. 7.1 presents a comparison of calculated and measured cutout factors for circular fields. The agreement is better than 1% which is similar to the previous results for square cutouts.

7.3 Rectangular fields

Fig. 7.2 shows a comparison between Monte Carlo calculations and measurements for ROFs for rectangular fields. The agreement is better than 1% for all cases studied. ROFs are also calculated using the SQRT and 1-D methods suggested by Mills *et al.*[19]. In these calculations, ROFs for square fields are needed for the SQRT method. For example, to calculate the ROF of a 9×4 cm^2 field, one needs ROFs for 9×9 and 4×4 cm^2 fields (see Eq. 1.6). Also, for the 1-D method, one needs ROFs for two rectangular fields to calculate an ROF (see Eq. 1.7). All the ROFs needed for the SQRT and 1-D methods are from Monte Carlo calculations. Thus the comparison in Fig. 7.2 is actually a Monte Carlo test of the SQRT and 1-D methods.

Since the SQRT method ignores the difference in scattering between the X and Y collimation systems[19], the difference in ROFs between the Monte Carlo and SQRT methods for long fields, *e.g.*, 9×2 cm^2 in the figure, is usually large, up to 4.5%. The 1-D method, on the other hand, which includes the scattering difference between X and Y collimation system, can predict ROFs within 1.5% for all the rectangular-field cases studied.
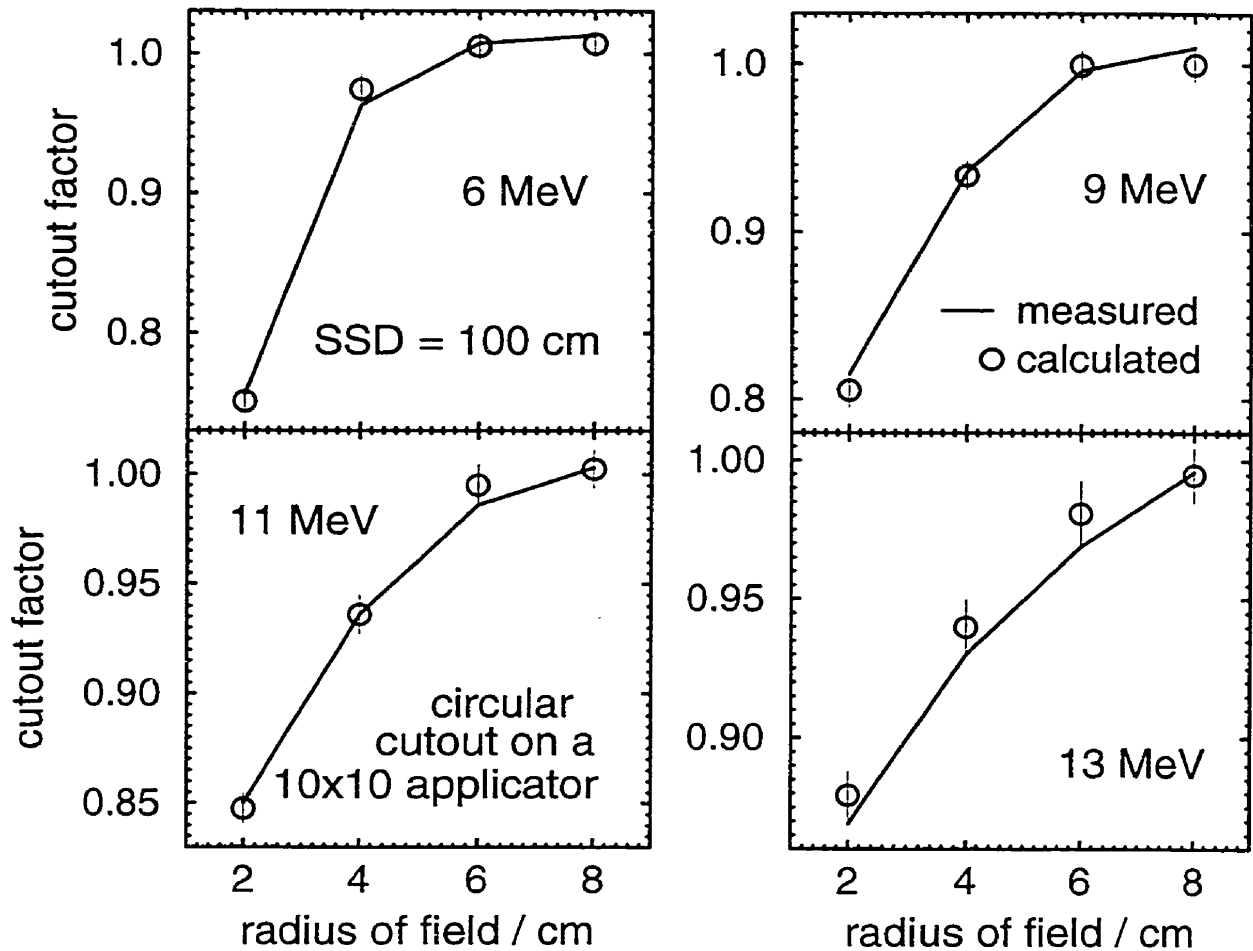
Figure 7.1: Measured and calculated cutout factors for circular fields for an MD2 accelerator. The agreement between calculations and measurements is better than about 1%. All cutout factors are relative to the open 10×10 cm^2 applicator. The experimental data were measured at the Ottawa Regional Cancer Centre by Dr. Joanna Cygler.
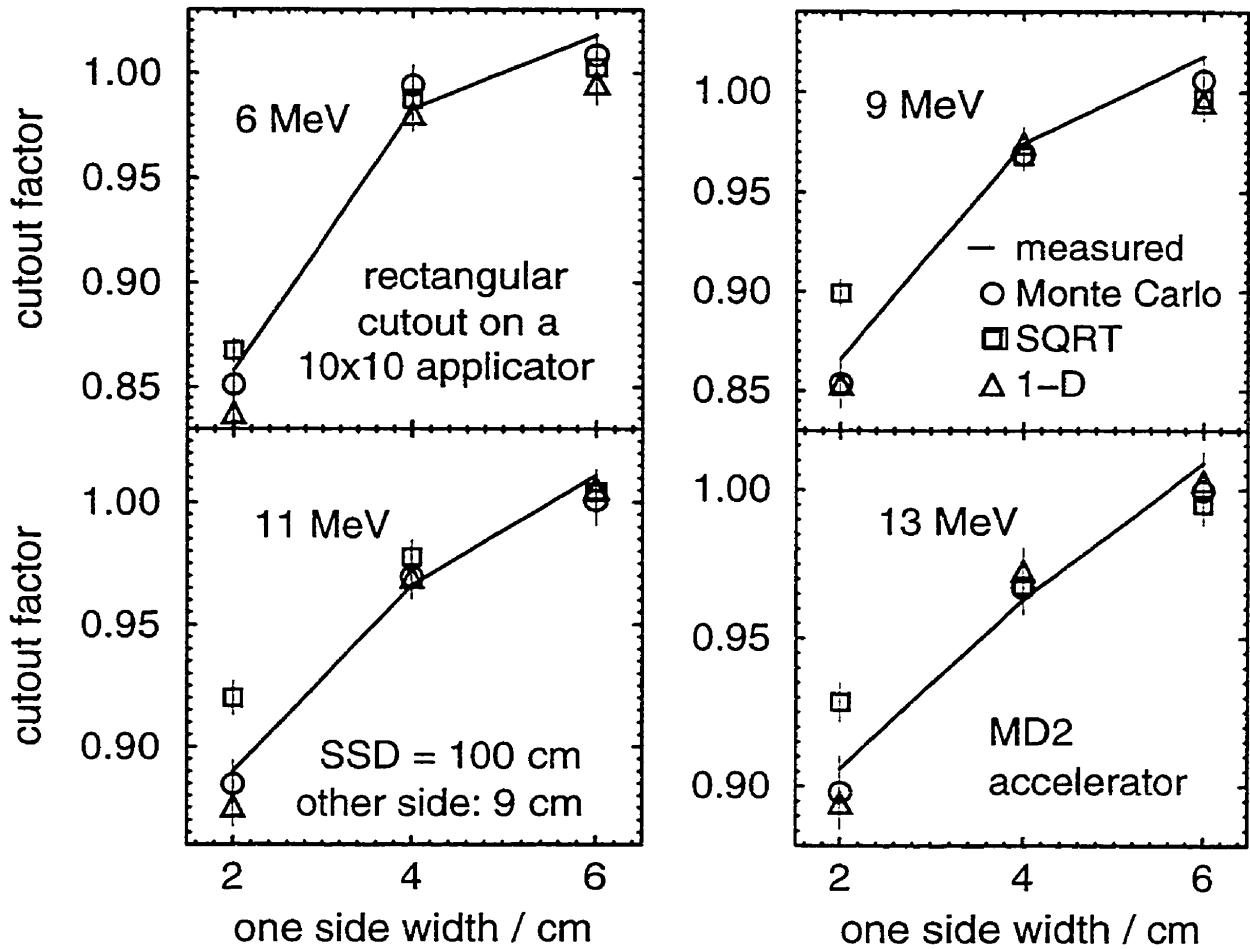
Figure 7.2: Measured and calculated cutout factors for rectangular cutouts in a 10 × 10 cm² applicator on a Siemens MD2 accelerator. The width of one side of all fields is fixed at 9 cm while the other side varies between 2 and 6 cm. The agreement between Monte Carlo calculations and measurements is better than about 1% for all cases studied. Monte Carlo calculations are also compared with calculations using the SQRT and 1-D methods suggested by Mills *et al.*[19]. The experimental data were measured at the Ottawa Regional Cancer Centre by Dr. Joanna Cygler.

7.4   Irregular fields

Two examples (Fig. 7.3 and 7.4) are given in this section to show that Monte Carlo calculated ROFs for irregular fields agree with measurements very well. Both cases show an agreement of better than 1% (Table 7.1).

Table 7.1: Two examples of ROF calculations for irregular cutouts for 13 MeV beams. The experimental data were measured at the Ottawa Regional Cancer Centre by Dr. Joanna Cygler.

cutout	applicator (cm^2)	SSD (cm)	measured ROF	calculated ROF
Fig. 7.3	15 × 15	115	0.969	0.976 ± 0.009
Fig. 7.4	20 × 20	100	1.013	1.007 ± 0.009

With component module *BLOCK*, *BEAM* is also capable of calculating ROFs for a cutout with multiple-openings.
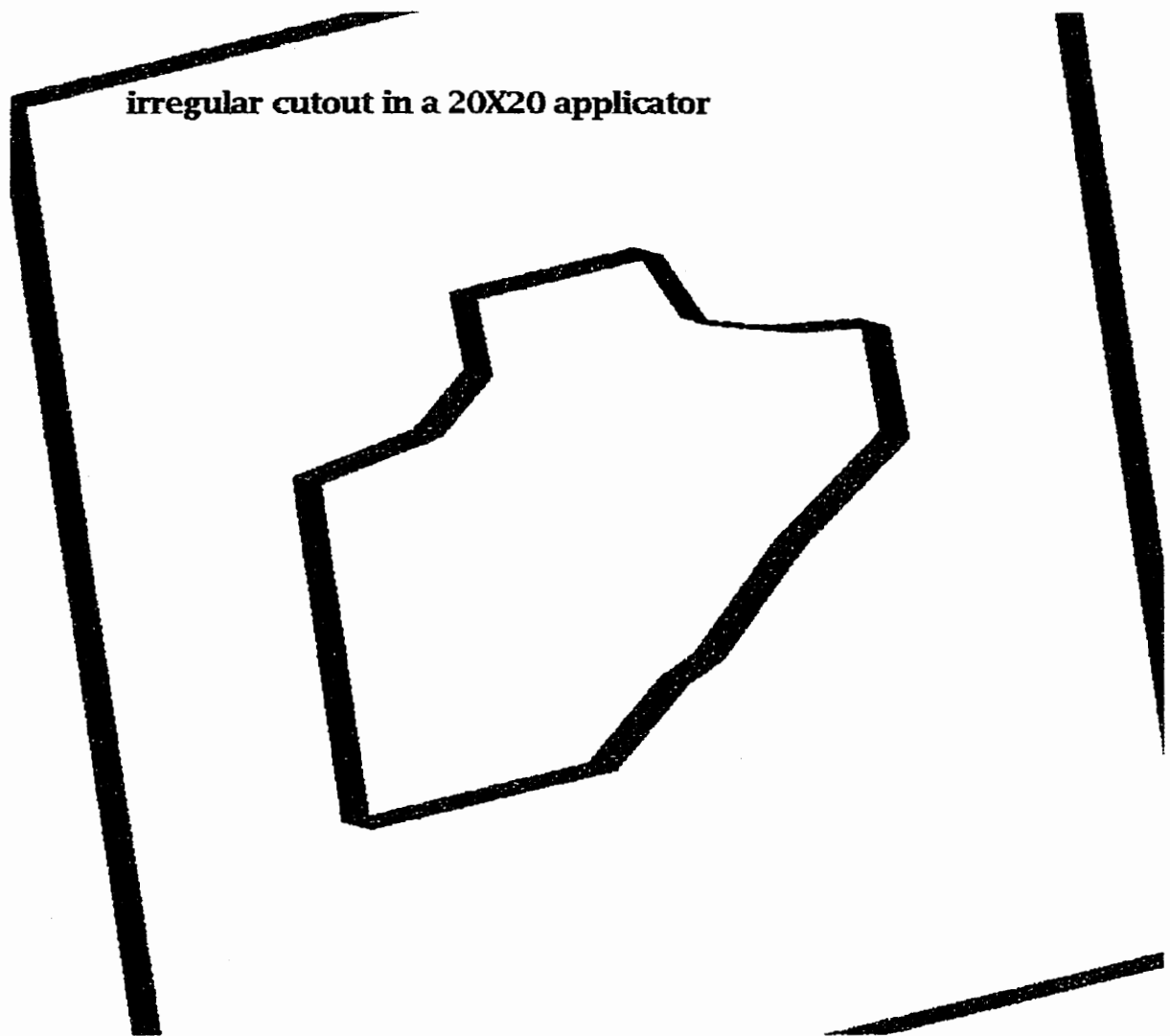
irregular cutout in a 20X20 applicator

Figure 7.4: Irregular cutout 2. Everything is the same as in Example 1 except that the applicator is 20×20 cm^2 and SSD = 100 cm. The opening edge is again closely approximated by using 14 straight lines.

Chapter 8

Summary

This study shows that Monte Carlo methods can be applied in electron-beam ROF calculations for clinical treatment planning. The calculated applicator factors agree with measurements within 2% for a Siemens MD2 accelerator and 1.5% for a Varian Clinac 2100C. Similar agreement is also found for the gap factors for an MD2 linac. All calculated cutout factors, including those for square, circular, rectangular and even irregular cutouts, agree with measurements within 1%. This agreement is better than the clinical tolerance which is usually about 3%. The statistical uncertainty for the calculations is around 1%.

Monte Carlo methods are simple to use in ROF calculations once the initial accelerator simulation is done. All ROFs, including applicator factors, gap factors and cutout factors are calculated in very similar ways. No special consideration is given to a specific ROF except component module *BLOCK* must be used in the calculations for irregular cutouts to define the desired arbitrary openings. This is a big advantage over other algorithms which usually are complicated and need a lot of measurement data and are usually designed for a specific kind of ROF calculation.

The study also shows that Monte Carlo methods are not only practical and accurate in clinical applications, but also help to understand the related physics which is difficult or even impossible to sort out by experiments. One of the useful features is that Monte Carlo can catalogue the particles into different components based on their history, such as direct, scattered electrons and contaminant photon, so that one can understand how the collimation system affects the beam outputs. This feature is used very often in the study of cutout factors. Also by using this feature, the reason why gap factors for large fields and high energy beams are larger than the inverse-square law prediction is found to be that the scattered component contributes more to the total output with a larger air gap. Another advantage is that one can set up the simulation either in vacuum or in the air so that one can obtain a clear idea how important the air scattering is for electron-beam outputs. The study of blocking and outscattering effects of air gaps and hence why electron-beam output does not follow

the inverse-square law for small fields has used this feature of *BEAM*, an *EGS*4 user code. The blocking and outscattering effects in small fields not only quantitatively explain the smaller gap factors than the inverse-square law predicts, but also quantitatively explain why applicator factors are so sensitive to the photon-jaw setting.

Stopping-power ratio for both mono-energetic and realistic-clinical beams can be calculated using Monte Carlo methods. *SPRRZ*, another *EGS*4 user-code designed for this specific task, is used, together with *BEAM*, for the calculations of stopping-power ratios for MD2 and Clinac 2100C accelerators. This study shows that the stopping-power ratio is a function of field size. It also varies with accelerator. Although the error from using broad-beam stopping-power ratio data which are recommended by TG-21 and TG-25 in ROF measurements using an ion-chamber, can be up to one-half percent and the error from using stopping-power ratio data for mono-energetic beams can be up to 0.7%, the overall error from using TG-21 or TG-25 data is less than 0.4% since the above two specific errors cancel each other, however, if d_{max} shifts are ignored for small beams, ROFs are overestimated by up to 3% due to the difference in stopping-power ratio values at different depths. This stopping-power ratio correction is needed for small beam ROF measurements if an ion-chamber is used.

All Monte Carlo calculations are done on a single Pentium Pro 200 MHz PC which takes about 6 hours of CPU time for an accelerator simulation and an additional 1–2 hours for each ROF. With the continuing rapid growth in computer power, Monte Carlo methods can be used for ROF calculations in clinics.

Future work

This study has accomplished the first step for the application of Monte Carlo methods in clinical-treatment planning, *i.e.*, accurately calculating ROFs for arbitrary fields. To implement Monte Carlo methods in clinical treatment planning, there is still a lot to be done.

Although it has been shown that ROFs can be calculated accurately for MD2 and Clinac 2100C accelerators using *BEAM* and the Monte Carlo calculated profiles of beams at different depths can be flattened to match the measured profiles by using a divergent electron source incident on the exit window, more details of the source geometry need to be studied further to give a general model of source type for different accelerators.

BEAM code is a big Monte Carlo program package. People need a lot of time and practice to get familiar with it. Even for *BEAM* experts, it is still time consuming to set up an accelerator with *BEAM* and mistakes are common in simulations. A possible solution would be that *BEAM* be commercialized and accelerator manufacturers provide the standard accelerator setups with *BEAM*. In this way, Monte Carlo techniques can be properly and efficiently applied in clinical treatment planning.

Appendix A: Input Files for Simulations

During the study, many input files are used in the Monte Carlo simulations for various purposes. For each model of accelerator, since many field sizes are applied clinically, there are about 5 different applicators and jaws settings and about 5 different energies to simulate. The number of the input files thus is very large for all the studies involved in this thesis.

As explained in Chapter 2, *BEAM* simulations for this study are usually divided into 2 steps, accelerator and phantom simulations, to save CPU time. Due to the requirement by the accelerator manufacturers that the mechanical data on the accelerator be kept confidential, the input files for the accelerator simulations are not included in this thesis. However, an example for the phantom part is given in Section A.1.3.

Although *BEAM* is used most often in this study, other *EGS*4 user-codes, such as *SPRRZ*, which is for stopping-power ratio calculations, *DOSRZ*, which is for dose distribution calculations in phantoms, are also used. An example of an input file for *SPRRZ* is also given in Section A.2.

For the meaning of each line in a *BEAM* input file, one should refer to the "BEAM Users Manual"[80].

A.1 *BEAM* simulations

A.1.1 Component module tests

After a component module is written, many test runs must be done to test its reliability and capability. To do such tests, an accelerator with this single component module of interest is built. The detailed geometry is in the input file for the simulation run. Many of these tests are to test the behavior of the CM under extreme conditions. In this section, the input file for the Canadian flag in Fig. 2.6 (page 28) is presented as an example of input files for CM tests. This input file is not for extreme-condition test, but just to show how wonderful this CM is.

```
block test: 12 MeV, Maple Leaf field
AIR700ICRU
4, 0, 0, 0, 0, 2, 0, IWATCH,ISTORE,IRESTART,etc
100., 87, 23, 500.0, 0, 0, 0, NCASE, etc
-1, 6, 0.0, 0.0, 4.0, 2.03,   rectangular source.
0, MONOEN
12.00000, BEAM ENERGY-monoenergetic
0.0, 5.0, 0.70, 0.010, 0, 1, 2.0, 0, ESTEPE,SMAX,ECUTIN,etc
0, 0, 0, 0, 0, IFORCE,NFMIN,etc
1, 1,        NSC_PLANES, IPLANE_to_CM
5, 1,        NSC_ZONES,MZONE_TYPE
0.70700, 1.0, 1.2250, 5.0, 7.07100,   RSCORE_ZONE
0, ITDOSE_OFF
0.00000,        Front of first CM with air
*********************************************
10.0
maple leaf-shaped cutout
1.0, 4.0, 6666.0
12,                12 sub-regions
4,         4 defining points in sub-region1
-0.12, -1.6,        x,y of point 1 in sub-region1
0.12, -1.6,      x,y of point 2 in sub-region1
0.12, -0.8,      x,y of point 3 in sub-region1
-0.12, -0.8,        x,y of point 4 in sub-region1
3,         3 defining points in sub-region2
0.12, -0.8,        x,y of point 1 in sub-region2
1.0, -1.0,      x,y of point 2 in sub-region2
0.8, -0.7,      x,y of point 3 in sub-region2
3,         3 points in sub-region3
0.8, -0.7,        of point 1 in sub-region3
1.7, 0.0,
1.5, 0.1,        end of sub-region3
6,         6 points in sub-region4
0.12, -0.8,
```

```
0.8, -0.7,
1.5, 0.1,
1.6, 0.75,
1.1, 0.6,
0.5, 0.3,              end of sub-region4
3,         3 points in sub-region5
0.5, 0.3,
1.1, 0.6,
0.9, 0.85,             end of sub-region5
4,         4 points in sub-region6
0.5, 0.3,
0.65, 1.3,
0.3, 1.2,
0.12, -0.8,            end of sub-region6
5,         5 points in sub-region7
0.0, 1.8,
0.3, 1.2,
0.12, -0.8,
-0.12, -0.8,
-0.3, 1.2,             end of sub-region7
4,         4 points in sub-region8
-0.3, 1.2,
-0.12, -0.8,
-0.5, 0.3,
-0.65, 1.3,            end of sub-region8
3,         3 points in sub-region9
-0.5, 0.3,
-1.1, 0.6,
-0.9, 0.85,            end of sub-region9
6,         6 points in sub-region10
-1.1, 0.6,
-0.5, 0.3,
-0.12, -0.8,
-0.8, -0.7,
-1.5, 0.1,
-1.6, 0.75,            end of sub-region10
3,         3 points in sub-region11
-1.7, 0.0,
-0.8, -0.7,
-1.5, 0.1,             end of sub-region11
3,         3 points in sub-region12
-1.0, -1.0,
-0.8, -0.7,
-0.12, -0.8,           end of sub-region12.
2.0, 2.02, -2.0, -2.02,          xpmax,ypmax,xnmax,ynmax
10.0, 12.0, 1, 0,      ecut, pcut, dose-zone, ir-to-bit for top air
11.5, 12.0, 2, 0,      ecut, pcut, dose-zone, ir-to-bit for opening and outs
AIR700ICRU
0.0, 0.0, 3, 3
MILDSTEEL700
*********************************************
```

A.1.2   Accelerator simulations

Most of this study concerns a Siemens MD2 linear accelerator. This accelerator has an electron-beam energy range from 6 to 13 MeV. For higher energies, a Siemens KD2, which has electron-beam energy up to 20 MeV, is simulated. The major geometry difference between these two accelerators is that the secondary scattering foil for an MD2 has 2 steps while the KD2 has 3. However, the CMs used for these two accelerators are the same, and thus the files for the accelerator building are the same for these two accelerators.

In this section, only the files to build the accelerators are presented. The input files for the simulations which contains detailed mechanical structures are not included for the reason mentioned at the beginning of this appendix.

The following is the file to build an MD2 accelerator in which the CMs in the MD2 accelerator are set up in the order from the exit window to the end of applicator:

```
CM names:   CONESTAK FLATFILT CHAMBER JAWS APPLICAT BLOCK BLOCK
Identifiers:  FOIL COLFOIL MONITOR MAINJAWS APP1 APP2 APP3
```

The last two *BLOCK* are used to simulate the scrapers with rounded corners in the applicator.

In this thesis work, an MD2 accelerator with a circular applicator is also simulated. The file for the accelerator building is different than the one for square applicators. The following is an example of the files for a circular applicator.

```
CM names:   CONESTAK FLATFILT CHAMBER JAWS APPLICAT CIRCAPP
Identifiers:  FOIL COLFOIL MONITOR MAINJAWS APP1 CIRCLE
```

CLINAC 2100C is a Varian linear accelerator. This machine is also used in the ROF study, and for the comparison of stopping-power ratios for realistic beams. The CMs file for this accelerator is following:

```
CM names:   CONESTAK CHAMBER CONESTAK MIRROR CONESTAK JAWS SLABS APPLICAT
Identifiers:  XSFOILS IONCHAM RING1 MIRROR RING2 MAINJAWS FWIN APPLICAT
```

A.1.3 Phantom simulations

Although the geometry for a phantom simulation is simple, it is also required to build an accelerator before any simulation. The accelerator which is actually a phantom must include a CM of *CHAMBER*. *CHAMBER* has the ability to calculate dose deposited along the central axis in a phantom. The file for the accelerator building for a phantom simulation is like following:

```
CM names:  APPLICAT CHAMBER
Identifiers:  CROBAND PHANTOM
```

APPLICAT is used to simulate the last scraper or the cutout above the phantom. The following is an example of input files for a phantom simulation. It is for a 2 × 2 cm^2 cutout for an 11 MeV beam.

```
last appli. + dose in phantom, 10x10, 2x2 cutout, 11MeV of e- from MD
AIR700ICRU
0,   0,   0,   1,   0,   0,   0, IWATCH,ISTORE,IRESTART,etc
20490724.,   33,   97,   200.0,   0,   1,   0,   NCASE, etc
-1,   21,   12.0,   1.0,   0.0,   0.000000,  IQIN,ISOURCE etc
/usr/people/gzhang/egs4/BEAM_MD/phsp/10_11Mup.egs4phsp1
0.04,   0.0,   0.70,   0.010,   0,   2,   2.0,   0, ESTEPE,etc
0, 0, 0, 0, 0, IFORCE,NFMIN,etc
1, 1,   scoring plane between thin air and phantom
5,1
2.8868, 4.0825, 5.0, 15.0, 17.0
1, ITDOSE_ON
2, 0
1
11,13,14,15,16,17,18,19
4
11
13,14
15,16,17,18,19
13,14,15,16,17,18,19
0.00000, Front of first CM with air
***************start of CM APPLICAT CUTOUT,   *************
16.00000, Outer boundary
cutout, cerrobend
9.99,   zback
1, 1,   # of layers, ishape(1 for rectangular opening)
8.70, 1.27, 0.95, 0.95, 7.30, 7.30, 0, 19
0.0, 0.0, 27, 21
CERROBEND700
**************start of CM CHAMBER PHANTOM *************
25.00000, Outer boundary
depth dose in phantom
14.98,   zmin
```

```
0,   26,   0
0.52,   14.00,   24.0
0.28,  26
0.70,    0.010,   1,   0
H20700ICRU
0.70,    0.010,   0,   0
H20700ICRU
0.70,    0.010,   0,   0
H20700ICRU
0.70,    0.010,   0,   0
H20700ICRU
0
**************end of all CMs****************
```

A.2 *SPRRZ* simulations

In Chapter 5, the study of stopping-power ratio corrections to ROFs for small fields is presented. Many stopping-power ratios are calculated for realistic and monoenergetic beams using Monte Carlo method. The code used for this purpose is *SPRRZ*. Here is an example of an input file for this code:

```
kd1020_2:nominal 20 MeV KD2 beam,2x2 on 10x10 phsp,
0, 0, 0, 0,    iwatch,istore,irstrt,idat,
8036680.0, 97, 33, 240.0, 0,   ncase,ixx,jxx,timmax
0,      slabs of equal thickness
0.0,     zplane--start of first slab
28, 0.3600,     28 slab in this group with thickness of .360cm
0, 0.0,     end of slab-groups
3,      # of cylindrical radii
0.5,     radius
1.0,
5.0,
2,     # of media,order:primary wall, cavity,the rest
H20521ICRU
AIR521ICRU
1, 1, 0,
0, 0, 0,   end of material info
2, 21, 0, 0.0, 0.0, 0.0
/usr/people/gzhang/egs4/BEAM_appli/phsp/kd1020_2.egs4phsp1
0.0, 0.0, 0, 0
0.0, 0.0, 0.0
0, 0, 0
0, 0, 0, 0, 0.0
```

It is for a 2×2 cm^2 cutout for a 20 MeV KD2 beam.

The following input file is for a stopping-power ratio calculation for a nominal 20 MeV monoenergetic beam. The energy of the beam is the mean energy of a nominal 20 MeV KD2 beam of 10×10 cm^2 field.

```
mo20kd:nominal 20MeV mono-energetic for kd2,field diameter 2 to 10 cm,
0, 0, 0, 0,    iwatch,istore,irstrt,idat,
1000000.0, 97, 33, 240.0, 0,   ncase,ixx,jxx,timmax
0,      slabs of equal thickness
0.0,    zplane--start of first slab
28, 0.360,     28 slab in this group with thickness of .36cm
0, 0.0,      end of slab-groups
5,      # of cylindrical radii
1.0,    radius
1.5,
2.0,
2.5,
5.0,
2,      # of media,order:primary wall, cavity,the rest
H20521ICRU
AIR521ICRU
1, 1, 0,
0, 0, 0,  end of material info
-1, 4, 0.5, 0.0, 0.0, 0.0
0
17.84
0.0, 0.0, 0, 0
0.0, 0.0, 0.0
0, 0, 0
0, 0, 0, 0, 0.0
```

Appendix B: Other Useful Figures

In the previous chapters, many figures are presented. These figures are just parts of the whole study. In this appendix, more figures are presented which may be of interest.
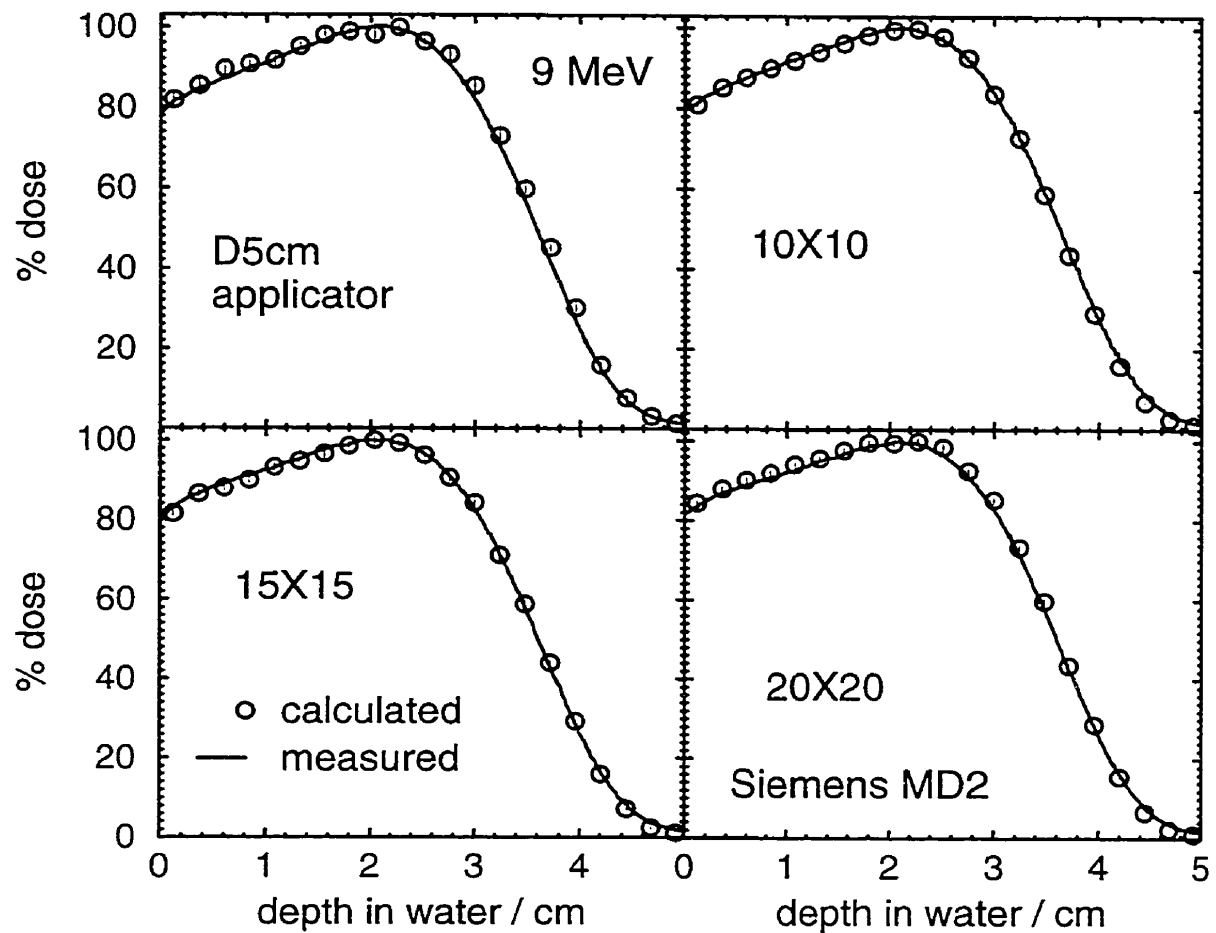
Figure B.2: Comparison of calculated and measured % depth dose curves for 9 MeV beams with open applicators for an MD2 accelerator.
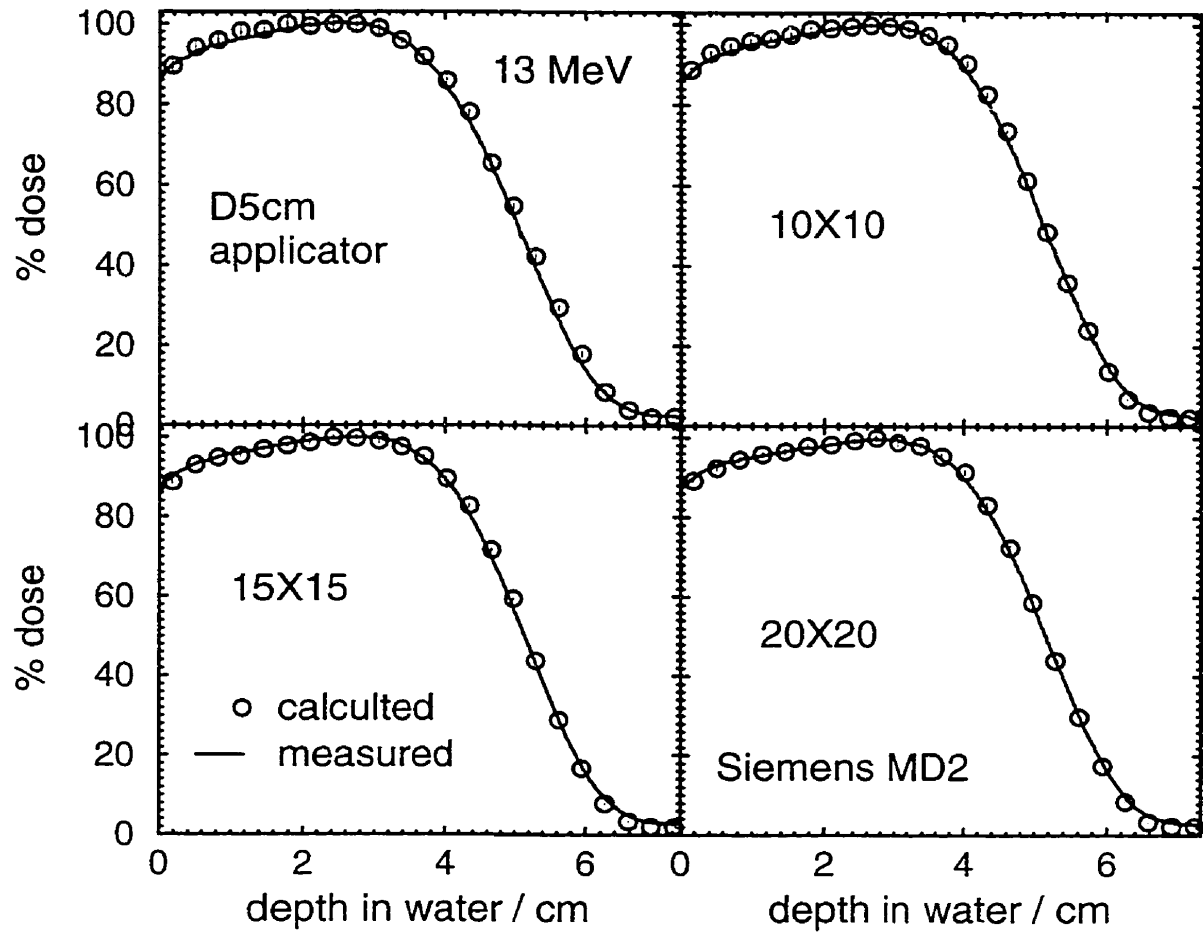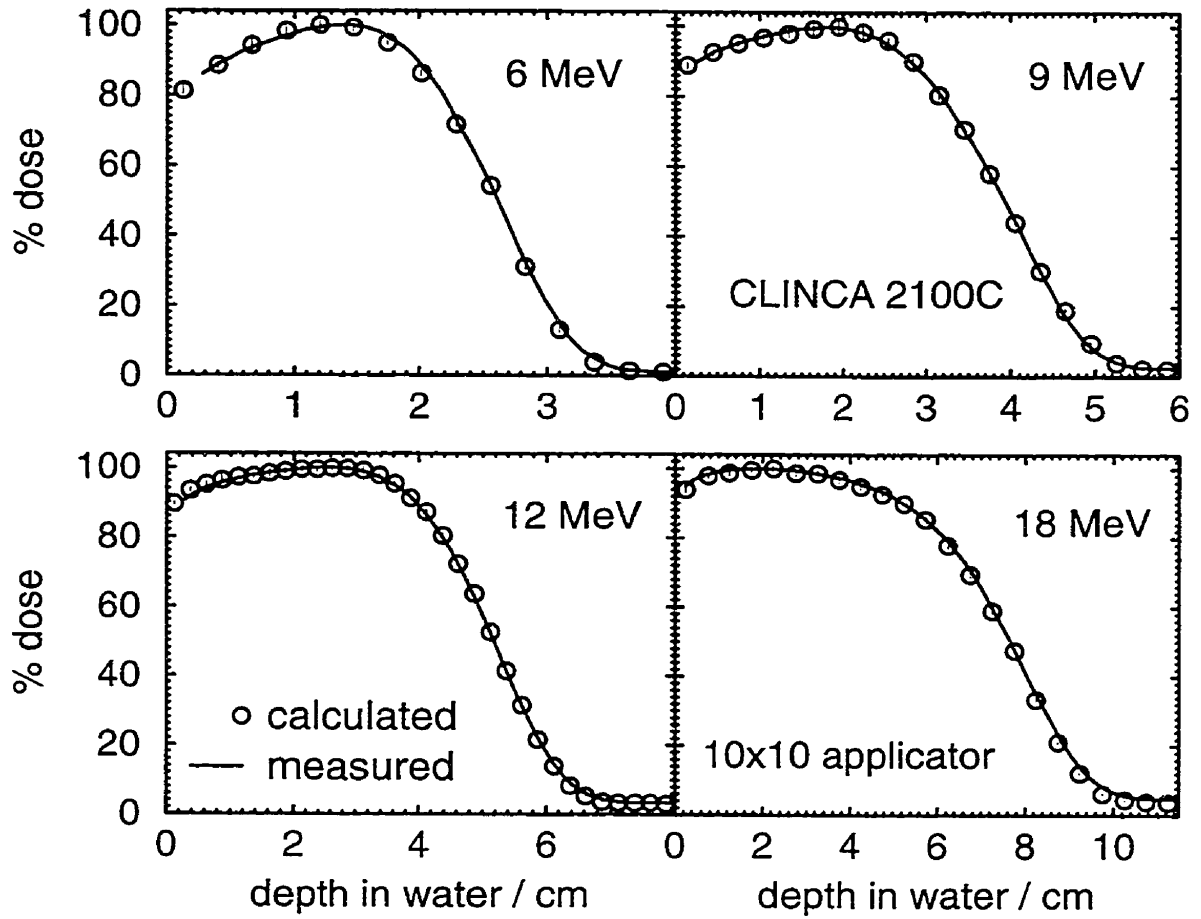
Figure B.4: Comparison of calculated and measured % depth dose curves for 13 MeV beams with open applicators for an MD2 accelerator.

Figure B.5: Comparison of calculated and measured % depth dose curves for Clinac 2100C beams for a 10×10 cm^2 open applicator.
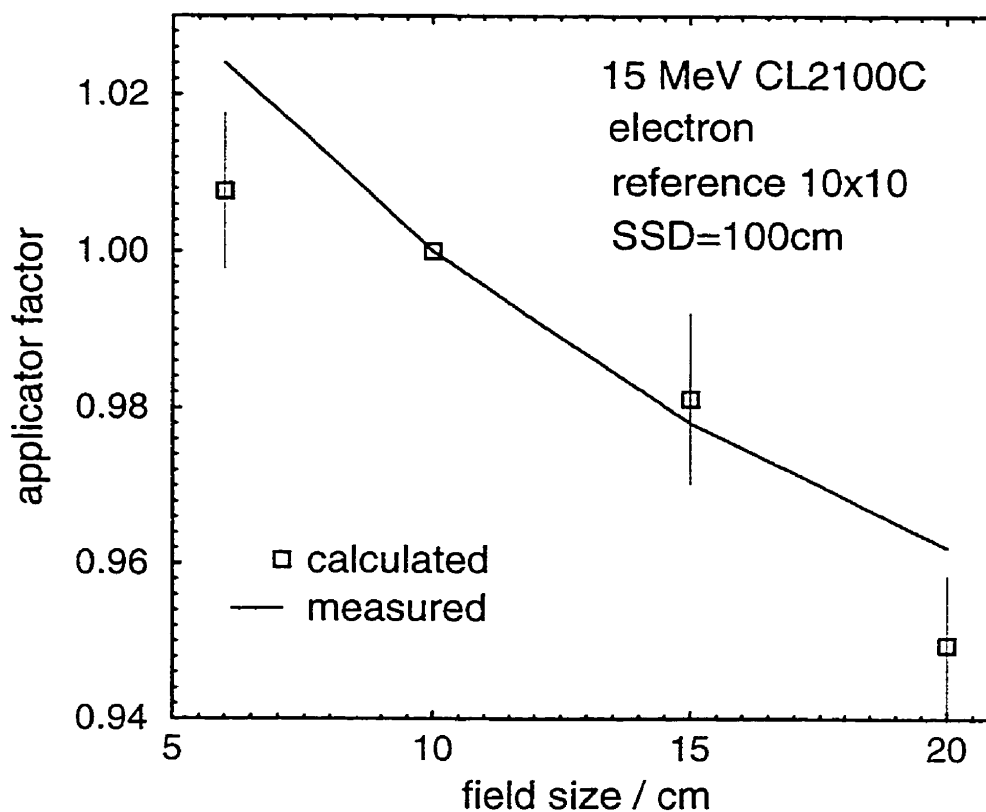
B.2 ROF figures

Figure B.6: Applicator factors for 15 MeV Clinac 2100C beams. Both calculated and measured ROFs are normalized to the output for 10×10 cm^2 beam. Calculations and measurements agree within 1.5%. The measured data in this figure are from Rock Mackie of the University of Wisconsin, Madison.
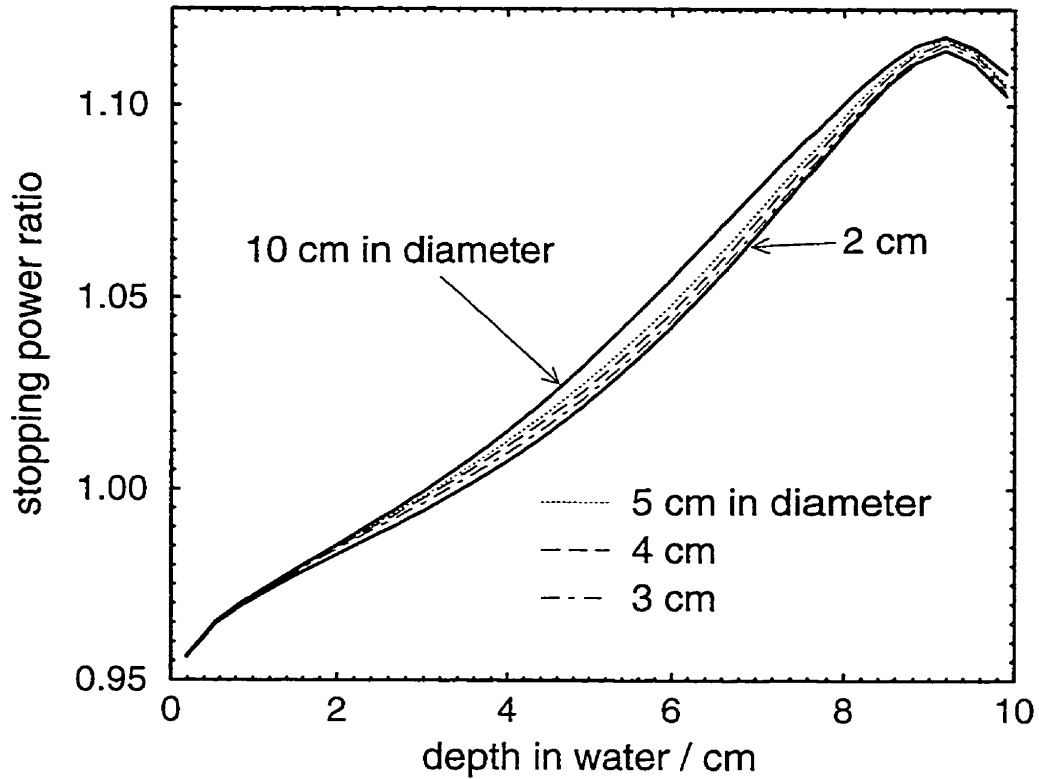
B.3 SPR figures

Figure B.7: Stopping-power ratio versus depth for mono-energetic nominal 20 MeV beams. The mean energy of a 20 MeV KD2 beam at SSD = 100 cm within the field defined by a 10 × 10 cm² applicator, which is 17.84 MeV, is used for the stopping-power ratio calculation for this figure so that the results can be compared with the stopping-power ratio values for realistic 20 MeV KD2 beams.
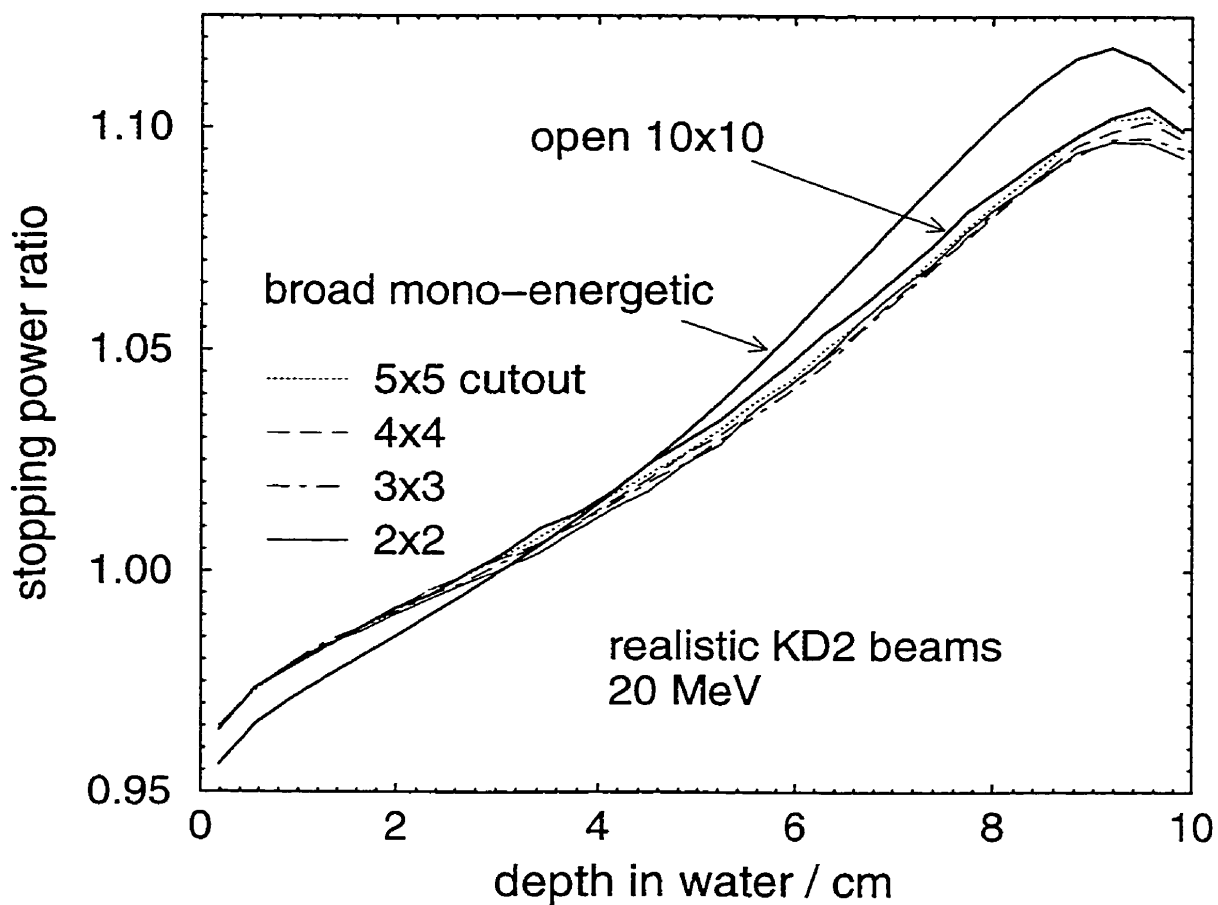
Figure B.8: Stopping-power ratio versus depth for realistic 20 MeV KD2 beams. The stopping-power ratio versus depth for broad mono-energetic beams, for which the same mean energy is used, are compared with the values for the realistic beams. Due to too few trials or number of histories, the statistical uncertainty of the calculations is not so good that the curves for small fields are mixed together and are not smooth.
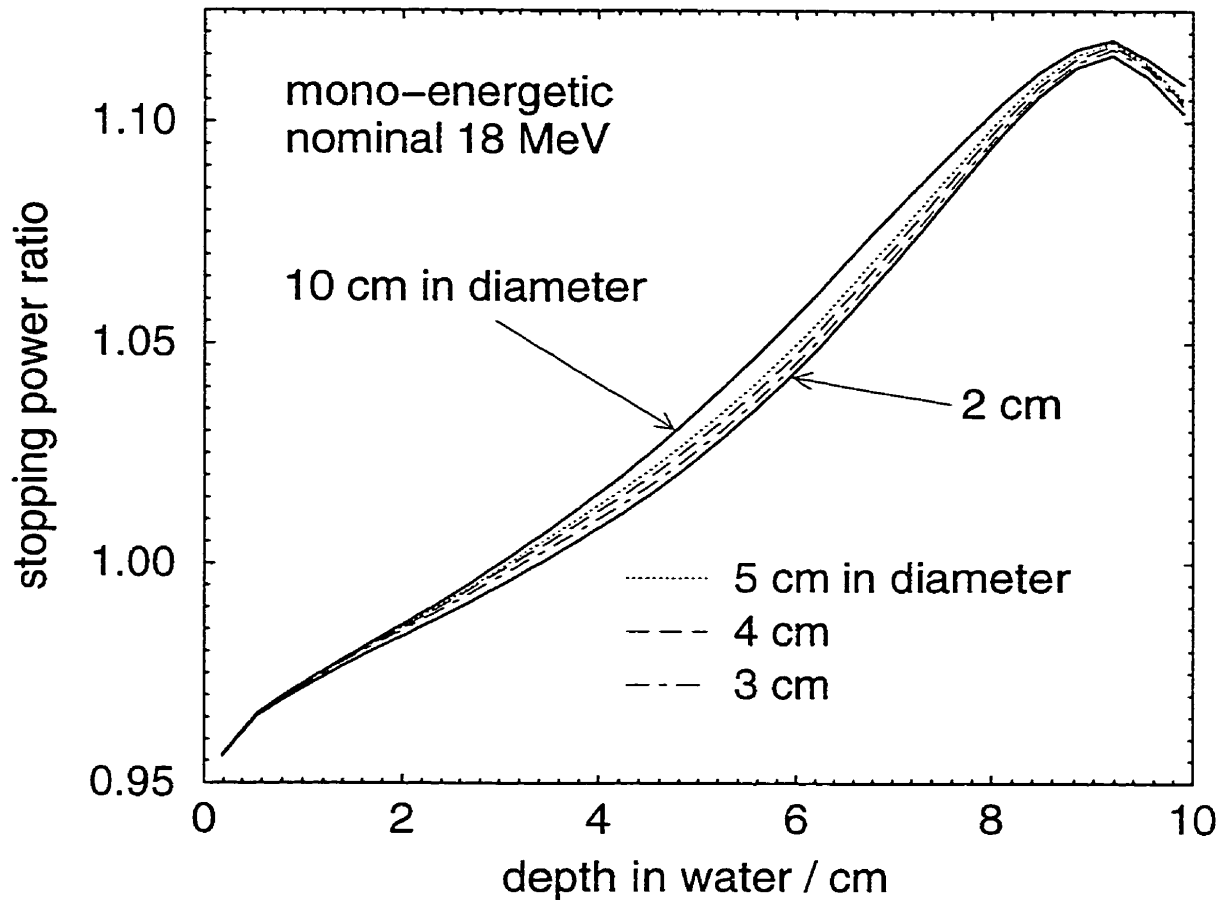
Figure B.9: Stopping-power ratio versus depth for mono-energetic 18 MeV Clinac 2100C beams. The mean energy of a 18 MeV Clinac 2100C beam at SSD = 100 cm within the field defined by a 10×10 cm^2 applicator, which is 17.72 MeV, is used for the stopping-power ratio calculation for this figure so that the results can be compared with the stopping-power ratio values for realistic 18 MeV Clinac 2100C beams.
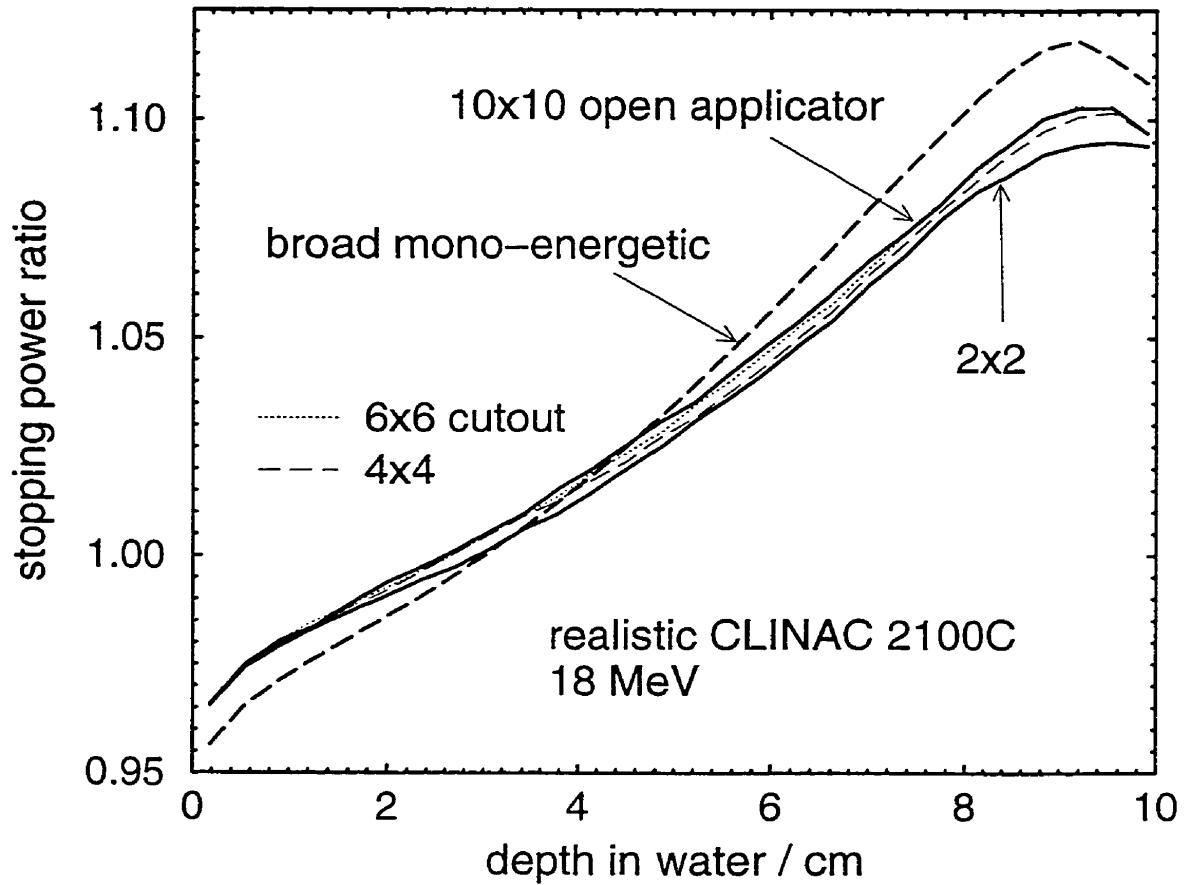
Figure B.10: Stopping-power ratio versus depth for realistic 18 MeV Clinac 2100C beams. The stopping-power ratio versus depth for broad mono-energetic beams, for which the same mean energy is used, are compared with the values for the realistic beams. Due to too few trials or number of histories, the statistical uncertainty of the calculations is not so good that the curves are not smooth.
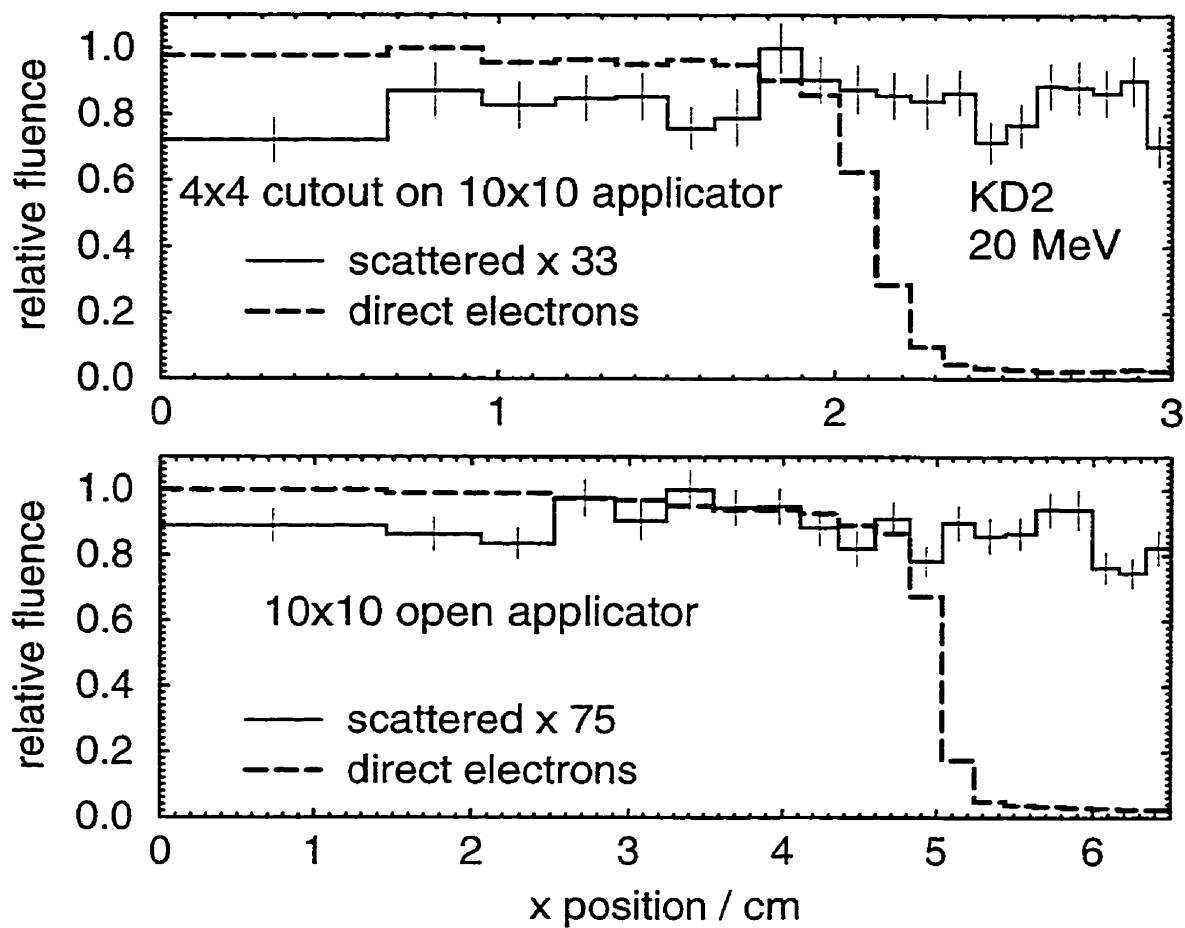
B.4   Other figures

Figure B.11: Relative fluence for KD2 20 MeV beams. The bin width varies so that the area of each bin of a square ring is the same. Relatively more scattered electrons are found in the 4×4 cm^2 field.

Bibliography

[1] http://www.cancer.ca/stats/   [cited pg. 2]

[2] W.T. Moss, W.N. Brand and H. Battifora, "Radiation oncology: rationale, technique, results", The C.V. Mosby Company, St. Louis, (1979).

[cited pg. 2]

[3] F.H. Attix, "Introduction to Radiological Physics and Radiation Dosimetry", Wiley, New York, (1986).   [cited pg. 2]

[4] F.M. Khan, "The Physics of Radiation Therapy", Williams and Wilkins, Baltimore, Maryland, 1984.   [cited pg. 4, 8]

[5] F.M. Khan, K.P. Doppke, K.R. Hogstrom, G.J. Kutcher, R. Nath, S.C. Prasad, J.C. Purdy, M. Rozenfeld and B.L. Werner, "Clinical electron-beam dosimetry: Report of AAPM Radiation Therapy Committee Task Group 25," Med. Phys. 18 73 – 109 (1991).   [cited pg. 5, 8, 45, 48, 52, 58, 58, 59, 61, 74, 75, 80]

[6] B.L. Werner, F.M. Khan and F.C. Deibel, "A model for calculating electron beam scattering in treatment planning," Med. Phys, 9 180 – 187 (1982).

[cited pg. 6]

[7] I. Lax and A. Brahme, "Electron beam dose planning using gaussian beams," Acta. Radiol. Oncology 24 75 – 85 (1985).   [cited pg. 6]

[17] F.M. Khan, W. Sewchand and S.H. Levitt, "Effect of air space on depth dose in electron beam therapy", Radiology, **126** 249 – 252 (1978).   [cited pg. 8, 58]

[18] J.A. Meyer, J.R. Palta and K.R. Hogstrom, "Demonstration of relatively new electron dosimetry measurement techniques on the Mevatron 80", Med. Phys., **11** 670 – 677 (1984).   [cited pg. 8]

[19] M.D. Mills, K.R. Hogstrom and P.R. Almond, "Prediction of electron beam output factors," Med. Phys. **9** 60 – 68 (1982).

[cited pg. 8, 8, 14, 48, 61, 85, 85, 85, 100, 102, 100]

[20] M.D. Mills, K.R. Hogstrom and R.S. Fields, "Determination of electron beam output factors for a 20-MeV linear accelerator", Med. Phys., **12** 473 – 476 (1985).   [cited pg. 8]

[21] I.A.D. Bruinvis and W.A.F. Mathol, "Calculation of electron beam depth-dose curves and output factors for arbitrarily large fields", Radiother. Oncol., **11** 395 – 404 (1988).   [cited pg. 8, 9]

[22] B.J. McParland, "A method of calculating the output factors of arbitrarily shaped electron fields", Med. Phys., **16** 88 – 93 (1989).   [cited pg. 8, 9]

[23] K.R. Hogstrom, M.D. Mills and P.R. Almond, "Electron beam dose calculations", Phys. Med. Biol. **26** 445 – 459 (1981).   [cited pg. 8]

[24] I.A.D. Bruinvis, A. van Amstel, A.J. Elevelt and R. van der Laarse, "Calculation of electron beam dose distributions for arbitrarily shaped fields", Phys. Med. Biol. **28** 667 (1983).   [cited pg. 9]

[25] F.K. Khan, F.C. Deibel, B.J. Gerbi and I.J. Das, "Dosimetry of irregularly shaped electron fields", Med. Phys. (abstract) **14** 473 (1987).   [cited pg. 9]

[36] L.L. Carter and E.D. Cashwell, "Particle transport simulation with the Monte Carlo method, ERDA Critical Review Series, TID-26607, (1975).

[cited pg. 10]

[37] J.R. Howell, "Application of Monte Carlo to heat transfer problems", Advances in Heat Transfer, **5**, T.F. Irvinem Jr., and J.P. Hartnett, Eds., Academic Press, New York, (1968). [cited pg. 10]

[38] R.L. Ford and W.R. Nelson, "The EGS code system: computer programs for the Monte Carlo simulation of electromagnetic cascade showers (Version 3)", SLAC-210, Stanford University, (1978). [cited pg. 10]

[39] W.R. Nelson, H. Hirayama and D.W.O. Rogers, "The EGS4 Code System," Stanford Linear Accelerator Center Report SLAC-265, Stanford Calif, (1985).

[cited pg. 10, 20, 20, 21]

[40] W.R. Nelson and D.W.O. Rogers, "Structure and Operation of the EGS4 code system," in "Monte Carlo Transport of Electrons and Photons Below 50 MeV", eds. T.M. Jenkins, W.R. Nelson, A. Rindi, A.E. Nahum and D.W.O. Rogers, (Plenum Press) 287 – 306 (1989). [cited pg. 10, 20]

[41] M.J. Berger, "Monte Carlo calculation of the penetration and diffusion of fast charged particles", Methods in Computational Physics, **1**, B. Alder, S. Fernbach and M. Rotenberg, Eds., Academic Press, New York, 135 – 215 (1963).

[cited pg. 10]

[42] H.M. Colbert, "SANDYL: a computer program for calculating combined photon-electron transport in complex systems", SCL-DR-72019, Sandia Laboratories, Livermore, (1973). [cited pg. 10]

[43] J.A. Halbleib, Sr. and W.H. Vandevender, "CYLTRAN", Nucl. Sci. Eng. **61** 288 – 289 (1976. [cited pg. 10, 20]

[44] D.W.O. Rogers, B.A. Faddegon, G.X. Ding, C.-M. Ma, J. Wei and T.R. Mackie, "BEAM: A Monte Carlo code to simulate radiotherapy treatment units," Medical Physics **22** (503 – 524) (1995).   [cited pg. 10, 13, 20, 22, 22, 23]

[45] H. Neuenschwander and E.J. Born, "A Macro Monte Carlo method for electron beam dose calculations", Phys. Med. Biol., **37** 107 – 125 (1992).

[cited pg. 10]

[46] H. Neuenschwander, T.R. Mackie and P.J. Reckwerdt, "MMC – a high performance Monte Carlo code for electron beam treatment planning", Phys. Med. Biol., **40** 543 – 574 (1995).   [cited pg. 10]

[47] I. Kawrakow, M. Fippel and K. Friedrich, "3D Electron Dose Calculation using a Voxel based Monte Carlo Algorithm", Med. Phys., **23** 445 – 457 (1996).

[cited pg. 10]

[48] I. Kawrakow, "Improved modeling of multiple scattering in the Voxel Monte Carlo model", Med. Phys., **24** 505 – 517 (1997).   [cited pg. 10]

[49] J. Briesmeister, "MCNP—A general purpose Monte Carlo code for neutron and photon transport, Version 3A", Los Alamos National Laboratory Report LA-7396-M (Los Alamos, NM), (1986).   [cited pg. 10]

[50] J. F. Briesmeister (Editor), "MCNP—A general Monte Carlo N-particle transport code", Los Alamos National Laboratory Report LA-12625-M (Los Alamos, NM), (1993).   [cited pg. 10]

[51] F. Salvat, J.M. Fernandez-Varea, J. Baro and J. Sempau, "PENELOPE, an algorithm and computer code for Monte Carlo simulation of electron-photon showers", University of Barcelona preprint, (1996).   [cited pg. 10]

[52] D.W.O. Rogers and A.F. Bielajew, "Monte Carlo techniques of electron and photon transport for radiation dosimetry," in "The Dosimetry of Ionizing Ra-

diation",Vol III, eds. K.R. Kase, B.E. Bjarngard, and F.H. Attix, (Academic Press) 427 − 539 (1990).   [cited pg. 12, 12, 20, 20, 40, 40]

[53] D.W.O. Rogers, A.F. Bielajew and A.E. Nahum, "Ion chamber response and A_{wall} correction factors in a ^{60}Co beam by Monte Carlo simulation", Phys. Med. Biol., **30** 429 − 443 (1985).   [cited pg. 13]

[54] K.R. Shortt, C.K. Ross, A.F. Bielajew and D.W.O. Rogers, "Electron Beam Dose Distributions Near Standard Inhomogeneities," Physics in Medicine and Biology **31** 235 − 249 (1986).   [cited pg. 13]

[55] M. Boutillon, "Gap correction for the calorimetric measurement of absorbed dose in graphite with a ^{60}Co beam", Phys. Med. Biol., **34** 1809 − 1821 (1989).
[cited pg. 13]

[56] M. Udale, "Monte Carlo calculations of electron beam parameters for three Philips linear accelerators," Phys. Med. Biol. **37** 85 − 105 (1992).
[cited pg. 13, 20]

[57] C.-M. Ma, D.W.O. Rogers, K.R. Shortt, C.K. Ross, A.E. Nahum and A.F. Bielajew, "Wall correction and absorbed dose conversion factors for Fricke dosimetry: Monte Carlo calculations and measurements", Med. Phys., **20** 283 − 292 (1993).   [cited pg. 13]

[58] D.M.J. Lovelock, C.S. Chui, J. Kutcher and R. Mohan, "Analysis of the photon beam treatment planning data for a scanning beam machine", Med. Phys, **21** 1969 − 1977 (1994).   [cited pg. 13, 20]

[59] D.S. Davis, D.S. Followill, P. Kennedy and W.F. Hanson, "Electron percent depth dose and cone ratio data from various machines", Med. Phys. (abstract), **22** 1007 (1995).   [cited pg. 14]

editor R.L. Morin, CRC Press, Inc., Boca Raton, Florida, 53 – 101 (1988).

[cited pg. 20]

[69] T.R. Mackie, "Applications of the Monte Carlo Method in Radiotherapy," in Vol. III of "Dosimetry of Ionizing Radiation" eds. K. Kase, B. Bjarngard and F.H. Attix (Academic Press, New York) 541 – 620 (1990). [cited pg. 20]

[70] P. Andreo, "Monte Carlo techniques in medical radiation physics", Phys. Med. Biol., **36** 861 – 920 (1991). [cited pg. 20]

[71] M.J. Berger and S.M. Seltzer, "Bremsstrahlung and photonneutrons from thick tungsten and tantalum targets", Phys. Rev., **C2**, 621 – 631 (1970).

[cited pg. 20]

[72] M.J. Berger and S.M. Seltzer, "ETRAN, Monte Carlo code system for electron and photon transport through extended media" Documentation for RSIC Computer Code Package CCC-107, Oak Ridge National Lab., Oak Ridge, Tennessee, 1973. [cited pg. 20]

[73] S.M. Seltzer, "An overview of ETRAN Monte Carlo methods", Monte Carlo Transport of Electrons and Photons, T.M. Jenkins, W.R. Nelson, A. Rindi, A.E. Nahum and D.W.O. Rogers, Eds., Plenum Press, New York, 153 – 182 (1989). [cited pg. 20]

[74] J.A. Halbleib and W.H. Vandevender, "TIGER" Nucl. Sci. Eng. **57** 94 – 95 (1975). [cited pg. 20]

[75] J.A. Halbleib and T.A. Mehlhorn, "ITS: The Integrated TIGER Series of Coupled Electron/Photon Monte Carlo Transport Codes", Sandia Report SAND84-0573, (1984). [cited pg. 20]

[76] J.A. Halbleib, R.P. Kensek, T.A. Mehlhorn, G.D. Valdez, S.M. Seltzer and M.J. Berger, "ITS Version 3.0: The Integrated TIGER Series of Coupled

Electron/Photon Monte Carlo Transport Codes", Sandia report SAND91-1634, (1992). [cited pg. 20]

[77] D.W.O. Rogers, A.F. Bielajew, T.R. Mackie and S.S. Kubsad, "The OMEGA Project: treatment planning for electron-beam radiotherapy using Monte Carlo techniques," Phys. Med. Biol. **35** (abs) 285 (1990). [cited pg. 22]

[78] T.R. Mackie, S.S. Kubsad, D.W.O. Rogers and A.F. Bielajew, "The OMEGA project: Electron dose planning using Monte Carlo simulation," Med. Phys. **17** (abs) 732 (1990). [cited pg. 22]

[79] G.X. Ding, "An Investigation of Radiotherapy Electron Beams Using Monte Carlo Techniques", PhD thesis, Carleton University, Ottawa, (1995).
[cited pg. 22, 23, 35]

[80] D.W.O. Rogers, C.-M. Ma, G.X. Ding and B. Walters, D. Sheikh-Bagheri and G.G. Zhang, "BEAM Users Manual", NRC Report PIRS-0509(A)revC, NRCC, Ottawa, (1998). [cited pg. 23, 23, 27, 77, 110]

[81] G.X. Ding, D.W.O. Rogers and T.R. Mackie, "Calculation of stopping-power ratios using realistic clinical electron beams," , Med. Phys. **22** 489 – 501 (1995).
[cited pg. 30, 39, 75]

[82] G.X. Ding and D.W.O. Rogers, "Energy spectra, angular spread and dose distributions of electron beams from various accelerators used in radiotherapy", NRC Report PIRS-0439, (1995). [cited pg. 35]

[83] C. Duzenli, B. McClean and C. Field, "Backscatter into the beam monitor chamber: Implications for dosimetry of asymmetric collimator," Med. Phys. **20** 363 – 367 (1993). [cited pg. 35]

[84] G.X. Ding, D.W.O. Rogers, and T.R. Mackie, "Calculation of backscatter into beam monitor chamber for electron beams," Med. Phys. **21** (abs) 923 (1994).
[cited pg. 35]

[95] A. Niroomand-Rad, M.T. Gillin, R.W. Kline and D.F. Grimm, "Film dosimetry of small electron beams for routine radiotherapy planning", Med. Phys. **13** 416 – 421 (1986). [cited pg. 72, 72]

[96] A. Niroomand-Rad, "Film dosimetry of small elongated electron beams for treatment planning", Med. Phys. **16** 655 – 662 (1989). [cited pg. 72]

[97] AAPM TG-21, "A protocol for the determination of absorbed dose from high-energy photon and electron beams," Med. Phys. **10** 741 – 771 (1983).
[cited pg. 72, 72, 72, 72, 74, 75]

[98] J.M. Havercroft and S.C. Klevenhagen, "Ion recombination corrections for plane-parallel and thimble chambers in electron and photon radiation", Phys. Med. Biol. **38** 25 – 38 (1993). [cited pg. 72]

[99] IAEA, International Atomic Energy Agency, "Absorbed Dose Determination in Photon and Electron Beams; An International Code of Practice," Technical Report Series No. 277, IAEA, Vienna (1987). [cited pg. 72]

[100] P.R. Almond, F.H. Attix, S. Goetsch, L.J. Humphries, H. Kubo, R. Nath and D.W.O. Rogers, "The calibration and use of plane-parallel ionization chambers for dosimetry of electron beams: An extension of the 1983 AAPM protocol, Report of AAPM Radiation Therapy Committee Task Group 39," Med. Phys. **21** 1251 – 1260 (1994). [cited pg. 72]

[101] A. Van der Plaetsen, J. Seuntjens, H. Thierens and S. Vynckier "Verification of absorbed doses determined with thimble and parallel-plate ionization chambers in clinical electron beams using ferrous sulphate dosimetry", Med. Phys. **21** 37 – 44 (1994). [cited pg. 72]

[102] J. Cygler, X.A. Li, G.X. Ding and E. Lawrence, "Practical Approach to Electron Beam Dosimetry at Extended SSD", Phys. Med. Biol. **42** 1505 – 1514 (1997).
[cited pg. 73, 80]

[103] K.A. Johansson, L.O. Mattsson, L. Lindborg and H. Svensson, "Absorbed-dose determination with ionization chambers in electron and photon beams having energies between 1 and 50 MeV," IAEA Symposium Proceedings, (Vienna) IAEA-SM-222/35 243 – 270 (1977). [cited pg. 75]

[104] D.W.O. Rogers and A.F. Bielajew, "Differences in Electron Depth Dose Curves Calculated with EGS and ETRAN and Improved Energy Range Relationships," Med. Phys. **13** 687 – 694 (1986). [cited pg. 80]

[105] D.T. Burns, G.X. Ding and D.W.O. Rogers, "R_{50} as a beam quality specifier for selecting stopping-power ratios and reference depths for electron dosimetry", Med. Phys. **23** 383 – 388 (1996). [cited pg. 82]

[106] R. Brun, O. Couet, C. Vandoni and P. Zanarini, "PAW User Guide," CERN Computer Center, Geneva, Switzerland (1992). [cited pg. 91]

IMAGE EVALUATION
TEST TARGET (QA-3)

150mm

6"
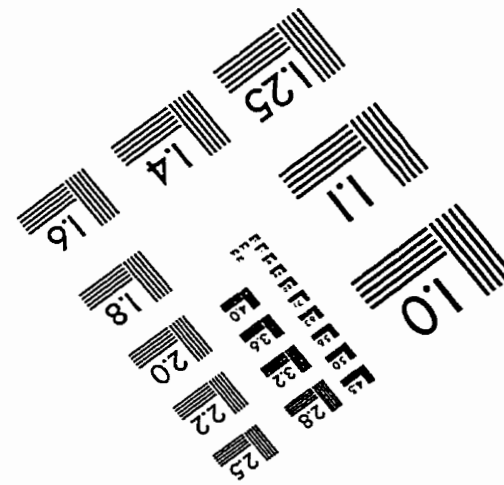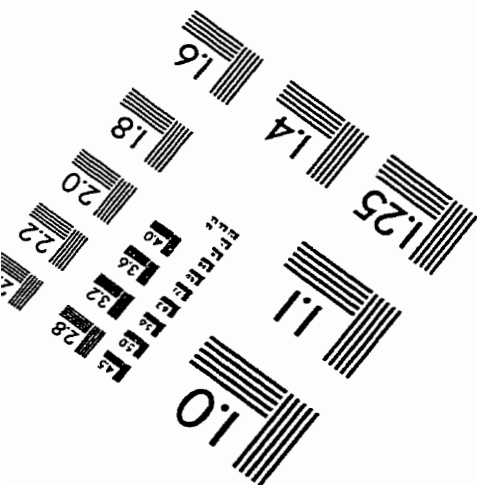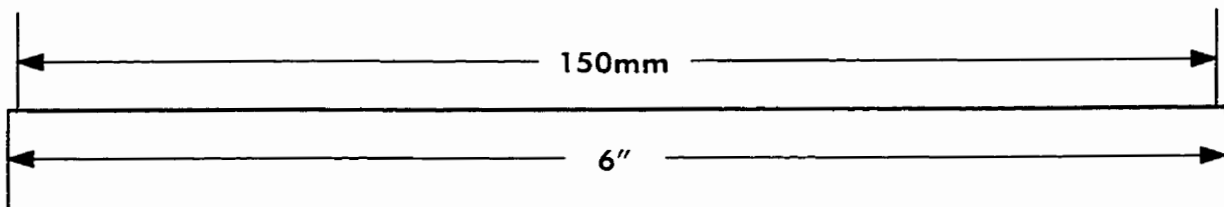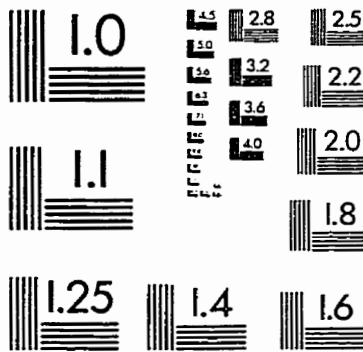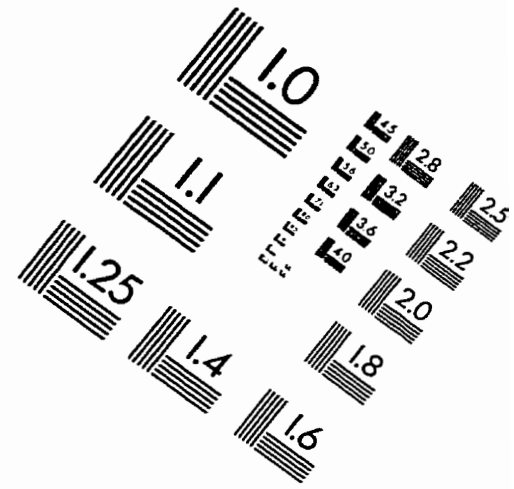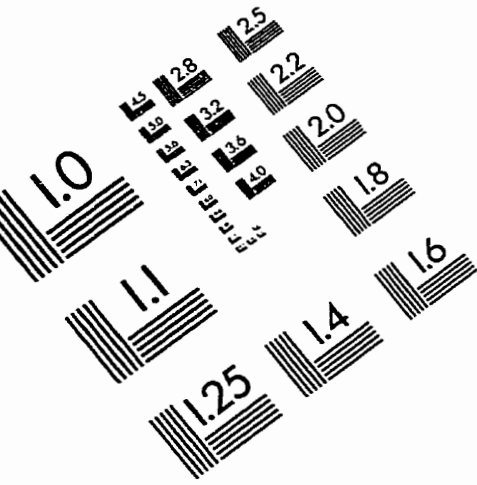
APPLIED IMAGE, Inc
1653 East Main Street
Rochester, NY 14609 USA
Phone: 716/482-0300
Fax: 716/288-5989